Design method for s-CO_2 gas turbine power plants

Integration of thermodynamic analysis and components design for advanced applications

J.S. Bahamonde Noriega

Master of Science Thesis

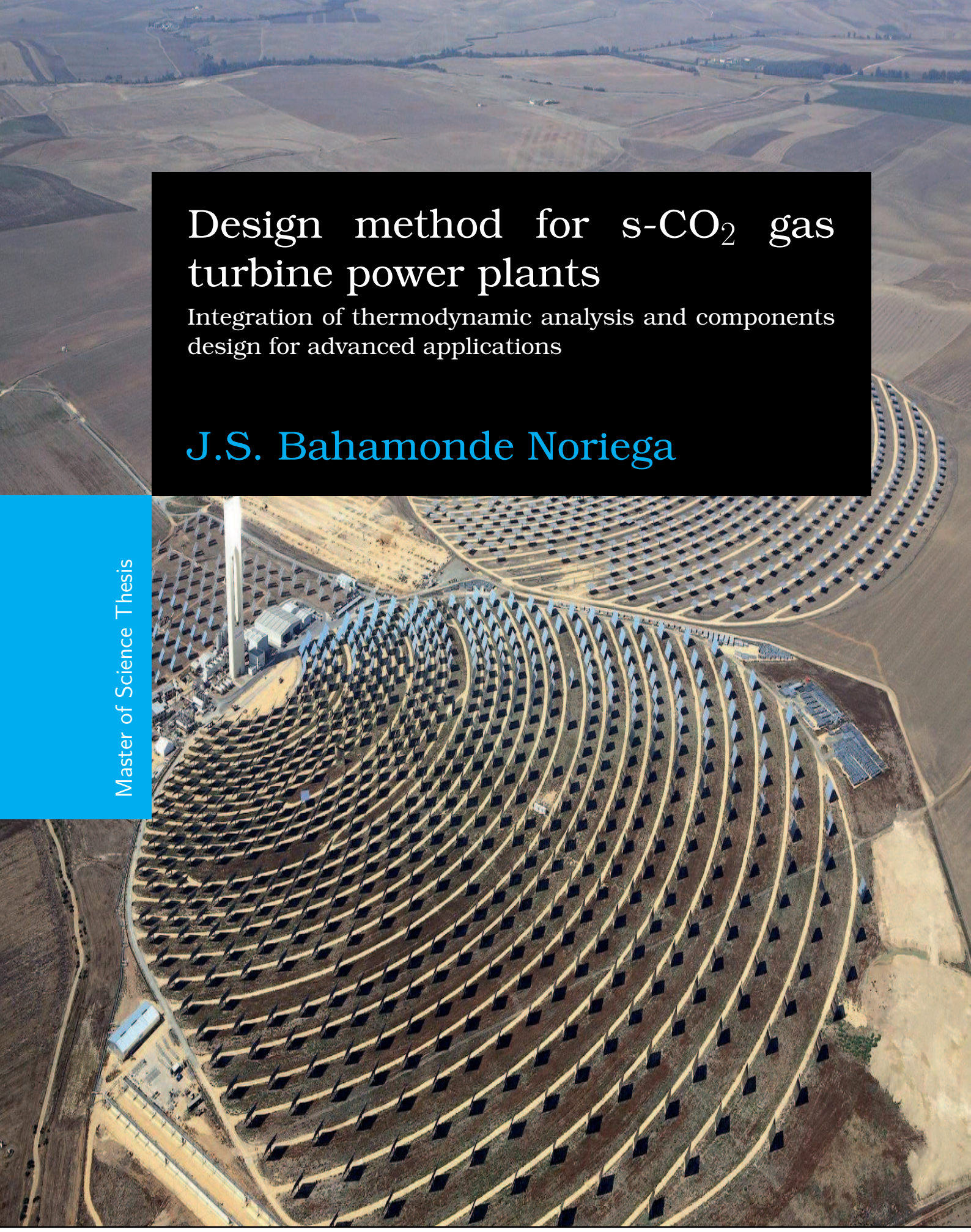

TU Delft Delft University of Technology

Report: P&E-2530

Process & Energy Delft

Design method for s-CO_2 gas turbine power plants

Integration of thermodynamic analysis and components design for advanced applications

Master of Science Thesis

For the degree of Master of Science in Mechanical Engineering at Delft University of Technology

J.S. Bahamonde Noriega

October 21, 2012

Faculty of Mechanical, Maritime and Materials Engineering (3mE) · Delft University of Technology

Report: P&E-2530

Delft University of Technology

Department of

Process and Energy (P&E)

The undersigned hereby certify that they have read and recommend to the Faculty of Mechanical Engineering (3mE) for acceptance a thesis entitled

Design method for s-CO_2 gas turbine power plants

Integration of thermodynamic analysis and components design for advanced applications

by

Juan Sebastian Bahamonde Noriega

in partial fulfillment of the requirements for the degree of

Master of Science Mechanical Engineering

Dated: October 21, 2012

Supervisors:

Prof.dr. P. Colonna	E. Rinaldi, MSc

Exam committee:

Prof.ir. J.P. van Buijtenen	Prof.dr.ir. B.J. Boersma
Prof.dr. P. Colonna	Dr. R. Pecnik
Dr. A.G. Rao	E. Rinaldi, MSc.

Abstract

Supercritical CO_2 (s-CO_2) Brayton power plants will be part of the next-generation energy conversion systems since they are based on technically challenging thermodynamic cycles with processes that occur entirely above the critical point of the working fluid. Advantages of these new power systems are the possibility of using external thermal energy sources, like concentrated solar radiation or biomass combustion, high conversion efficiency at moderate temperatures, and possibly low operational and investment costs. Supercritical CO_2 as the working fluid presents additional advantages: it is thermochemically stable up to very high temperatures, comparatively inert regarding the containing materials, and it is non-toxic and relatively inexpensive. Although research on s-CO_2 power applications has grown considerably in the last years, and the expansion of simulation capabilities is revolutionizing engineering design, the thermodynamic cycle analysis/optimization, and the design of the system components are activities still performed independently and in an iterative manner. This conventional design procedure is time-consuming and it might neglect portions of the potentially vast design envelope. This work stemmed from the observation that, with today's simulation capabilities, in case of a relatively simple system like a s-CO_2 power plant, the optimization of the thermodynamic cycle and the design of the system components can be integrated into a single calculation procedure, which can be subjected to an automated constrained optimization process. The objective of this work is therefore to perform a preliminary assessment of the envisaged methodology.

First, the thermodynamic analysis of the system has been performed thanks to a computer code developed for this purpose, and it consists in the study of three s-CO_2 power cycle configurations. The thermal efficiency is prescribed to a value that is greater than that of a cutting-edge gas turbine, while the power capacity is set to the same value. These are 50% and 18.7 MW respectively, and the effect of the components operation on the turbine inlet temperature (TIT) and regeneration load is studied. The recompression Brayton cycle configuration allows to comply with the specified performance with the lowest turbine inlet temperature (787°C) and at moderate maximum pressure (272 bar). However, it requires larger mass flow rates leading to larger equipment. The operating conditions given by this analysis are used as inputs for the design of the components, which is focused on the re-

generator and the cooler since they are the largest and possibly most expensive components of the s-CO_2 power plant. The steady state models are based on the discretization of the flow passages and the evaluation of the fluid properties in each element. The models are validated against the design and performance data of an existing s-CO_2 heat exchanger, and a well-know commercial design code.

The methodology that combines the thermodynamic analysis and the components design is implemented into a computational routine that is tested with two study cases. The first one is aimed as a first assessment of a futuristic concept, namely the adoption of a s-CO_2 closed Brayton gas turbine for aircraft propulsion. The s-CO_2 power system is designed such that it exceeds the performance rating of a cutting-edge turbofan, and at the same time the weight of the system is decreased as much as possible. The calculations show that the regenerators, designed with current technology for stationary applications, have a weight of minimum 5 tonne, which is almost the weight of the reference engine. The second study case regards the design of a power plant using a solar tower power as the heater, with the same power output and efficiency as the ones adopted for the thermodynamic analysis (18.7 MW, 50%). The methodology is extended to the dimensioning of the heliostat field, since its share of the total investment cost is possibly the largest. This exercise provides key characteristics of the power plant: 636 heliostats that occupy an area of 300 m^2, regenerators weight of 17 tonne, dry cooler weight of 18 tonne, TIT of 647°C, and compressor discharge pressure of 245 bar. Finally, the formulation of an optimization problem for the net present value of the solar power plant is outlined. Although the calculations are not performed due to the large computational time required, the potential of the methodology is exemplified, pointing to further work in this promising direction.

Table of Contents

List of Figures

List of Tables

Acknowledgments

I want to thank my supervisor Prof. Dr. Piero Colonna for his guidance, enthusiasm and time devoted to this project. His vision about renewable energies and the dedication he gives to this research field are sources of inspiration for me.

My sincere thanks also go to Enrico Rinaldi, who has been always available to help me during these 8 months.

I want to express my gratitude to the rest of the examination committee. I appreciate their time devoted to reading and evaluating this document.

Finally, I want to thank my family, their love, support and patience made this work possible.

Delft, University of Technology
October 21, 2012

J.S. Bahamonde Noriega

Chapter 1

Introduction

Fossil fuels have been used by humans for thousands of years. In China, in about 500 B.C., people burned natural gas transporting it with bamboo straws. American Indians used petroleum as paint and medicines. Coal has been burned as a source of thermal energy for hundreds of years to melt metals and make weapons and tools [12]. However, the commercialization of petroleum began in 1872, which created the fossil fuel industry and brought large economic and technological growth with the industrialization of electric energy generation in the second industrial revolution [13]. Nowadays, electricity has become part of the daily life and it is one of the primary needs of society required to maintain and improve its well being.

Although fossil fuels have been suitable companions to human development, their disadvantages have become more evident with their increasing consumption. Global warming, air pollution, acid precipitation, ozone depletion and forest destruction, which are side effects produced by the energy generation from fossil fuels, are driving forces that promote the research of alternative and cleaner energy conversion technologies [14]. Furthermore, fossil fuels are nonrenewable, which means that they are going to be completely exhausted in the future. For this reason, time and effort should be invested to search for alternative solutions to satisfy the energy demand. Next-generation thermodynamic cycles for energy conversion systems are powerful alternatives which could reduce the environmental impacts and whose feasibility is a matter of continuous research.

1-1 The supercritical Brayton cycle

Next-generation thermal energy conversion systems use thermodynamic cycles with processes that occur either entirely above the critical point (supercritical), or that allow the thermodynamic states to be also below the critical point (transcritical). Examples of these cycles are the supercritical organic Rankine cycle, the transcritical condensation cycle and the supercritical Brayton cycle [15]. As described in more detail in this section, the systems based

on these concepts present several attractive characteristics. For example, the possibility of using external heat sources like solar radiation, biomass or nuclear fuel, the capability of using low to medium-temperature waste heat from other production processes, and potential low operational and investment costs [15].

One of the most promising options is the supercritical CO_2 (s-CO_2) Brayton cycle. The studies about its application for power generation systems have their oldest reference in 1948, when Sulzer Ltd. patented a partial condensation s-CO_2 Brayton energy generator [16]. In the United States, Feher [1] proposed the first s-CO_2 design in 1968 (the Feher cycle), in which all the processes take place above the critical pressure and the compression occurs completely in the liquid phase. In the same year Angelino [17] performed an extensive analysis of transcritical CO_2 power systems. These cycles include CO_2 condensation with temperatures and pressures below the critical point. Angelino considers several system configurations with additional compressors and heat exchangers to reduce the internal irreversibilities of the thermodynamic cycles. The s-CO_2 cycles immediately raised interest and the investigation of these systems started in many countries [16] (Feher in the United states, Angelino in Italy and Sulzer Ltd. in Switzerland are examples).

The Feher cycle T-s diagram is shown in Figure 1-1. The processes taking place are:

- pumping (a-b),
- cold side regeneration (b-c),
- heat addition (c-d),
- expansion (d-e),
- hot side regeneration (e-f) and
- heat rejection (f-a).

Notice that the processes in this power cycle operate always above the critical pressure. However, the pumping works entirely below the critical temperature with the working fluid in the liquid phase. Similarly, the regeneration process operates with condensation in its hot side and evaporation in its cold side. While these kind of cycles can work with many suitable fluids, the first choice of Feher is CO_2 due to some advantages over other fluids:

- its critical pressure is one third of that of water, which allows for a lower operation pressure,
- it is stable and inert at the temperatures of interest, and
- it is abundant, non-toxic and relatively inexepensive.

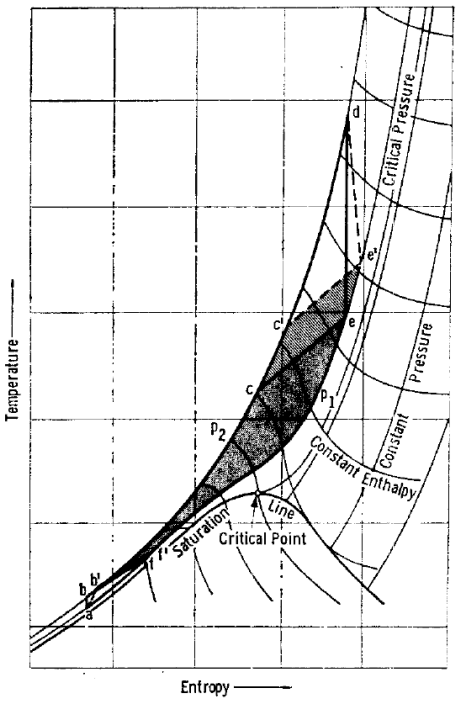

Figure 1-1: Feher cycle T-s diagram [1] (not in scale).

Additionally, he shows that these kind of systems are promising alternatives for power generation since they avoid several disadvantages of the conventional Rankine and Brayton power

systems, nevertheless combining many of their benefits:

- high thermal efficiency at moderate temperatures due to the small compression work and large renegeration power,
- high power densities that are consequence of the high density of the working fluid under supercritical pressures, leading to smaller equipment,
- low pressure ratio which reduces the number of stages in the turbine,
- compression, expansion, and heat rejection of the working fluid under single phase, which reduces the complexity of the system, and
- insensitivity to compression efficiency due to its small specific work compared to the one of the turbine.

The supercritical Brayton cycle with CO_2 as the working fluid maintains the advantages of the Feher cycle and adds two additional benefits. First, all the operating conditions remain above the critical temperature, which leads to single state operation that avoids the complexity of fluid condensation and evaporation in the regeneration processes. Second, the critical temperature of CO_2 (30.98°C) allows the use of air at lower temperatures instead of water as the sink for the heat rejection process, reducing the environmental impact. A diagram for the simple regenerative Brayton system is shown in Figure 1-2. The cycle is composed by the same processes as the Feher cycle with the compression taking place above the critical temperature.

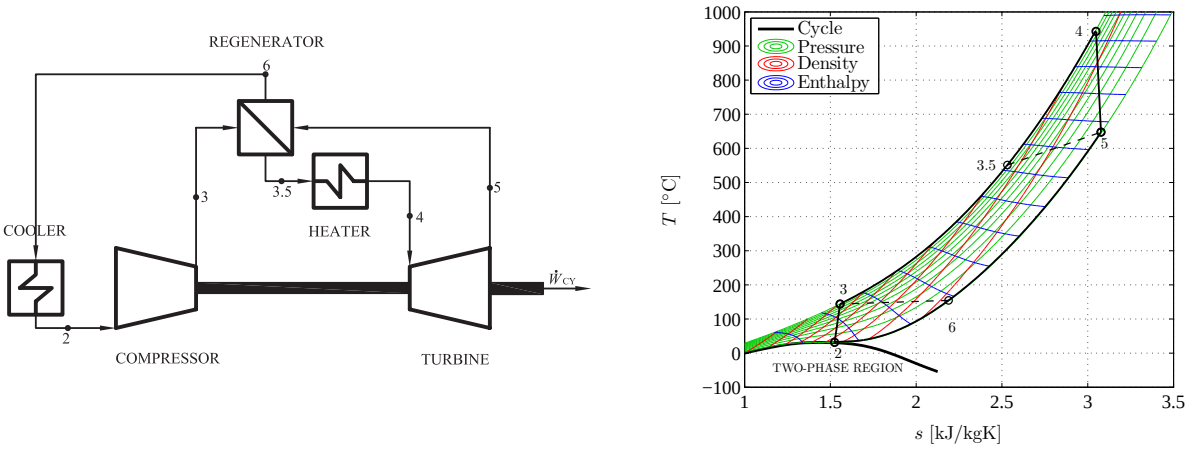

Figure 1-2: Supercritical regenerative Brayton power system. Process flow diagram and T-s diagram (for operating conditions of the T-s diagram refer to Figure 2-11).

Even though the interest in the CO_2 power cycles arose in the research community decades ago, these systems were not developed to commercial scale mainly due to insufficient turbomachinery experience, lack of suitable heat exchangers and lack of appropriate heat sources [16]. It is in the last years that both supercritical and transcritical CO_2 power generation systems have become again a matter of raising interest and research. This new age of s-CO_2 investigation starts with the works of Petr et al. [18, 19] in the Czech Republic and reached its definitive breakthrough in the United States with the studies of Dostal et al. [16, 20, 21], which are oriented towards nuclear applications. Nowadays the investigation of these sys-

tems is still growing and several institutions are currently studying the application of s-CO_2 power generation systems with thermal energy sources such as nuclear reactors [16, 22–28] or concentrating solar power (CSP) [29–32].

The s-CO_2 Brayton system is a technology still emerging, with few experimental setups for the study of the operation of the entire system. The most relevant institution involved in this field of investigation is currently the Sandia National Laboratories (SNL), which owns two s-CO_2 test loops used for research purposes [26]. The first test bench consists in a Brayton loop with a heater power of 260 kW which is able to generate electricity with multiple cycle configurations. The second test bench is a motor driven s-CO_2 compression loop, which is used to explore the characteristics of CO_2 gas mixtures, condensation cycles and gas-foil thrust bearing performance. These studies lead to the experimental confirmation of the mentioned advantages of the s-CO_2 systems, which have been reported as the key features of the supercritical Brayton systems [33]:

- s-CO_2 power plants can be powered with all medium to high temperature energy sources,
- efficiency between 43% (turbine inlet tempeterature (TIT) of 538°C) and 50% (TIT of 700°C) for 10 to 300 MW systems,
- standard materials can be used for the components (stainless steels and Inconels),
- high power density for the conversion system (a s-CO_2 gas turbine power plant is approximately 30 times smaller than steam and 6 times smaller than helium or air power plants), and
- modular capacity, with dimensions that make these systems factory-manufacturable (units with 10 MW of capacity and dimensions of approximately 2.5 m x 8 m).

Nowadays, the studies on s-CO_2 power conversion systems branched in many directions that include a broad variety of engineering and commercial fields. The research areas covered can be classified in four groups [26, 33]. The first branch deals the hardware development. SNL is the only institution that continuously reports experimental results with s-CO_2 Brayton test loops, although there are other organizations that are currently working with similar resources or that are planning to do so (Bechtel Marine Propulsion Corporation [34], Knolls Atomic Power Laboratory [35], Southwest research Institute []). The second is focused on improving the performance and extending the capabilities of s-CO_2 power systems to applications with gas mixtures, condensation cycles and s-CO_2 heat pumps. This field is covered both experimentally by SNL and theoretically by other researchers [15, 23, 29, 36]. The third area is focused on the modeling of the components in the Brayton power systems and on the development of control strategies. This is a research field covered by many institutions which study turbomachinery modeling [24, 37, 38] or the heat exchangers modeling [39–42]. Finally, the fourth field deals with the implementation and commercialization of the s-CO_2 power systems. SNL is one of the leading institutions of this research branch, since it aims to built the first commercial set-up of approximately 10 MW, which can be constituted by currently available industrial components [33]. Other institutions in this research field are the Southwest Research Institute and Brayton Energy LLC. Both of them have been awarded development grants by the U.S Department of Energy under the SunShot CSP R&D initiative, which aims to reduce the cost of CSP technologies. The southwest research institute will develop an s-CO_2 power cycle for low cost modular CSP applications, and Brayton Energy LLC will build and test a new solar receiver with s-CO_2 as the heat transfer fluid [43].

1-2 Motivation and scope

Although the efforts towards the development of s-CO_2 power systems are increasing, the analysis of the thermodynamic cycles and the components design are regularly performed independently. Consequently, there are no available tools that integrate these two aspects. Such innovation would be useful to obtain a first estimation of the size, cost and performance of the equipment given the desired power output and operating conditions. Additionally, this tool could be used to implement a parametric analysis in order to perform both thermodynamic and economic optimization processes, which are important when a compromise must be found between components size, investment cost, economic rate of return and system efficiency. The aim of the work documented in this report is to develop and test a methodology for this purpose. As it will be shown later, the components that share the largest power and probably the largest cost in the s-CO_2 systems are the heat exchangers and therefore the scope of this work is the integration of the design procedure for these components with the cycle thermodynamic analysis. The design of turbomachinery equipment is left for further developments.

1-3 Thesis Outline

Chapter 2 presents the thermodynamic analysis of three s-CO_2 power systems configurations: a Brayton regenerative, a Brayton recompression and a Rankine cycle system. The power output and the system efficiency are fixed as targets for the analysis. The different thermodynamic cycles are parametrized, and the effects of the components characteristics on the TIT and the regeneration load are evaluated. The chapter shows finally an overall comparison between the three configurations and leaves two degrees of freedom in the operation characteristics of the systems that are used for the design methods developed in the subsequent chapters.

Chapter 3 presents the development of the steady state design methods for the regenerators and the cooler. Compact heat exchangers and air cooled heat exchangers are chosen for the regenerators and the cooler respectively. The design procedure is based on the discretization of the working fluid passages and the evaluation of each element as an independent control volume. The CO_2 properties are obtained by means of a computational fluid property library, which allows to obtain accurate values in the critical region. The pressure drop and heat transfer coefficient in both heat exchangers are calculated with several correlations, which are validated against real heat exchangers data and a well-known commercial design software. The correlations that give the best results are chosen and used to calculate the weight of the heat exchangers as a function of the operating conditions obtained from the thermodynamic analysis.

Chapter 4 presents the application of the methodology described in Chapters 2 and 3 to two study cases. The first one regards the study of the feasibility of s-CO_2 Brayton power systems for aerospace propulsion. A state-of-the-art aircraft engine is selected and its thermodynamical operation is studied in order to obtain its performance rating, which is used as the target for the s-CO_2 system. The regenerators weight is calculated as a function of varying operating conditions in order to decrease their weight as much as possible and

evaluate the feasibility for this application. The second case deals with the application of s-CO_2 power generation combined with solar power towers. The solar field, which shares the largest costs in solar power tower systems, is dimensioned based on several design criteria which allow to obtain the power contribution and location of each heliostat in the field.

Finally, the conclusions and recommendations are drawn in Chapter 5.

Chapter 2

Thermodynamic cycle analysis

The present chapter presents the thermodynamic analysis of three configurations of s-CO_2 power systems, a Brayton regenerative, a Brayton vapor recompression and a Rankine regenerative system. The thermal efficiency and the power output are fixed as representative targets. The remaining parameters, e.g. turbomachinery efficiency and system pressure loss, are varied in order to study their influence on the performance of the system.

The data for the thermodynamic analysis are obtained from the first study case documented in Chapter 4, which deals with the application of s-CO_2 power generators for aircraft propulsion systems. It is shown that the power output and the efficiency of a selected high-end technology aircraft engine are 18.7 MW and 47% respectively. In order to overcome the performance rate of this engine, the targets of s-CO_2 system are set to the same power output whith a thermal efficiency of 50%.

2-1 Computational steady state analysis of s-CO_2 Brayton cycles

The thermodynamic analysis in this chapter is performed with a computational program that evaluates the effect of the components operation in the system [44]. The inputs and outputs for the program developed for the regenerative system are presented in Table 2-1. The thermodynamic analysis is traditionally focused on the maximization of the efficiency as a function of the TIT. However, in this case the efficiency is an input for the analysis, while the TIT is an output. Then, the operating conditions are not based on the maximum thermal efficiency but on the minimum TIT, as shown in Sections 2-2-5 and 2-3-4 for the regenerative and recompression Brayton systems respectively.

The internal calculations in this program are based on the solution of the steady-state mass and energy balance for each of the components in the system. The fluid thermodynamic properties in the entire project are obtained by means of a computational fluid library [45], which is set to calculate the CO_2 properties by means of a Span-Wagner multiparameter equation of state, allowing for accurate property calculations in the critical region [46].

Table 2-1: Inputs and outputs of the program used in the thermodynamic analysis of the regenerative Brayton system

Inputs		**Outputs**	
Power output	$\dot{W}_{CY}$	Turbine inlet temperature	T_4
Thermal efficiency	η_{TH}	Regenerator power and effectiveness	$\dot{Q}_{RG}$, ε_{RG}
Compressor suction pressure	P_2	Compressor power	$\dot{W}_{CM}$
Compressor discharge pressure	P_3	Turbine gross power	$\dot{W}_{TR}$
Compressor suction temperature	T_2	Heater power	$\dot{Q}_{HR}$
Cold side temperature difference	ΔT_C	CO_2 mass flow	f
Compressor adiabatic efficiency	η_{CM}	Exergy efficiency	η_{EX}
Turbine adiabatic efficiency	η_{TR}	Exergy losses per component	E_{LS}
Heater efficiency	η_{HR}	Pinch temperature	ΔT_{PN}
System pressure loss	ΔP_{LS}	Cycle pressures and temperatures	P, T

Although they are not documented in this report, the thermodynamic analysis of each power cycle in this chapter and the design procedures described in Chapters 3 and 4 have been implemented in a computational program (see Appendix A).

2-2 Regenerative Brayton system

This section presents the analysis of analyzes the regenerative Brayton system schematized in Figure 2-1.

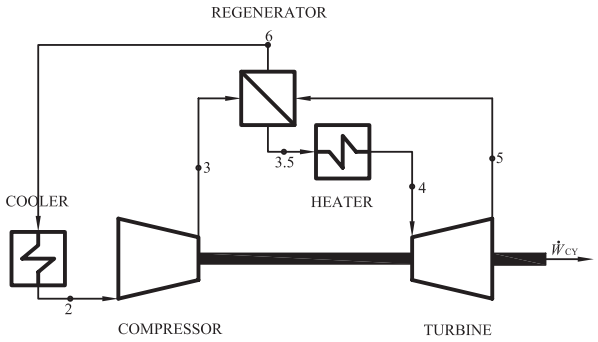

Figure 2-1: Process flow diagram of the regenerative Brayton system.

In order to study the steady state operation of this system, several parameters regarding the performance of the individual components, e.g. regenerators pinch temperature and turbomachinery efficiency, are set to initial values, which are later varied to study their effect on the performance of the system, as shown in Sections 2-2-2 to 2-2-4. The initial choice of these parameters is based on a selection from several theoretical and experimental works on s-CO_2 Brayton power systems. Table 2-2 summarizes this information and the choices made for the present study.

The compressor suction pressure and temperature are set as close as possible to the CO_2 critical point ($T_{CRIT} = 30.98°C$ $P_{CRIT} = 73.77$ bar), since this choice increases the efficiency of the system [27]. Both the compression and expansion processes are considered adiabatic. The turbine efficiency is fixed as 93.4%, the largest value among the other studies due to

Table 2-2: Parameters for the thermodynamic analysis of the s-CO_2 power generation systems.

Parameter			**Wright** [24, 25]	**Moisseyt-sev** [23]	**Dostal** [16]	**Cha** [27]	**This study**
Compressor 1 suction P.	bar	P_2	76.90	76.21	76.30	74.00	74.00
Compressor 1 suction T.	°C	T_2	31.85	32.79	32.00	31.25	31.25
Turbine adiabatic eff.	%	η_{TR}	93.00	93.40	92.90	93.40	93.40
Compressor 1 adiabatic eff.	%	η_{CM1}	75.02	88.90	95.50	89.10	85.00
Compressor 2 adiabatic eff.*	%	η_{CM2}	—	87.80	94.80	87.50	85.00
Regenerator 1 effectiveness	—	$\varepsilon_{\mathrm{RG1}}$	—	91.70	98.00	91.70	< 98.00
Regenerator 2 effectiveness*	—	$\varepsilon_{\mathrm{RG2}}$	—	94.50	98.00	94.60	< 98.00
System pressure loss	%	ΔP_{LS}	—	—	—	—	2.00
Heater efficiency	%	η_{HR}	—	—	—	—	90.00

*The components with label "2" correspond to the high temperature regenerator and compressor used in later configurations of the s-CO_2 systems.

the fact that the expansion in the turbine is done in a region in which the fluid behaves almost as an ideal gas, the expansion ratio is small, and the volumetric flow sufficient for the realization of simple axial turbine. Thus, high turbine efficiencies are expected. The compressors efficiency are set to a smaller value due to the real gas effects that influence the compression process close to the critical point.

Regarding the performance of the combustion process, the current state of the art of combustion chamber technologies allows to reach an efficiency value of 0.999 [9]. However, the carbon dioxide cannot be combusted and therefore the value of the efficiency of the heating system is taken as 0.9 in order to be conservative until the heater is designed and its efficiency estimated.

The pressure loss in the system depends on the design of the components. In this stage its value is set to 2%. The calculation of this value depends on the losses in each side of the heat transfer process (the cold side correspondent to the cold side of the regenerator and the heater, the hot side correspondent to the hot side of the regenerator and the cooler). In this steady state analysis these losses are concentrated in the turbine and compressor inlet. Thus, the pressure at point 4 (refer to Figure 2-1) depends on the pressure at point 3 and the percentage loss in the cold side of the cycle (the same procedure is applied to the hot side),

$$P_4 = P_3 \frac{100 - \Delta P_{\mathrm{LS}}\%}{100}. \tag{2-1}$$

In Section 3-1 it is shown that a Printed Circuit Heat Exchanger (PCHE) is an appropriate equipment for the realization of the regenerator. Its effectiveness in Table 2-2 corresponds to a maximum reference value given by the PCHE manufacturer [3]. Once the pinch is fixed, it is possible to calculate the regenerator effectiveness, which should not exceed this maximum value. The thermodynamics of the working fluid near to the critical point can lead to curved temperature profiles along the heat exchanger, with the pinch point not necessarily located in its hot or cold extremes. It is convenient then to fix the pinch instead of the effectiveness in order to avoid temperature crossing in the calculations of the temperature profiles. Considering this, the pinch temperature is set to 10°C. Additionally, it is necessary to define the regenerator effectiveness. A schematic diagram of the temperature profile is presented in Figure 2-2. The effectiveness is function of the enthalpies in the regenerator and

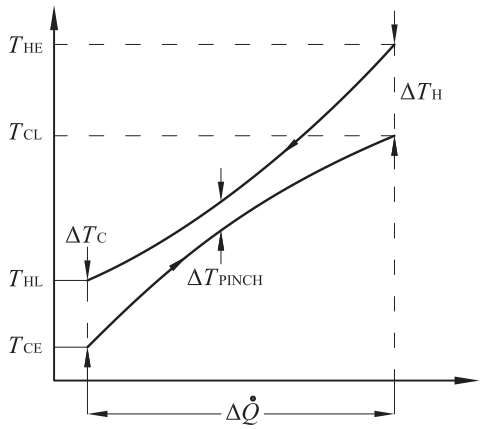

Figure 2-2: Regenerator schematic temperature profile. The curved shape is caused by the real gas effects in the CO_2 streams and the pinch is not necessarily located in the hot or cold extremes of the heat exchanger.

the mass flow of each stream,

$$\varepsilon_{RG} = \begin{cases} f_H \frac{h_{HE} - h_{HL}}{h_{HE} - h_{HL,IDEAL}} & \text{if} \quad \Delta T_H > \Delta T_C, \\ f_C \frac{h_{CL} - h_{CE}}{h_{CL,IDEAL} - h_{CE}} & \text{if} \quad \Delta T_C > \Delta T_H, \end{cases} \tag{2-2}$$

where f_H and f_C stand for the hot and cold mass flows respectively, h_{HE} and h_{HL} correspond to the entering and leaving enthalpies of the hot side respectively, and h_{CE} and h_{CL} correspond to the entering and leaving enthalpies of the cold side respectively. The ideal enthalpies $h_{HL,IDEAL}$ and $h_{CL,IDEAL}$ are the values obtained with a perfect heat exchanger, i.e., a heat exchanger with zero temperature difference between the streams at the cold or hot extremes of the heat exchange process,

$$h_{HL,IDEAL} = h(P_{HE}, T_{CE}), \tag{2-3}$$

$$h_{CL,IDEAL} = h(P_{CL}, T_{HE}), \tag{2-4}$$

These enthalpies are calculated as a function of the correspondent pressure and temperature by means of the computational fluid library, which is used in the calculation of all the fluid properties in this work.

The system performance is analyzed as a function of the compressor discharge pressure (maximum cycle pressure) with a constant pressure loss. The results are shown in Figure 2-3. Recall that the thermal efficiency of the cycle is fixed to 50% and the power to 18.7 MW. Figure 2-3a shows the TIT, which decreases with larger discharge pressures. There is a minimum at approximately 550 bar, which is a feature already discovered by Dostal [16], and leads to the conclusion that increasing the pressure ratio to reduce the TIT has a limited scope. This minimum is present due to the regeneration load that decreases with higher pressure ratios until the energy savings in the heat exchanger are not enough to maintain the thermal efficiency with lower TIT. Consequently, the TIT must increase to maintain the desired performance.

The CO_2 mass flow rate, regenerator power and effectiveness are shown in Figures 2-3b, 2-3c and 2-3d, respectively. They all decrease with larger maximum cycle pressures. The

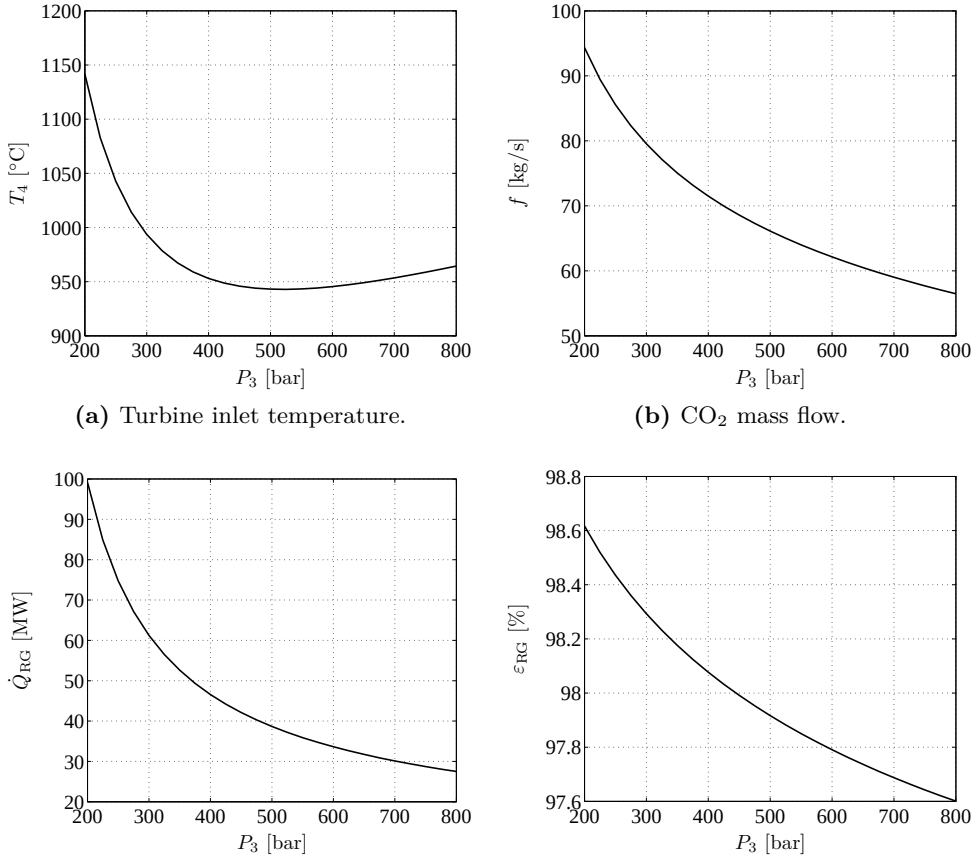

(a) Turbine inlet temperature. **(b)** CO_2 mass flow.

(c) Regenerator power. **(d)** Regenerator effectiveness.

Figure 2-3: Turbine inlet temperature, CO_2 mass flow rate, regenerator power and effectiveness for the regenerative Brayton system as a function of the compressor discharge pressure ($\eta_{TR} = 50\%$, $T_2 = 31.25°C$, $P_2 = 74$ bar, $\eta_{TR} = 93.4\%$, $\eta_{CM} = 85\%$, $\eta_{HR} = 90\%$, $\Delta P_{LS} = 2\%$, $\Delta T_{PN} = 10°C$).

mass flow rate decreases since the specific work is larger with increasing pressure ratios and therefore a lower mass flow is required to produce the fixed power of 18.7 MW. Similarly, larger pressure ratios reduce the temperature difference between the regeneration cold and hot sides, reducing the regenerator power and, since the pinch is fixed, reducing the effectiveness as well.

2-2-1 Compressor suction temperature and discharge pressure effect

This section presents the analysis of analyzes the effects of the compressor suction temperature combined with the discharge pressure on the system performance. A chart showing the variation of the turbine inlet temperature and regenerator load as a function of these two variables is presented in Figure 2-4.

Figure 2-4a shows the TIT, which has a steep variation in its slope at suction temperatures close to the critical one due to the sudden change of the specific enthalpy in the critical region. Notice that reducing the compressor suction temperature to values lower than the critical point one not reduce the TIT, which remains almost constant. This is a consequence

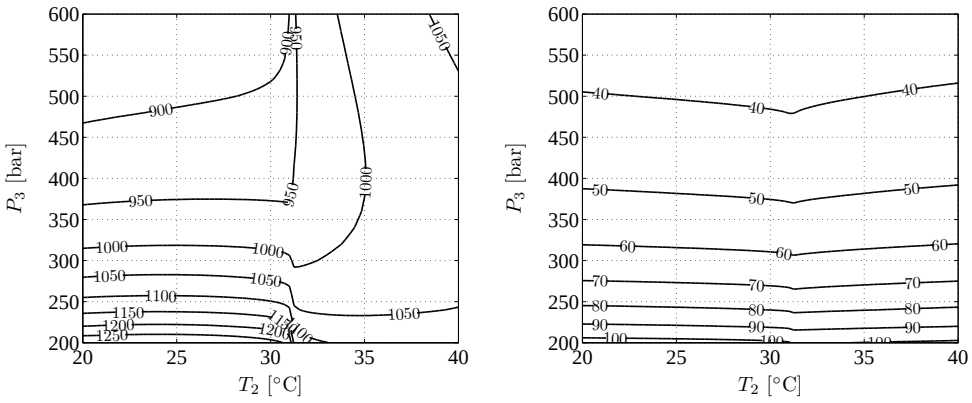

(a) Contour lines of T_4 (°C). **(b)** Contour lines of $\dot{Q}_{\mathrm{RG}}$ (MW).

Figure 2-4: Turbine inlet temperature and regenerator load for the regenerative Brayton system as a function of the compressor suction temperature and compressor discharge pressure ($\eta_{\mathrm{TR}} = 50\%$, $P_2 = 74$ bar, $\eta_{\mathrm{TR}} = 93.4\%$, $\eta_{\mathrm{CM}} = 85\%$, $\eta_{\mathrm{HR}} = 90\%$, $\Delta P_{\mathrm{LS}} = 2\%$, $\Delta T_{\mathrm{PN}} = 10°\mathrm{C}$).

of the specific work of the compressor, which does not change significantly. Figure 2-5 is useful to understand the reasons behind this. This chart presents an example of the T-s diagram of the compression in the critical region. Notice that the isenthalpic lines are not horizontal but very steep and therefore decreasing the suction temperature with constant pressure ratio will decrease the temperature rise in the compressor, but not the specific work. On the other hand, the pressure ratio has an effect and increasing the discharge presure reduces the TIT since large pressure ratios increase the specific work of the cycle [47].

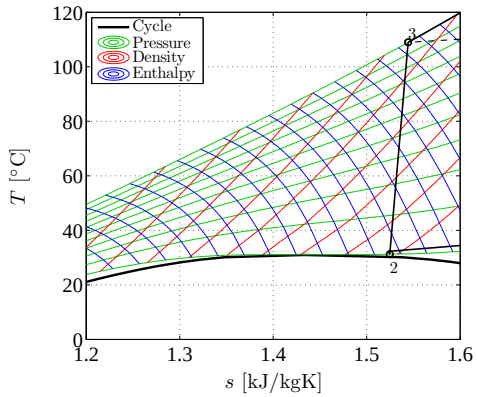

Figure 2-5: Compression T-s diagram ($P_2 = 74$ bar, $P_3 = 300$ bar, $\eta_{\mathrm{CM}} = 85\%$).

Figure 2-4b shows the regenerator load . Although the suction pressure does not have a considerable effect in the regenerator power, larger discharge pressure do influence the results and decrease the power of the regenerator because larger pressure ratios decrease the temperature difference between the cold and hot sides of the regeneration process.

Lower compressor suction temperatures do not considerably improve the performance of the cycle and additionally lower temperatures will bring the fluid to the liquid phase. This would involve supercritical condensation phenomena in the cooler, which should be preferable

avoided. Therefore, the compressor suction temperature of 31.25°C is a convenient value and it is taken for the analysis next sections.

2-2-2 Turbine and compressor efficiency effect

This section presents the analysis of analyzes the effects of the turbine and compressor efficiencies on the system performance. A chart showing the variation of the turbine inlet temperature and regenerator load as a function of these two variables is presented in Figure 2-6.

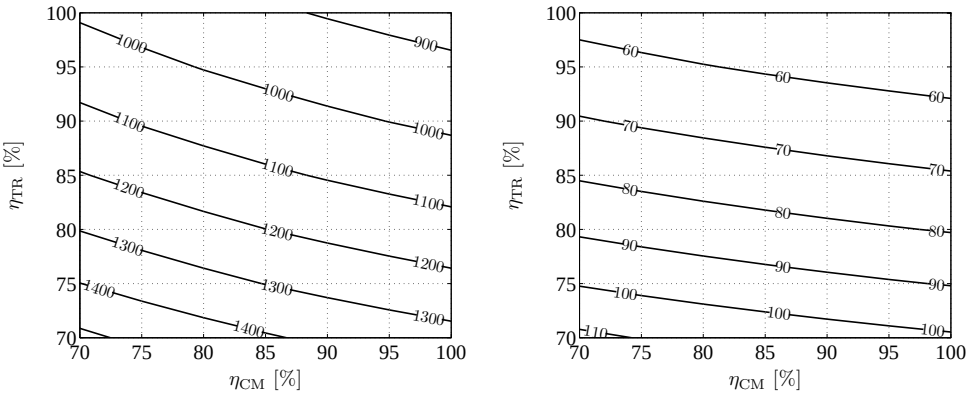

(a) Contour lines of T_4 (°C). **(b)** Contour lines of $\dot{Q}_{RG}$ (MW).

Figure 2-6: Turbine inlet temperature and regenerator load for the regenerative Brayton system as a function of the turbine and compressor adiabatic efficiencies ($\eta_{TR} = 50\%$, $T_2 = 31.25°C$, $P_2 = 74$ bar, $P_3 = 300$ bar, $\eta_{HR} = 90\%$, $\Delta P_{LS} = 2\%$, $\Delta T_{PN} = 10°C$).

Figure 2-6a presents the turbine inlet temperature as a function of the turbine and compressor efficiencies and it shows that the turbine efficiency has more influence on the system performance than the compressor efficiency, as expected. This is a consequence of the small power of the compressor when it is compared with that of the turbine. This feature is an advantage of the s-CO_2 power systems that was already mentioned in the first works of Feher [1]. It is produced by the high densities of the CO_2 in the critical region that reduce both the compressor work and its influence on the overall performance of the cycle. A sensitivity analysis is done on the compressor and turbine efficiencies to quantify the effect of both parameters.

Sensitivity refers to the effect that one variable has on another variable. The output analyzed here is the turbine inlet temperature. If the compressor efficiency changes from an initial value η_{CM0} to a value $\eta_{CM0} + \Delta\eta_{CM}$, also the TIT changes from an initial value of T_{TIT0} to a value $T_{TIT0} + \Delta T_{TIT}$. The sensitivity is given by the ratio of the relative changes of this variables [48],

$$\zeta = \frac{\Delta T_{TIT}/T_{TIT0}}{\Delta\eta_{CM}/\eta_{CM0}}. \tag{2-5}$$

The same principle applies for the turbine sensitivity analysis. The results of this calculation are shown in Figure 2-7. The starting efficiency for both compressor and turbine has been considered as 70%. The sensitivity of the turbine efficiency is more than twice the one of

the compressor efficiency, which indicates that the performance of the compressor has a low impact in the operation of the system compared with the performance of the turbine.

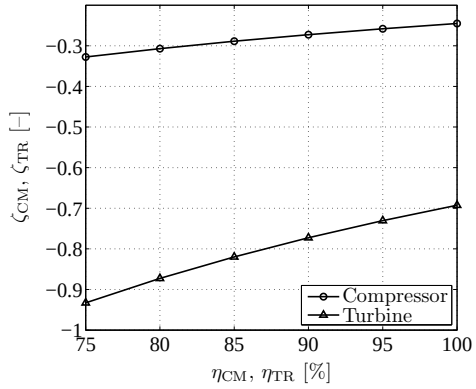

Figure 2-7: Sensitivity of the turbine and compressor efficiency in the regenerative Brayton system ($\eta_{CM0} = 70\%$, $\eta_{TR0} = 70\%$, $\eta_{TR} = 50\%$, $T_2 = 31.25°C$, $P_2 = 74$ bar, $P_3 = 300$ bar, $\eta_{HR} = 90\%$, $\Delta P_{LS} = 2\%$, $\Delta T_{PN} = 10°C$).

2-2-3 Regenerator effectiveness effect

This section documents the calculation of the turbine inlet temperature and the regenerator load as a function of the discharge pressure and regenerator effectiveness. The results are shown in Figure 2-8.

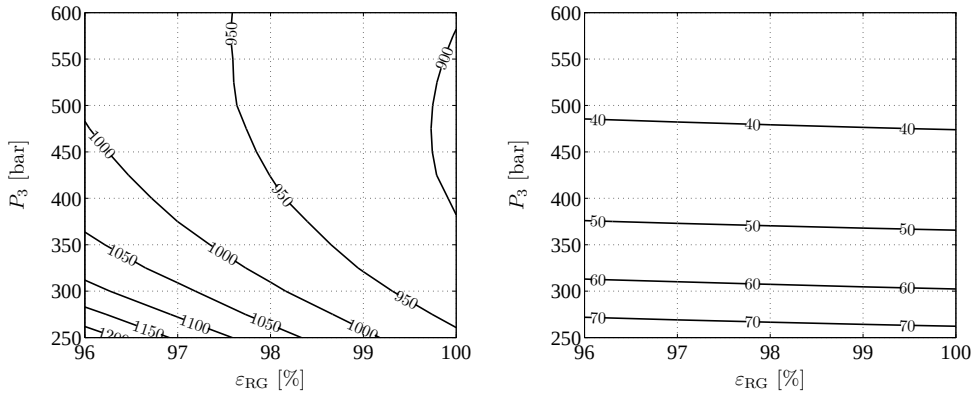

(a) Contour lines of T_4 (°C). **(b)** Contour lines of $\dot{Q}_{RG}$ (MW).

Figure 2-8: Turbine inlet temperature and regenerator load for the regenerative Brayton system as a function of the regenerator effectiveness and compressor discharge pressure ($\eta_{TR} = 50\%$, $T_2 = 31.25°C$, $P_2 = 74$ bar, $\eta_{TR} = 93.4\%$, $\eta_{CM} = 85\%$, $\eta_{HR} = 90\%$, $\Delta P_{LS} = 2\%$).

The effect of the discharge pressure is discussed in Section 2-2-1. Regarding the influence of the regenerator effectiveness, higher values improve the thermal energy recovery and therefore decrease the TIT, as shown in Figure 2-8a. Notice that the influence of the effectiveness

decreases with larger pressure ratios. Lower TITs decrease the regeneration temperature difference between cold and hot extremes and therefore result in a lower regenerator load. However, higher effectiveness values allow lower pinch temperatures and maintains almost constant the regeneration power, as shown in Figure 2-8b. The minimum effectiveness of 96% gives pinch temperatures between 20 and 40°C at discharge pressures of 250 and 600 bar respectively. These temperature differences are quite large and therefore no lower values of effectiveness are considered.

2-2-4 Pressure loss effect

The effect of the pressure drop is analyzed in this section by means of the calculation of the TIT as a function of the compressor discharge pressure and the pressure loss, as presented in Figure 2-9a. As shown in Section 2-2-1, larger pressure ratios decrease the TIT. Regarding the pressure losses, lager values lead to higher TIT and higher regeneration power due to the fact that it is necessary to increase both values to maintain the required thermal efficiency of 50%.

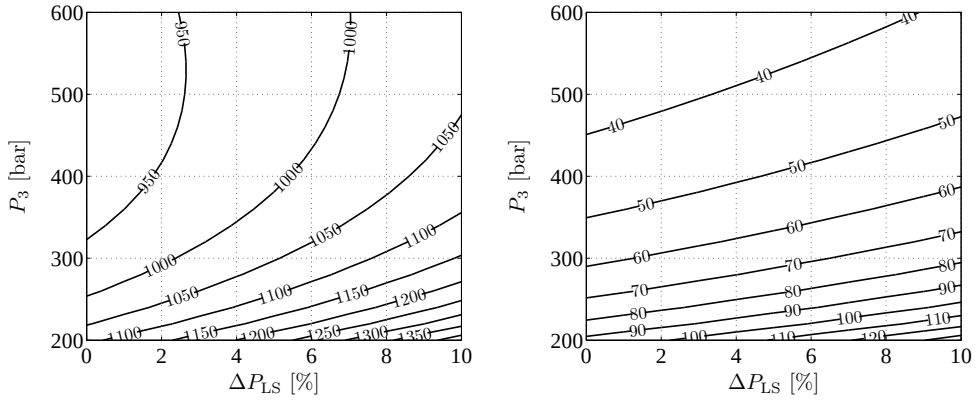

(a) Contour lines of T_4 (°C). **(b)** Contour lines of $\dot{Q}_{RG}$ (MW).

Figure 2-9: Turbine inlet temperature and regenerator load for the regenerative Brayton system as a function of the pressure loss and compressor discharge pressure ($\eta_{TR} = 50\%$, $T_2 = 31.25°C$, $P_2 = 74$ bar, $\eta_{TR} = 93.4\%$, $\eta_{CM} = 85\%$, $\eta_{HR} = 90\%$, $\Delta T_{PN} = 10°C$).

2-2-5 Operating conditions

This section presents the analysis of a particular set of operating conditions. There are several criteria available for the optimal choice of this set. The compressor discharge pressure, turbine inlet temperature and system pressure loss are examples of available options. In this stage of the work the minimum TIT is chosen. As shown in Figure 2-3a, there is a specific discharge pressure that gives the minimum TIT for a fixed pressure loss. It is possible therefore to calculate these minimum TITs with their correspondent discharge pressures as a function of the pressure loss, as shown in Figure 2-10.

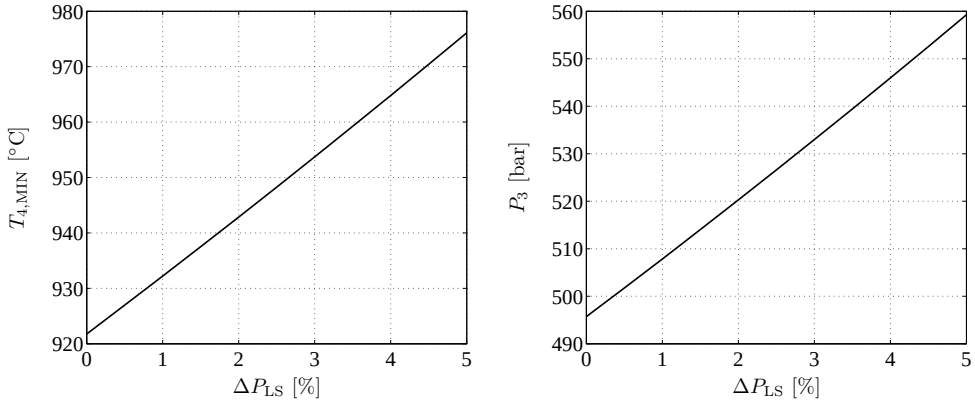

(a) Minimum TIT. **(b)** Discharge pressure.

Figure 2-10: Minimum turbine inlet temperature and its correspondent compressor discharge pressure for the regenerative Brayton system as a function of the pressure loss ($\eta_{\mathrm{TR}} = 50\%$, $T_2 = 31.25°\mathrm{C}$, $P_2 = 74$ bar, $\eta_{\mathrm{HR}} = 90\%$, $\Delta T_{\mathrm{PN}} = 10°\mathrm{C}$).

The chosen operating conditions correspond to a pressure loss of 2% (equivalent to 0.03 fractional pressure loss, calculated as $\Delta P_{\mathrm{TOTAL}}/P_3$), which is close to the state-of-the-art fractional pressure loss (0.04) [49] for Brayton power plants. This pressure loss corresponds to a minimum TIT of 943°C with a discharge pressure of 520 bar. The cycle T-s diagram is presented in Figure 2-11.

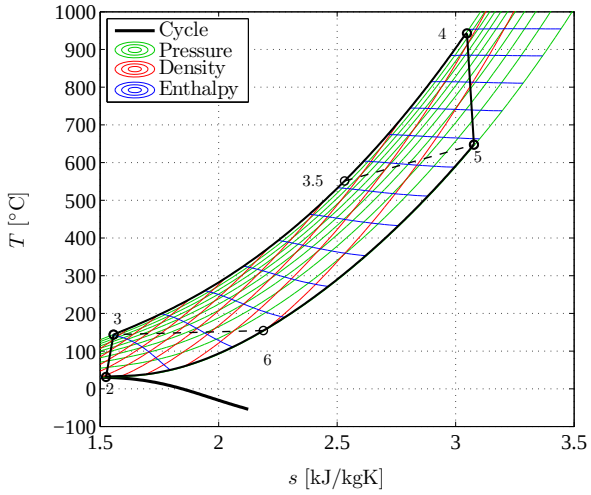

Cycle points	P [bar]	T [°C]
Comp. inlet (2)	74.00	31.25
Reg. cold side inlet (3)	520.28	143.94
Heater inlet (3.5)	520.28	551.33
Turb. inlet (4)	509.88	942.86
Reg. hot side inlet (5)	75.51	647.68
Cooler inlet (6)	75.51	154.56

Figure 2-11: Regenerative Brayton system T-s diagram ($\eta_{\mathrm{TR}} = 50\%$, $T_2 = 31.25°\mathrm{C}$, $P_2 = 74$ bar, $P_3 = 520.28$ bar, $\eta_{\mathrm{TR}} = 93.4\%$, $\eta_{\mathrm{CM}} = 85\%$, $\eta_{\mathrm{HR}} = 90\%$, $\Delta P_{\mathrm{LS}} = 2\%$, $\Delta T_{\mathrm{PN}} = 10°\mathrm{C}$).

The numbers in the chart correspond to those shown in Figure 2-1. As mentioned earlier, the pressure losses are placed at the turbine and compressor inlets. Notice that the CO_2 density varies between 43 kg/m^3 and 715 kg/m^3, which are high values that allow the design of very compact turbomachinery and compact heat exchangers, though the technological requirements are very demanding, and the equipment bound to be highly unconventional.

The temperature profile of the regenerator is shown in Figure 2-12. A counter current

heat exchanger has been assumed for this analysis. While both streams show an ideal gas behavior in the hot region of the heat exchanger, the cold extreme is close to the critical point, showing real gas effects. In this region, the slope of the heat capacities is not constant. As

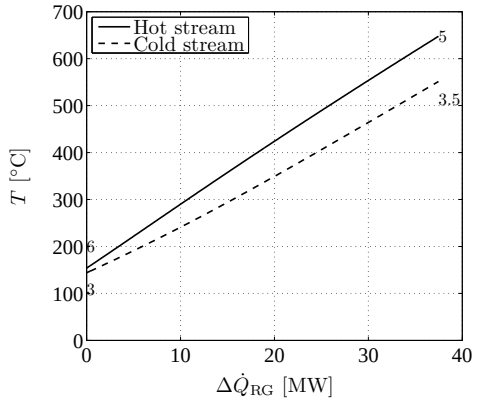

Figure 2-12: Regeneration temperature profile for the regenerative Brayton system ($\eta_{TR} = 50\%$, $T_2 = 31.25°C$, $P_2 = 74$ bar, $P_3 = 520.28$ bar, $\eta_{TR} = 93.4\%$, $\eta_{CM} = 85\%$, $\eta_{HR} = 90\%$, $\Delta P_{LS} = 2\%$, $\Delta T_{PN} = 10°C$).

a consequence the effectiveness of the heat exchanger decreases. Besides, the pinch point is not necessarily located at one of the extremes of the heat exchanger. Thus, the temperature difference is checked over the entire heat exchanger. The operating characteristics of the power system are presented in Table 2-3.

Table 2-3: Operating conditions for the regenerative Brayton system ($\eta_{TR} = 50\%$, $T_2 = 31.25°C$, $P_2 = 74$ bar, $P_3 = 520.28$ bar, $\eta_{TR} = 93.4\%$, $\eta_{CM} = 85\%$, $\eta_{HR} = 90\%$, $\Delta P_{LS} = 2\%$, $\Delta T_{PN} = 10°C$)

Variable		Value
Required CO_2 mass flow	kg/s	65.22
Regenerator effectiveness	%	97.89
Regenerator power	MW	37.47
Heater power	MW	33.67
Cooler power	MW	14.97
Compressor power	MW	5.71
Turbine gross power	MW	24.42

Notice that the regenerator power is the largest among the components. Feher [1] already mentioned this characteristic as an advantage of the s-CO_2 power cycles since it allows to recuperate large quantities of energy in the regeneration process. Similarly, the power of the compressor is 20% the power of the turbine, while in the typical Brayton systems the compressor power reaches values up to 50% the turbine gross power. This is another advantage of the s-CO_2 that allows high efficiencies at moderate TITs.

Exergy analysis

The exergy of an energy system is defined as the maximum work that can be produced by the combination of the system and a specified reference environment [50]. Exergy analysis of power plants is used to quantify the thermodynamic losses that cause exergy destruction, i.e.,

loss of potential to convert energy into work. It is therefore convenient to perform an exergy analysis to reveal the components causing the largest thermodynamic losses and therefore largest potential for improvement. First it is necessary to state the general exergy balance,

$$\text{Exergy entering} - \text{Exergy leaving} - \text{Exergy consumption} = \text{Exergy accumulation}. \tag{2-6}$$

No exergy accumulation is considered in the system, because steady-state operation is assumed. The exergy entering the energy conversion system is calculated as

$$E_{\mathrm{E}} = \left(1 - \frac{T_0}{\bar{T}_{\mathrm{H}}}\right) \dot{Q}_{\mathrm{E}}, \tag{2-7}$$

where T_0 corresponds to the environmental reference temperature, $\dot{Q}_{\mathrm{E}}$ and $\bar{T}_{\mathrm{H}}$ to the energy addition and the averaged temperature of this process respectively. Both the hot and cold averaged temperature are obtained as a function of the enthalpy and entropy values,

$$\bar{T}_{\mathrm{H}} = \frac{h_4 - h_{3.5}}{s_4 - s_{3.5}}, \tag{2-8}$$

$$\bar{T}_{\mathrm{C}} = \frac{h_6 - h_2}{s_6 - s_2}. \tag{2-9}$$

The subscripts correspond to the states shown in Figure 2-1. The exergy leaving the system corresponds to the net work output, the objective of the system. The exergy consumption corresponds to the exergy losses produced by the irreversibilities of each component, the destruction of exergy in the heat transfer processes and the exergy rejected by the cooler. The exergy loss in a fluid through a process reads

$$E_{\mathrm{LS}} = T_0 f \Delta s_{\mathrm{G}}, \tag{2-10}$$

where f is the mass flow rate and s_{G} is the entropy generated in the process. It is possible to apply this expression to obtain the losses in the the turbine and the compressor,

$$E_{\mathrm{LS,TR}} = T_0 f \left(s_5 - s_4\right), \tag{2-11}$$

$$E_{\mathrm{LS,CM}} = T_0 f \left(s_3 - s_2\right). \tag{2-12}$$

To calculate the exergy balance on the regenerator, it is necessary consider the exergy change of an open, steady state system,

$$\Delta E = f\left(\left(h_{\mathrm{E}} - h_{\mathrm{L}}\right) - T_0\left(s_{\mathrm{E}} - s_{\mathrm{L}}\right)\right). \tag{2-13}$$

The exergy balance, applied to the the heat exchanger reads

$$\Delta E_{\mathrm{H}} - \Delta E_{\mathrm{C}} = E_{\mathrm{LS}}, \tag{2-14}$$

where ΔE_{H} corresponds to the exergy transferred from the hot fluid and ΔE_{C} to the exergy gained by the cold fluid. Combining expressions (2-13) and (2-14) the exergy loss in the regenerator is obtained,

$$E_{\mathrm{LS,RG}} = f T_0\left(\left(s_{3.5} - s_3\right) - \left(s_5 - s_6\right)\right). \tag{2-15}$$

The reversible power of this system is a function of the system temperatures and the thermal energy input,

$$\dot{W}_{\mathrm{RV}} = \left(1 - \frac{\bar{T}_{\mathrm{C}}}{\bar{T}_{\mathrm{H}}}\right) \dot{Q}_{\mathrm{E}}. \tag{2-16}$$

Finally, the exergetic efficiency is calculated with the reversible power and the cycle power,

$$\eta_{\mathrm{EX}} = \frac{\dot{W}_{\mathrm{CY}}}{\dot{W}_{\mathrm{RV}}}. \tag{2-17}$$

The results of the exergy analysis for this system are presented in Figure 2-13. The largest losses in exergy are produced by the regenerator. As shown in Figure 2-12, real gas effects limit the performance of this device. In order to improve this operating conditions, two regenerators are considered in the following section. The second component with the largest exergy losses is the cooler. Likewise, the vapor recompression system presented in the next section improves the operation of this component.

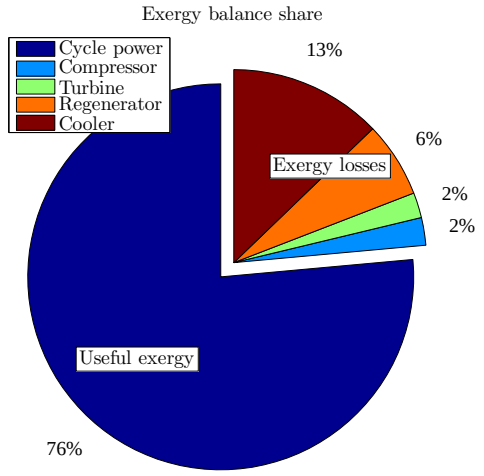

Component	Exergy loss [MW]
Regenerator	1.55
Cooler	3.13
Compressor	0.57
Turbine	0.52
Exergy efficiency	84.89 %

Figure 2-13: Cycle exergy balance for the regenerative Brayton system ($\eta_{\mathrm{TR}} = 50\%$, $T_2 = 31.25°\mathrm{C}$, $P_2 = 74$ bar, $P_3 = 520.28$ bar, $\eta_{\mathrm{TR}} = 93.4\%$, $\eta_{\mathrm{CM}} = 85\%$, $\eta_{\mathrm{HR}} = 90\%$, $\Delta P_{\mathrm{LS}} = 2\%$, $\Delta T_{\mathrm{PN}} = 10°\mathrm{C}$).

2-3 Brayton recompression system

This section is devoted to the analysis of the Brayton recompression system shown in Figure 2-14, which is a modification of the basic configuration of Section 2-2. This system includes two compressors and two regenerators in order to improve the energy transfer in the low temperature region of the regeneration process and reduce the energy rejection to the environment in the cooler. This configuration splits the mass flow f in two parts by means of the mass flow fraction α, which is calculated from an energy balance on the low temperature regenerator (regenerator 1 in Figure 2-14),

$$f(1-\alpha)(h_{3.3} - h_3) = f(h_{5.5} - h_6). \tag{2-18}$$

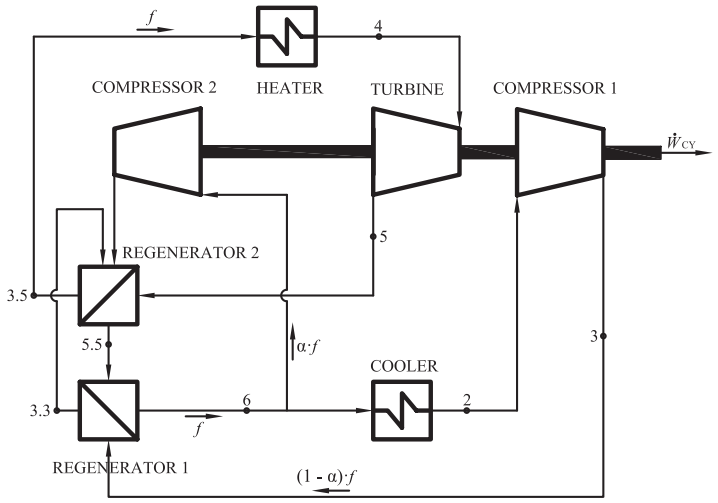

Figure 2-14: Process flow diagram of the Brayton recompression system.

The enthalpy $h_{3.3}$ depends on the high temperature compressor (compressor 2 in Figure 2-14) and its suction enthalpy and pressure in point 6. As mentioned earlier, the pinch is not necessarily located in the cold side of the low temperature regenerator, which is why it can not be assumed that $T_6 = T_3 + \Delta T_{\text{PN}}$. In order to calculate h_6 it is necessary to set a value for the mass flow fraction α, or set a value for the cold side temperature difference ($\Delta T_{\text{C,RG1}} = T_6 - T_3$). The latter is chosen in this work.

Additionally, the enthalpies 3.3 and 5.5 in expression (2-18) correspond to the cold side of the high temperature regenerator (regenerator 2 in Figure 2-14). The CO_2 in this component is not as close to the critical region as it is in the low temperature regenerator. It is reasonable then to assume that the pinch point for the regenerator 2 is located in the cold side of this heat exchanger. The temperature $T_{5.5}$ is therefore $T_{3.3} + \Delta T_{\text{PN}}$ and with this it is possible to obtain the enthalpy $h_{5.5}$. This assumption is confirmed in the temperature profile of Section 2-3-4.

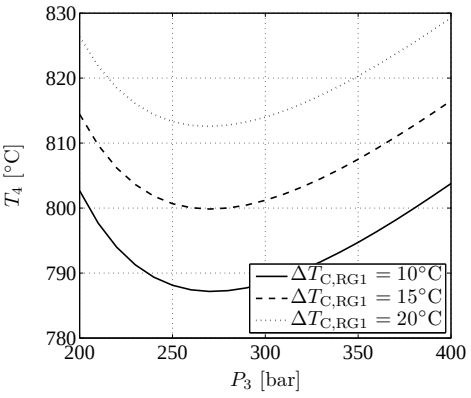

Figure 2-15: Turbine inlet temperature for the Brayton recompression system as a function of the compressor discharge pressure and cold side temperature difference, $\Delta T_{\text{C,RG1}}$, in the low temperature regenerator ($\eta_{\text{TR}} = 50\%$, $T_2 = 31.25°\text{C}$, $P_2 = 74$ bar, $\eta_{\text{TR}} = 93.4\%$, $\eta_{\text{CM1}} = 85\%$, $\eta_{\text{CM2}} = 85\%$, $\eta_{\text{HR}} = 90\%$, $\Delta P_{\text{LS}} = 2\%$, $\Delta T_{\text{PN}} = 10°\text{C}$).

The cold temperature difference, $\Delta T_{\text{C,RG1}}$ affects the mass flow fraction α in equation (2-18) and influences the performance of the system. In order to make the right assumption for this value it is necessary to evaluate the operation of the system as a function of this temperature difference, as shown in Figure 2-15. Lower values of $\Delta T_{\text{C,RG1}}$ are better for the the system since they lead to lower TITs. Therefore, the steady state balance for this system aims to fix the lowest temperature possible (i.e. the selected pinch) in the cold side of the low temperature regenerator. If this choice leads to lower pinch temperatures than the required one, $\Delta T_{\text{C,RG1}}$ is calculated in gradual increments until the pinch of 10°C is obtained.

The parameters presented in Table 2-2 are used in this section and the Brayton recompression system is analyzed as a function of the compressor discharge pressure. The results are shown in Figure 2-16. Figure 2-16a presents the TIT. The temperatures obtained in this

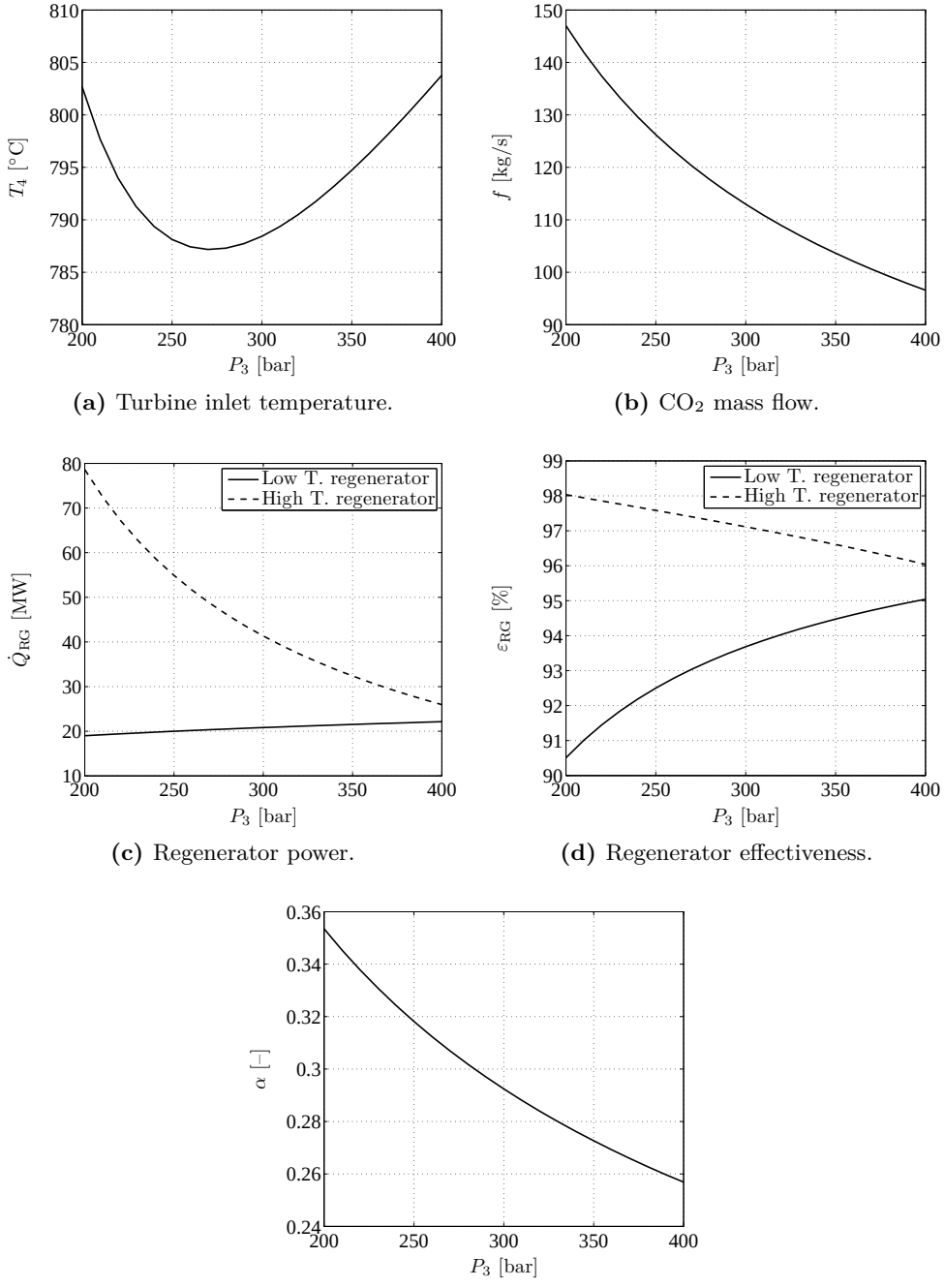

(a) Turbine inlet temperature.

(b) CO_2 mass flow.

(c) Regenerator power.

(d) Regenerator effectiveness.

(e) Mass flow fraction α.

Figure 2-16: Turbine inlet temperature, CO_2 mass flow rate, regenerator power, regenerator effectiveness and mass flow fraction for the Brayton recompression system as a function of the compressor discharge pressure ($\eta_{TR} = 50\%$, $T_2 = 31.25°C$, $P_2 = 74$ bar, $\eta_{TR} = 93.4\%$, $\eta_{CM1} = 85\%$, $\eta_{CM2} = 85\%$, $\eta_{HR} = 90\%$, $\Delta P_{LS} = 2\%$, $\Delta T_{PN} = 10°C$).

case are lower than those of the regenerative Brayton system. Notice that also the variation of the temperatures is lower and do not exceed 805 °C. The most important difference with the regenerative Brayton system is that the pressure correspondent to the minimum TIT is much lower, 270 bar approximately. The CO_2 mass flow, shown in Figure 2-16b, follows the expected trend. It decreases with larger pressure ratios since the specific work of the turbine increases. However, the vapor recompression system presents larger mass flow rates compared to the regenerative Brayton system since the turbine drives two compressors and only one operates close to the critical point. The mass flow therefore needs to increase in order to achieve the fixed target power of 18.7 MW.

The regenerator power and effectiveness, presented in Figures 2-16c and 2-16d respectively, decrease in the case of the high temperature regenerator and increase for the low temperature regenerator. In the first case, this is due to the increasing pressure ratio which decreases the temperature difference between the cold and hot side extremes of the heat exchanger and decreasing both the power and the effectiveness (the same effect is present in the Brayton regenerative cycle). The opposite effect is present in the low temperature regenerator.

The next sections present a similar analysis to the one of the regenerative Brayton system, i.e., the study of the influence of the components performance on the overall operation of the system.

2-3-1 Compressor suction temperature and discharge pressure effect

Figure 2-17 shows the variation of the turbine inlet temperature and the regenerators load as a function of the compressor suction temperature and discharge pressure. Both charts present similar behavior to those correspondent to the regenerative Brayton system presented in Figure 2-4. Figure 2-17a shows the TIT, which is relatively constant for suction temperatures lower than the critical temperature. Figure 2-17b present the total regenerator load, which remains almost unchanged. These effects have already been discussed in section 2-2-1.

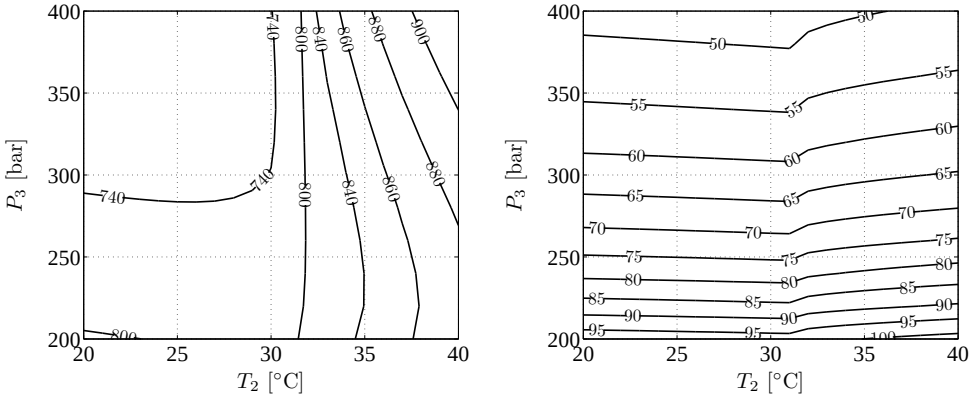

(a) Contour lines of T_4 (°C). **(b)** Contour lines of $\dot{Q}_{\mathrm{RG}}$ (MW).

Figure 2-17: Turbine inlet temperature and total regenerators load for the Brayton recompression system as a function of the compressor suction temperature and discharge pressure ($\eta_{\mathrm{TR}} = 50\%$, $P_2 = 74$ bar, $\eta_{\mathrm{TR}} = 93.4\%$, $\eta_{\mathrm{CM1}} = 85\%$, $\eta_{\mathrm{CM2}} = 85\%$, $\eta_{\mathrm{HR}} = 90\%$, $\Delta P_{\mathrm{LS}} = 2\%$, $\Delta T_{\mathrm{PN}} = 10°\mathrm{C}$).

2-3-2 Turbine and compressors efficiency effect

Figure 2-18 presents the TIT and the regenerators load as a function of the turbine and compressors adiabatic efficiencies. Though the system presents similar characteristics to the regenerative Brayton cycle shown in Figure 2-6, in this case the compressor efficiency plays a more important role because there are two compression processes in this configuration.

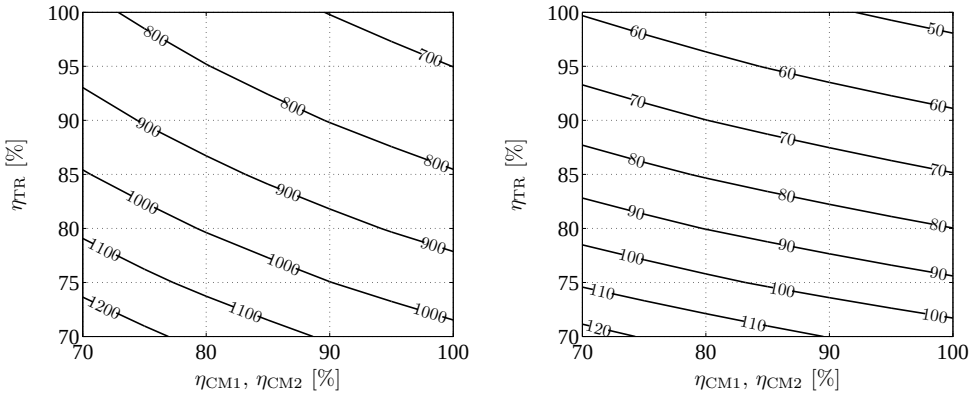

(a) Contour lines of T_4 (°C). **(b)** Contour lines of $\dot{Q}_{RG}$ (MW).

Figure 2-18: Turbine inlet temperature and total regenerators load for the Brayton recompression system as a function of the turbine and compressors efficiencies ($\eta_{TR} = 50\%$, $T_2 = 31.25°C$, $P_2 = 74$ bar, $P_3 = 300$ bar, $\eta_{HR} = 90\%$, $\Delta P_{LS} = 2\%$, $\Delta T_{PN} = 10°C$).

2-3-3 Pressure loss effect

Figure 2-19a shows the TIT as a function of the pressure losses and the discharge pressure.

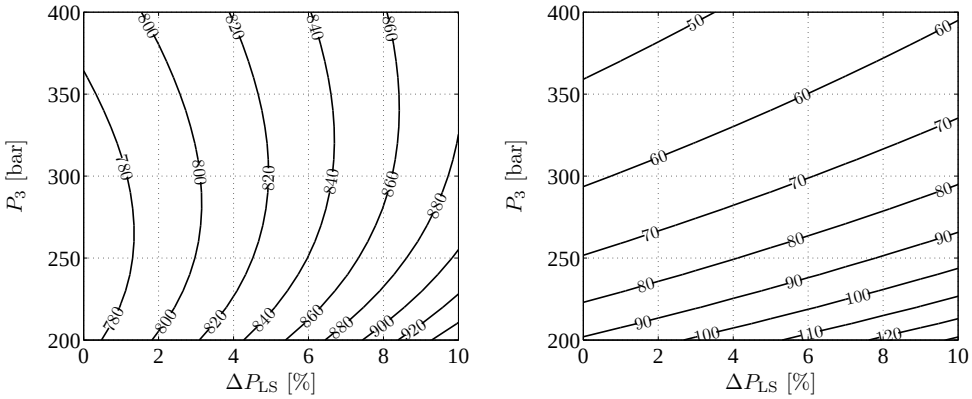

(a) Contour lines of T_4 (°C). **(b)** Contour lines of $\dot{Q}_{RG}$ (MW).

Figure 2-19: Turbine inlet temperature and total regenerators load for the Brayton recompression system as a function of the pressure loss and compressor discharge pressure ($\eta_{TR} = 50\%$, $T_2 = 31.25°C$, $P_2 = 74$ bar, $\eta_{TR} = 93.4\%$, $\eta_{CM1} = 85\%$, $\eta_{CM2} = 85\%$, $\eta_{HR} = 90\%$, $\Delta T_{PN} = 10°C$).

The trends are similar to those of the regenerative Brayton cycle presented in Figure 2-9, i.e., larger pressure losses require larger TIT and increasing the discharge pressure decreases

the TIT. However, the minimum TIT takes place at lower pressures in this configuration, which is why for a fixed pressure loss there is always a minimum TIT in Figure 2-19a. The trend of the regenerators load in Figure 2-19b is similar to that of the regenerative Brayton system. However, the values of the power are larger in this case since the vapor recompression system requires larger CO_2 mass flow.

2-3-4 Operating conditions

The same procedure followed for the first system configuration is used in this section to analyze a specific set of operating conditions for the Brayton recompression system. The minimum TIT and its correspondent discharge pressure are obtained for different pressure losses. The results are shown in Figure 2-20.

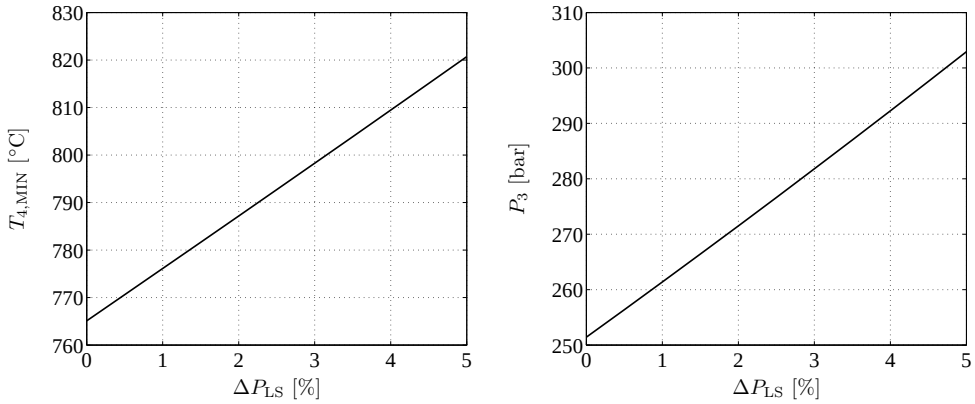

(a) Minimum TIT. **(b)** Discharge pressure.

Figure 2-20: Minimum turbine inlet temperature and its correspondent compressor discharge pressure for the Brayton recompression system as a function of the pressure loss ($\eta_{\mathrm{TR}} = 50\%$, $T_2 = 31.25°\mathrm{C}$, $P_2 = 74$ bar, $\eta_{\mathrm{HR}} = 90\%$, $\Delta T_{\mathrm{PN}} = 10°\mathrm{C}$).

The operating conditions used in this analysis correspond to a pressure loss of 2%, which gives a minimum TIT of 788°C and a discharge pressure of 272 bar. The correspondent T-s diagram is shown in Figure 2-21. Apart from the lower TIT, the most important feature of this system is the value of the discharge pressure, which is almost half the value required by the regenerative Brayton configuration.

The temperature profile of the regenerators is shown in Figure 2-22. One objective of the recompression system is to separate the low temperature stream in order to limit the real gas effects in the heat exchangers. Besides, both extremes of the low temperature regenerator are fixed to have a value as close possible to the pinch, which results in the almost parallel temperature profile presented in Figure 2-22a and improves the regeneration process. The temperature profile of the high temperature regenerator, shown in Figure 2-22b, shows the pinch located in the cold side of this heat exchanger, confirming the assumption made for the calculation of the mass flow fraction α in equation (2-18).

Another feature of the vapor recompression system is the improved operation of the cooler.

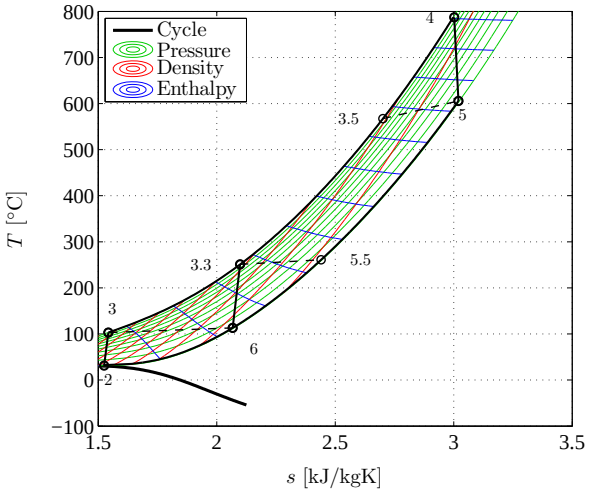

Cycle points	P [bar]	T [°C]
Comp. inlet (2)	74.00	31.25
Reg. 1 cold side inlet (3)	271.51	103.08
Reg. 2 cold side inlet (3.3)	271.51	250.98
Heater inlet (3.5)	271.51	567.31
Turbine inlet (4)	266.07	787.17
Reg. 2 hot side inlet (5)	75.48	605.73
Reg. 1 hot side inlet (5.5)	75.48	260.98
Cooler inlet (6)	75.48	113.08

Figure 2-21: Recompression Brayton system T-s diagram ($\eta_{TR} = 50\%$, $T_2 = 31.25°C$, $P_2 = 74$, $P_3 = 271.51$ bar, $\eta_{TR} = 93.4\%$, $\eta_{CM1} = 85\%$, $\eta_{CM2} = 85\%$, $\eta_{HR} = 90\%$, $\Delta P_{LS} = 2\%$, $\Delta T_{PN} = 10°C$).

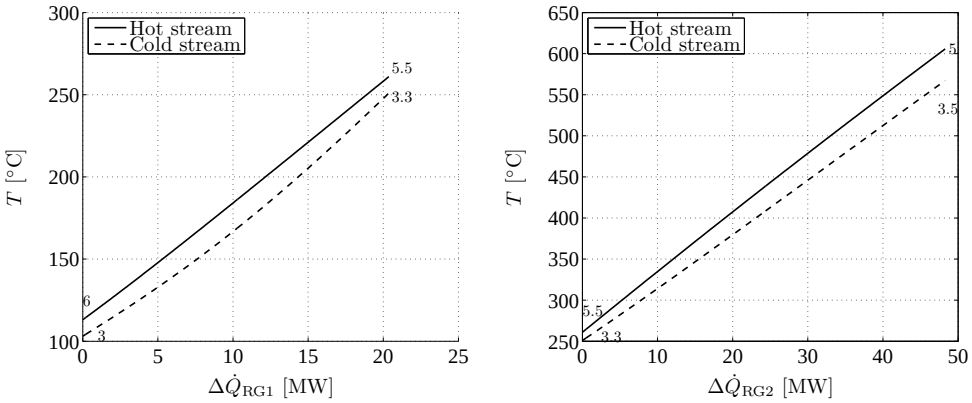

(a) Low T. regenerator profile. **(b)** High T. regenerator profile.

Figure 2-22: Regeneration temperature profiles for the Brayton recompression system ($\eta_{TR} = 50\%$, $T_2 = 31.25°C$, $P_2 = 74$, $P_3 = 271.51$ bar, $\eta_{TR} = 93.4\%$, $\eta_{CM1} = 85\%$, $\eta_{CM2} = 85\%$, $\eta_{HR} = 90\%$, $\Delta P_{LS} = 2\%$, $\Delta T_{PN} = 10°C$).

Consider Figure 2-14, though the complete mass flow f goes trough the heater, just a fraction of it $(1-\alpha)f$ passes trough the cooler, reducing the heat rejection in the cooler and improving the performance of the system. The operating conditions of this recompression configuration are presented in Table 2-4. Though the temperatures and pressures of this system are lower, the regeneration load and CO_2 mass flow are larger. Consequently, the weight of the components will increase as well, which will affect the design of the regenerators as shown in Chapter 3.

Table 2-4: Operating conditions for the Brayton recompression system ($\eta_{TR} = 50\%$, $T_2 = 31.25°C$, $P_2 = 74$, $P_3 = 271.51$ bar, $\eta_{TR} = 93.4\%$, $\eta_{CM1} = 85\%$, $\eta_{CM2} = 85\%$, $\eta_{HR} = 90\%$, $\Delta P_{LS} = 2\%$, $\Delta T_{PN} = 10°C$)

Variable		Value
Required CO_2 mass flow	kg/s	119.89
Mass fraction α	—	0.31
Regenerator 1 effectiveness	%	93.08
Regenerator 2 effectiveness	%	97.39
Regenerator 1 power	MW	20.37
Regenerator 2 power	MW	48.28
Heater power	MW	33.67
Cooler power	MW	14.97
Compressor 1 power	MW	3.72
Compressor 2 power	MW	4.03
Turbine gross power	MW	26.45

Exergy analysis

A procedure similar to the one of the previous section is followed. However, there are new thermodynamic states to be taken in account. Additionally, the mass flow used in the equations must be adjusted depending on the component. Considering these observations, the exergy balance is performed and the results are presented in Figure 2-23. As expected, the exergy efficiency is larger the one of the regenerative Brayton power cycle because of the better regeneration process and the lower heat rejection in the cooler, which has the largest percentage share in the exergy losses in this case.

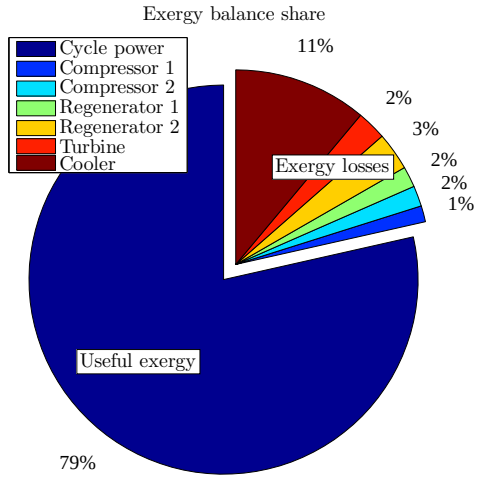

Component	Exergy loss [MW]
Regenerator 1	0.41
Regenerator 2	0.75
Cooler	2.64
Compressor 1	0.32
Compressor 2	0.41
Turbine	0.59
Exergy efficiency	86.16%

Figure 2-23: Cycle exergy balance for the Brayton recompression system ($\eta_{TR} = 50\%$, $T_2 = 31.25°C$, $P_2 = 74$, $P_3 = 271.51$ bar, $\eta_{TR} = 93.4\%$, $\eta_{CM1} = 85\%$, $\eta_{CM2} = 85\%$, $\eta_{HR} = 90\%$, $\Delta P_{LS} = 2\%$, $\Delta T_{PN} = 10°C$).

2-4 Regenerative Rankine system

This section presents the analysis of the regenerative Rankine system, whose process flow diagram is presented in Figure 2-24. In order to perform the thermodynamic analysis, it is necessary to define the s-CO_2 condensing temperature. Its value is chosen referring to the first study case of Chapter 4, in which the feasibility of s-CO_2 systems for aerospace applications is investigated. Because of the very low environmental temperatures present at cruise altitude (-50°C at 10670 m [51]), the condensing temperature is set to -20 °C (19.70 bar condensing pressure). The system is analyzed with the same parameters used in the other configurations with a pump efficiency of 85%. The results are presented in Figure 2-25.

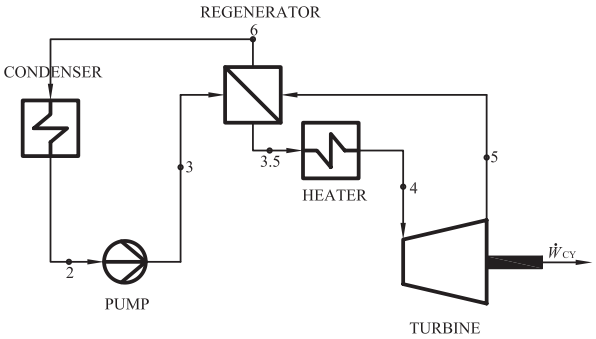

Figure 2-24: Process flow diagram for the regenerative Rankine system.

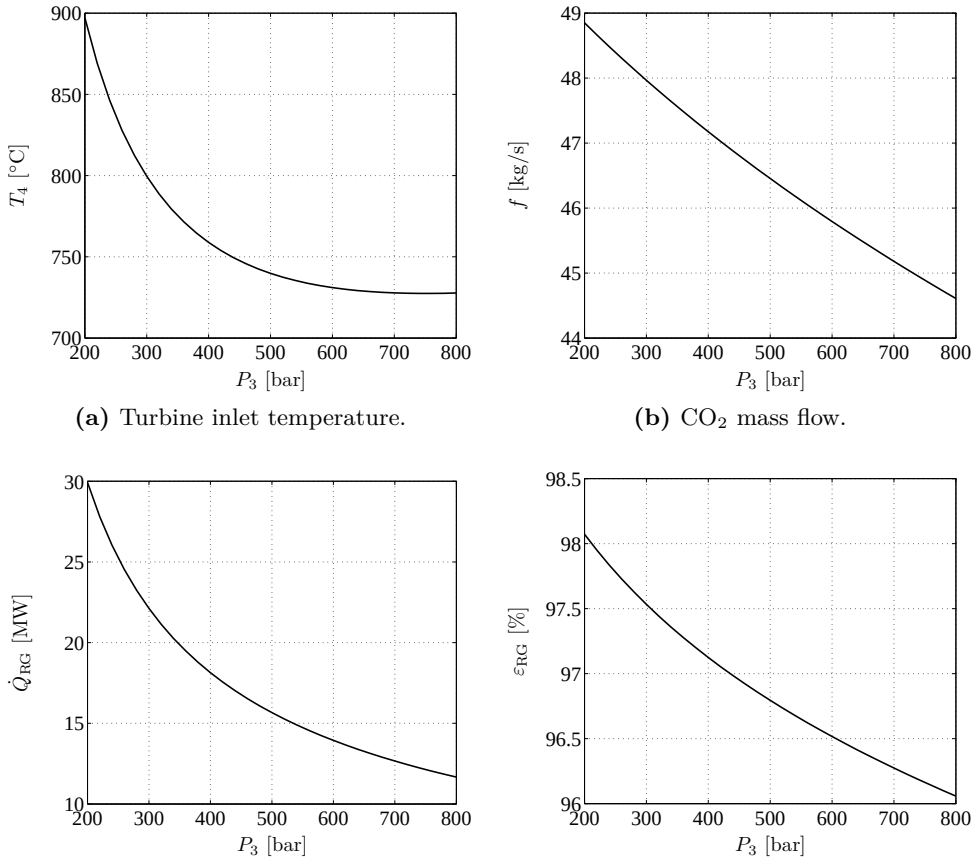

(a) Turbine inlet temperature.

(b) CO_2 mass flow.

(c) Regenerator power.

(d) Regenerator effectiveness.

Figure 2-25: Turbine inlet temperature, CO_2 mass flow rate, regenerator power and effectiveness for the regenerative Rankine system ($\eta_{TR} = 50\%$, $T_2 = -20°C$, $\eta_{TR} = 93.4\%$, $\eta_{PM} = 85\%$, $\eta_{HR} = 90\%$, $\Delta P_{LS} = 2\%$, $\Delta T_{PN} = 10°C$).

As expected, the trends of the analyzed variables are similar to those of the regenerative Brayton configuration in Figure 2-3. However, the ranges of the variables for the s-CO_2 Rankine system present better characteristics than those of the other configurations, i.e., lower TIT, lower CO_2 mass flow, lower regeneration power and regenerator effectiveness always in the accepted range ($\leq$ 98%). The minimum TIT of in Figure 2-25a has a value of 730°C and it is present at a discharge pressure of 750 bar approximately, which is a extremely large operating pressure and therefore the criterion to choose the specific operating conditions based on the minimum TIT should be changed.

The analysis of the operating conditions of the different components in the performance of the cycle is limited to the effect of the condensing temperature and the pump discharge pressure.

2-4-1 Condensing temperature and pump discharge pressure effect

The variation of the TIT and the regenerators load as a function of the condensing temperature and discharge pressure is presented in Figure 2-26. The temperatures do not cross the critical point and therefore the Contour lines of T_4 shown in 2-26a do not present sudden changes in their slope. Unlike both the regenerative and the vapor recompression Brayton systems, the suction temperature does have an influence on the TIT for the analyzed range in Figure 2-26a, i.e., lower suction temperatures decrease the TIT. Higher pressures decrease the TIT as well, which is a feature discussed in Section 2-2-1. Figure 2-26b presents the regeneration power. Both lower condensing temperature and higher discharge pressures reduce this power and are beneficial to decrease the size of the regenerators.

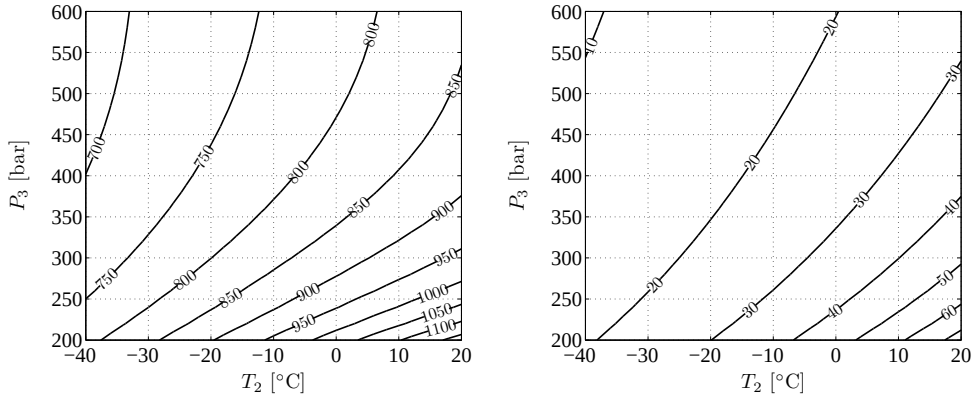

(a) Contour lines of T_4 (°C) **(b)** Contour lines of $\dot{Q}_{RG}$ (MW)

Figure 2-26: Turbine inlet temperature and regenerator load contour plot for the regenerative Rankine system as a function of the condensing temperature and pump discharge pressure (η_{TR} = 50%, η_{TR} = 93.4%, η_{PM} = 85%, η_{HR} = 90%, ΔP_{LS} = 2%, ΔT_{PN} = 10°C).

2-4-2 Operating conditions

As mentioned earlier, the minimum TIT for the Rankine system with a 2% pressure loss takes place at a very high pressure of 750 bar approximately. Therefore, the minimum TIT is not

a feasible criteria to choose a particular set of operating conditions. The discharge pressure of the operational point for the vapor recompression system in Section 2-3-4 is chosen (272 bar). The results are presented in Figure 2-27.

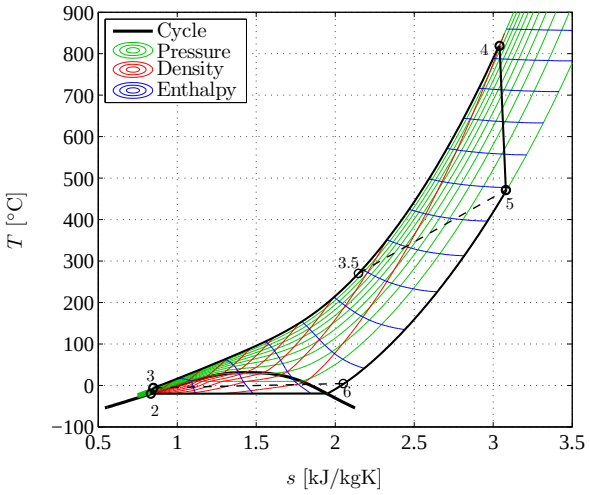

Cycle points	P [bar]	T [°C]
Pump inlet (2)	19.70	-20.00
Reg. cold side inlet (3)	271.51	-5.94
Heater inlet (3.5)	271.51	270.24
Turb. inlet (4)	266.08	818.73
Reg. hot side inlet (5)	20.10	471.03
Cooler inlet (6)	20.10	4.60

Figure 2-27: Regenerative Rankine system T-s diagram ($\eta_{TR} = 50\%$, $T_2 = -20°C$, , $P_3 = 271.51$ bar, $\eta_{TR} = 93.4\%$, $\eta_{PM} = 85\%$, $\eta_{HR} = 90\%$, $\Delta P_{LS} = 2\%$, $\Delta T_{PN} = 10°C$).

The turbine inlet temperature is higher than that correspondent to the vapor recompression system. However, as indicated later, the regeneration load and CO_2 mass flow is much lower. The regenerator temperature profile is presented in Figure 2-28.

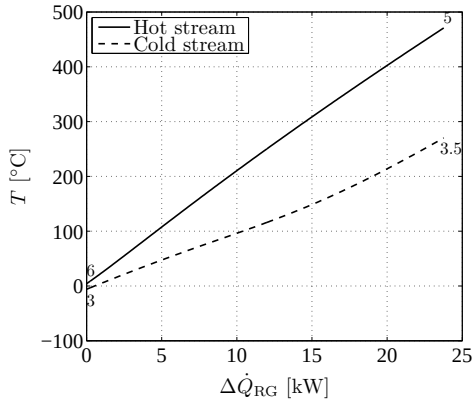

Figure 2-28: Regenerator temperature profile for the Regenerative Rankine system ($\eta_{TR} = 50\%$, $T_2 = -20°C$, , $P_3 = 271.51$ bar, $\eta_{TR} = 93.4\%$, $\eta_{PM} = 85\%$, $\eta_{HR} = 90\%$, $\Delta P_{LS} = 2\%$, $\Delta T_{PN} = 10°C$).

The pinch temperature is present at the cold extreme of the regeneration process and limits the performance of the heat exchanger. This is produced by the real gas effects that influence the properties of the streams. Besides, condensation takes place for the cold stream, which changes the heat capacity and slope of the temperature profile. The operating conditions of this specific case are presented in Table 2-5.

Both the regenerator load and the CO_2 mass flow are much lower than those correspondent to the regenerative and the vapor recompression Brayton systems. Regarding the aerospace

Table 2-5: Operating conditions for the regenerative Rankine system ($\eta_{TR} = 50\%$, $T_2 = -20°C$, $P_3 = 271.51$ bar, $\eta_{TR} = 93.4\%$, $\eta_{PM} = 85\%$, $\eta_{HR} = 90\%$, $\Delta P_{LS} = 2\%$, $\Delta T_{PN} = 10°C$).

Variable		Value
Required CO_2 mass flow	kg/s	48.21
Regenerator effectiveness	%	97.67
Regenerator power	MW	23.77
Heater power	MW	33.67
Cooler power	MW	14.97
Pump power	MW	1.36
Turbine gross power	MW	20.06

application study case of Section 4-1, it can be concluded that this system is the most beneficial for cruise conditions since the weight of the components is likely the lowest between the three s-CO_2 configurations studied so far. However, take off conditions and supercritical condensation of carbon dioxide add much more complexity to the system. Thus, this configuration is not considered in the next chapters of this study.

Regarding stationary power generation applications, the condensing temperature of -20°C is not feasible for this objective, and Rankine cycles with CO_2 require fluids with temperatures lower than the critical one (30.98°C) to be used as the thermal sink in the heat rejection process. Although water can be used for this aim, it is preferable to design dry coolers in order to reduce water pollution and environmental impacts. Future investigations should consider the variation of the critical temperature using CO_2 mixtures in order to adjust the critical temperature to levels that ease the operation of Rankine systems with air as the thermal sink.

Exergy losses

Following a similar procedure to that of the previous sections, the exergy analysis is done and presented in Figure 2-29. The main exergetic losses are present in the regenerator and

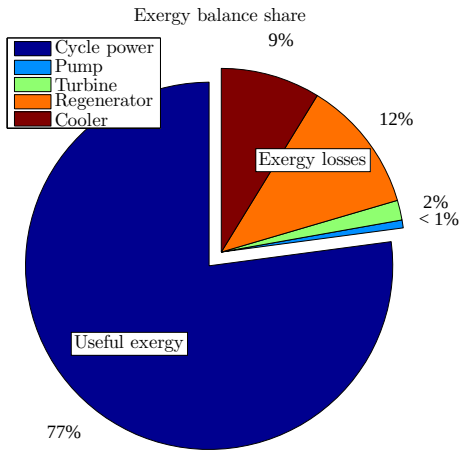

Component	Exergy loss [MW]
Regenerator	2.84
Cooler	2.13
Pump	0.17
Turbine	0.42
Exergy efficiency	82.39 %

Figure 2-29: Cycle exergy balance ($\eta_{TR} = 50\%$, $T_2 = -20°C$, , $P_3 = 271.51$ bar, $\eta_{TR} = 93.4\%$, $\eta_{PM} = 85\%$, $\eta_{HR} = 90\%$, $\Delta P_{LS} = 2\%$, $\Delta T_{PN} = 10°C$).

the cooler, which is a similar result to that obtained in the regenerative Brayton system. However, in this case the pump shares a very small amount of the losses, which is expected since the compressibility of the CO_2 is lower in the liquid phase that in the critical region, which reduces the compression work.

2-5 Overall comparison

This section presents a comparison between the regenerative and the recompression Brayton systems in an attempt to identify the best features of each configuration. The Rankine configuration is not further considered, as explained in Section 2-4-2. The parameters in Table 2-2 regarding the characteristics of the components and the system are used in this section. The TIT, CO_2 mass flow rate, regenerator power and regenerator effectiveness are calculated as a function of the discharge pressure. The results are presented in Figure 2-30.

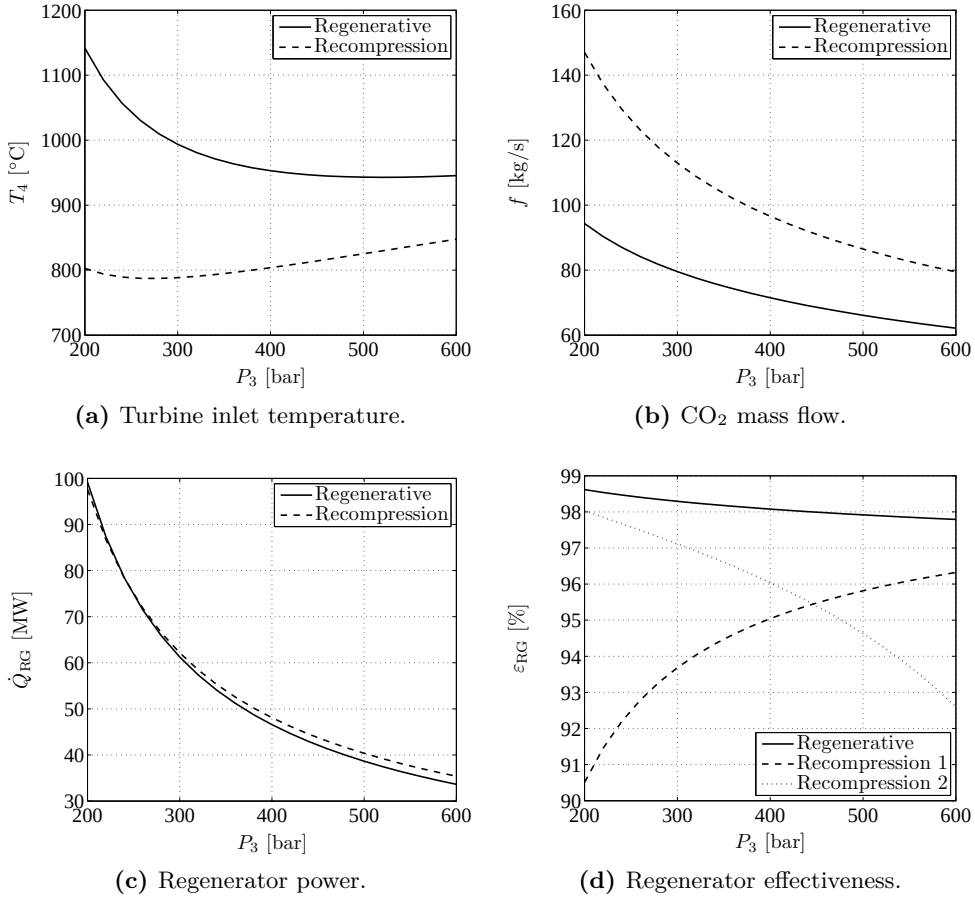

(a) Turbine inlet temperature.

(b) CO_2 mass flow.

(c) Regenerator power.

(d) Regenerator effectiveness.

Figure 2-30: TIT, CO_2 mass flow rate, regenerator power and effectiveness as a function of the compressor discharge pressure for the s-CO_2 regenerative and recompression Brayton power systems (η_{TR} = 50%, T_2 = 31.25°C, P_2 = 74 bar, η_{TR} = 93.4%, η_{CM1} = 85%, η_{CM2} = 85%, η_{HR} = 90%, ΔP_{LS} = 2%, ΔT_{PN} = 10°C).

The Brayton recompression system presents better characteristics than the Brayton regen-

erative system for stationary power applications since it has lower TITs for the same compressor discharge pressures, the regenerator power is almost the same and the effectiveness is always lower than the imposed limit ($\leq 98\%$). However, the recompression configuration requires a larger CO_2 mass flow, which will increase the size of the heat exchangers in the system. In order to establish an accurate comparison, the design procedures for the heat exchangers in the next chapter are applied to both Brayton configurations.

Chapter 3

Components design

This chapter describes the steady state design of the regenerators and the cooler. The dimensioning of the turbomachinery is not treated in this work and the design of the heater is considered in the next chapter for a specific application. The thermodynamic analysis performed previously gives the operating conditions which are used as inputs for the components design, which include several steps:

- analysis of material and geometrical characteristics,
- development of the calculation procedure for the dimensions of the components,
- validation and selection of correlations for the overall heat transfer coefficient and pressure drop,
- application of the dimensioning procedure to calculate the key characteristics of the heat exchangers.

3-1 Regenerators

As shown in the thermodynamic analysis, the regenerators share the largest power among the components of the system and then it is necessary to consider compact heat exchangers in order to keep their dimensions and weight as low as possible. In this regard, there is an increasing interest in Printed Circuit Heat Exchangers (PCHE) and there are already several theoretical and experimental studies about the application of such devices with s-CO_2 [16, 23, 26, 27]. All the referenced works recommend using PCHE due to several reasons that will be explained in the next section.

3-1-1 PCHE description

These heat exchangers are constituted by several metal plates which are photo-chemically etched on one side using a technology similar to that used for electronic circuits, hence the

name PCHE. The plates are joined by a technique called diffusion bonding, which includes a thermal process that allows grain growth and produces a free join interface between the plates [52]. The final result is a monolithic metal block which inherits all the properties

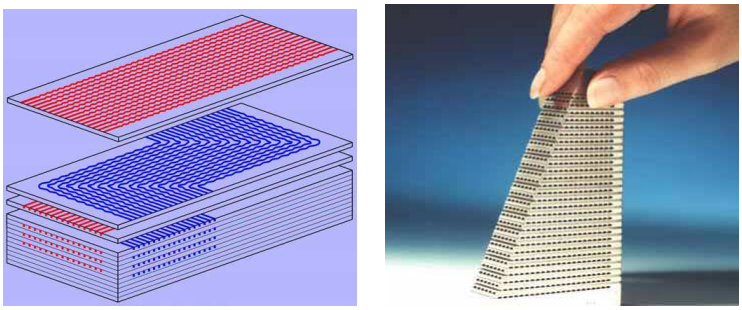

(a) Metal plates

(b) Section of the block

Figure 3-1: PCHE plates and section of the final block [2].

of the original material. The benefits of such process are very high pressure containment capabilities, avoidance of corrosion cells, possibility of channels with very small diameters, high effectiveness and tolerance to high temperatures. Figure 3-1 presents a diagram of the plates and a picture of a PCHE section.

Figure 3-1a shows the metal plates that can be identified with different colors according to the hot and cold sides of the heat exchanger. Each plate corresponds to a different side, but it is possible to assign two or more plates to a specific stream. The diameters of the channels are approximately semicircular in cross section with diameters between 1.0 and 2.0 mm. However, it is possible to obtain smaller diameters with values of 0.1 mm [16]. The channels can be straight or wavy, but the last option is preferable since it enhances the heat transfer and decreases the component size. Although the maximum dimensions of a PCHE core are 0.6x0.6x1.5 m [16], the core blocks can be welded together to increase the flow capacity until the required values are reached. The typical characteristics of these devices are shown in Figure 3-2.

Characteristic		**Value**
Unit weight	kg	1 - 60000
Max. design P	bar	650
Design T	°C	-271.25 - 900
Area/unit volume	m^2/m^3	1300 (100 bar)
	m^2/m^3	650 (500 bar)
Minimum pinch	°C	1
Maximum effectiveness	%	98.00
Overall HTC	W/m^2	LP gas cooler 500 - 1000
	W/m^2	HP gas cooler 1000 - 4000
Plate thickness	mm	0.5 - 5.0
Passage width	mm	0.5 - 5.0
Reynolds number	—	Gases: 1000 - 100000
	—	Liquids: 10 - 5000

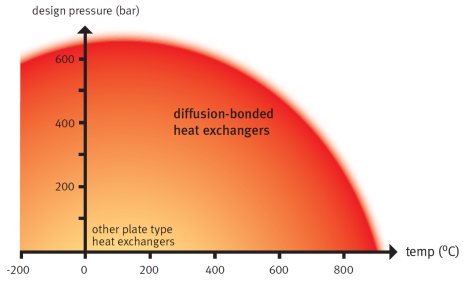

Figure 3-2: PCHE Typical characteristics and operational envelope [3].

The weight of the single units can reach values up to 60 tonne, and larger weights can be achieved if several units are joined together. It is possible then to adapt the PCHE to a wide range of operating conditions. Though the maximum pressure is 650 bar, the maximum value in practice will depend on the working temperature as well, as shown in the operational envelope of Figure 3-2. The effectiveness of this type of heat exchangers is very high and experimental results have reported values close to 99% [53], which is much higher than the standard values for industrial gas turbine regenerators (90% [54]).

3-1-2 Material and geometrical characteristics

Song [4] investigates the performance of a PCHE for supercritical CO_2 applications and he obtains the internal geometry of heat exchanger. A schematic diagram of the PCHE section and a single channel are shown in Figure 3-3.

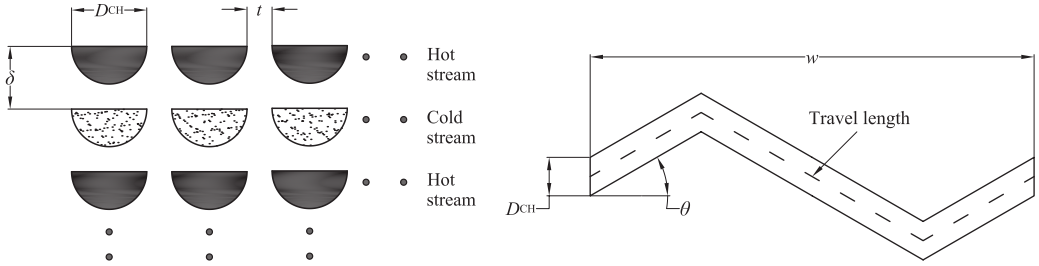

(a) PCHE cross section. **(b)** Channel top view.

Figure 3-3: Geometry of the section the core of a PCHE and top view of a single channel.

The design specifications from the manufacturer and the results of the calculations performed by Song are presented in Table 3-1. Notice that the travel length and the angles of the hot and cold sides are different due to the different number of channels. The density of the heat exchanger is close to that of steel itself (7990 kg/m^3 [55]) since it is almost a steel solid

Table 3-1: PCHE design specifications used in the work of Song [4]

Characteristic		**Hot side**	**Cold side**
Design pressure	bar	83	216
Design temperature	°C	200	200
Flow area	mm^2	1047	930
Number of channels		1176	1050
Hydraulic diameter	mm	0.92	0.92
Heat transfer area	m^2	5.6	5.6
Mass	kg	203	
Dimensions	mm	120 x 200 x 1200	
Material		SS 316	SS 316
Values calculated by Song			
Channel diameter	mm	1.51	1.51
Travel length	m	1.230	1.378
Wave angle (θ)	°	20.31	33.36
Plate thickness (δ)	mm	1.76	1.76
Plenum length	mm	49	46.5
Density	kg/m^3	7048.6	

block. In order to reduce the weight, a lighter material should be considered in this design. Titanium is an attractive option since it is a suitable material for the PCHE manufacturing process, it is corrosion resistant, and presents comparable mechanical characteristics to stainless steel [41].

The PCHE of the work of Song is the reference used in the next sections for the dimensioning of the regenerators. For the sake of simplicity, it is considered that the channel wave angle, number of channels and travel length are the same for both hot and the cold sides. Therefore, these parameters are obtained averaging the values given in Table 3-1. The geometry of the heat exchanger used in the present study is described in Table 3-2.

Table 3-2: PCHE parameters fixed for this work

Parameters		**Value**
Hydraulic diameter	mm	0.92
Channel diameter	mm	1.51
Plenum chamber length	mm	48.00
Wave angle (θ)	°	26.84
Sidewall thickness	mm	44.6
Top and bottom wall thickness	mm	32.5
Material		Titanium alloy grade 5

The sidewall and the top and bottom wall thickness are not presented in the work of Song. These values are taken from a similar analysis made by Meter [56]. The horizontal pitch and the plate thickness are of fundamental importance since they influence the final weight of the component. They are going to be reduced to their minimum value in order to decrease the heat exchanger dimensions as a function of the allowable stresses in the channels.

Wall and plate thickness, simplified stress analysis

As mentioned earlier, in order to decrease the PCHE volume and weight, it is necessary to evaluate the horizontal wall thickness (t in Figure 3-3) and the plate thickness (δ in Figure 3-3) to decrease them as much as possible. The method recommended by Hesslegraves [52] to calculate the horizontal pitch is used. The stress in the walls between horizontal channels, σ, is given by

$$\sigma = \Delta P \left(\frac{1}{Nt} - 1 \right), \tag{3-1}$$

where ΔP is the pressure difference between hot and cold sides and N is the number of walls between channels per meter. The number of walls per meter can be calculated using the horizontal pitch,

$$N = \frac{1}{t + D_{\mathrm{CH}}}. \tag{3-2}$$

Combining the last two expressions it is possible to obtain the minimum wall thickness,

$$t = D_{\mathrm{CH}} \frac{\Delta P}{\sigma}. \tag{3-3}$$

According to the last expression, t increases with higher pressure differences, and decreases with larger allowable stress. The stress is considered to be the yield stress of the material,

which is 450 MPa at a temperature of 538°C for titanium [57]. The pressure difference depends on the regenerator operating conditions.

The plate thickness is calculated considering the channels as thick cylindrical pressure vessels [16]. Since the titanium alloy can be considered a ductile material, the failure mode is associated with the maximum shear stress,

$$\tau_{\mathrm{MAX}} = \frac{R_{\mathrm{I}}^2 P_{\mathrm{I}}}{R_{\mathrm{O}}^2 - R_{\mathrm{I}}^2}. \tag{3-4}$$

It is possible to obtain plate thickness δ from the last expression,

$$\delta = \frac{D_{\mathrm{CH}}}{2}\left(\frac{P_{\mathrm{I}}}{\tau_{\mathrm{MAX}}} + 1\right)^{0.5}. \tag{3-5}$$

The internal radius R_{I} is replaced by the channel diameter $D_{\mathrm{CH}}/2$. Likewise, the external radio, R_{O} is replaced by the plate thickness δ. The yield shear stress is approximately 0.6 the tensile stress under nominal conditions [58]. Assuming this ratio as constant, the resultant shear stress is 270 MPa. Now it is possible to obtain the wall and plate thickness as a function of the internal channel pressure and the pressure difference between channels. The results are shown in Figure 3-4.

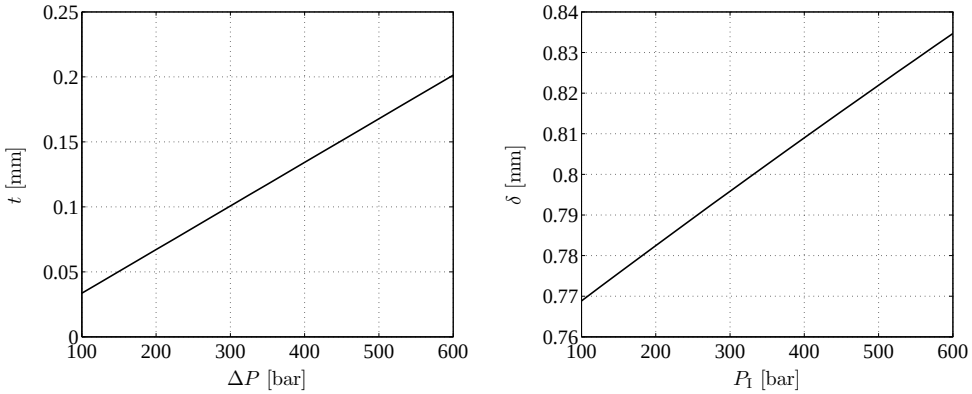

(a) Horizontal wall thickness. **(b)** Plate thickness.

Figure 3-4: PCHE wall thickness and plate thickness as a function of the pressure difference and the internal pressure.

Both the wall and plate thickness can be very small according to the results in Figure 3-4. Song reports a vertical wall thickness ($D_{\mathrm{CH}}/2 - \delta$ in Figure 3-3) of 1 mm. However, values as small as 0.5 mm are reported as well [59]. The latter value is taken in this work, which gives a horizontal pitch and plate thickness of 2.01 mm.

3-1-3 Overall heat transfer coefficient

The general equation for heat transfer reads

$$\dot{Q} = UA\Delta T_{\mathrm{LM}}, \tag{3-6}$$

where A stands for the heat transfer area and ΔT_{LM} for the logarithmic mean temperature difference. The overall heat transfer coefficient U is calculated with the contributions of the cold side, the hot side and the methal wall between them,

$$U = \frac{1}{\frac{1}{\alpha_{\mathrm{C}}} + \frac{\delta - 0.5 D_{\mathrm{CH}}}{\lambda_{RG}} + \frac{1}{\alpha_{\mathrm{H}}}}, \tag{3-7}$$

where α_{C} and α_{H} correspond to the heat transfer coefficient for the cold and hot sides respectively, δ stands for the plate thickness and λ_{RG} for the thermal conductivity of the heat exchanger material.

The heat transfer coefficient of the working fluid inside the channels is a function of the Nusselt number,

$$\alpha_{\mathrm{CH}} = \frac{Nu \lambda_{\mathrm{CH}}}{D_{\mathrm{HD}}}, \tag{3-8}$$

where D_{HD} corresponds to the hydraulic diameter of the semicircular channels,

$$D_{\mathrm{HD}} = \frac{D_{\mathrm{CH}}}{1 + \frac{2}{\pi}}, \tag{3-9}$$

and D_{CH} is the channel diameter. The thermal conductivity of the fluid can be obtained as a function of the pressure and temperature of the working fluid with the computational fluid library,

$$\lambda_{\mathrm{CH}} = \lambda(P, T). \tag{3-10}$$

There are several expressions available to calculate the Nusselt number for supercritical fluids. They have been developed for both straight channels and wavy channels, as shown in the next paragraphs.

Straight channels

The Gnielinski correlation is one of the most widely used relations and it is recommended by Hesslegraves [52],

$$Nu = \frac{\frac{F_{\mathrm{FI}}}{8} (Re - 1000) Pr}{1.0 + 12.7 \left(Pr^{\frac{2}{3}-1}\right) \sqrt{\frac{F_{\mathrm{FI}}}{8}}}, \tag{3-11}$$

where Pr corresponds to the Prandtl number and F_{FI} to the Filonenko friction coefficient,

$$F_{\mathrm{FI}} = \left[0.79 \ln (Re) - 1.64\right]^{-2}. \tag{3-12}$$

The Gnielinski correlation is valid for Reynolds numbers between 2300 and $5 \cdot 10^6$ and Prandtl numbers between 0.5 and 2000. Hesselgraves recommends a Nusselt number of 4.089 for laminar flows. Dostal [16] proposes an interpolation to calculate the Nusselt in the transition region between $Re = 2300$ and $Re = 5000$,

$$Nu = 4.089 + \frac{\mathrm{Nu}_{\mathrm{Re}=5000} - 4.089}{2300} (Re - 2300). \tag{3-13}$$

The Gnielinski equation (3-11) has been tested in different heat exchangers and conditions. Kruizenga et al. [40] study the heat transfer coefficient in a straight channel PCHE with

CO_2 under supercritical pressure and cooling conditions. They compare the results with several correlations and conclude that the Gnielinski equation gives results in good agreement with experimental data, within a difference of 20% at conditions far from the pseudocritical temperature. Additionally they report Nusselt numbers mostly overpredicted by values with an error close to 60% when the CO_2 is close to the pseudocritical region. Pettersen et al. [60] tested the Gnielinski correlation for supercritical CO_2 under cooling conditions for straight microchannel tubes. This study has good agreement with experimental results, with maximum errors of 15% in the calculation of the heat transfer coefficient.

Wavy channels

The literature regarding the detailed performance of wavy channels is scarce because of little information available from the manufacturer. Song [4] makes measurements in a PCHE and calculates the correspondent overall heat transfer coefficients. However, no comparison with analytical correlations is done. Carlson et al. [61] performs measurements of heat transfer and pressure in a PCHE with wavy channels and compares the results with several analytical expressions. They conclude that the Dittus Boelter and Gnielinski correlations underpredict the Nusselt number. Carlson proposes scaling the correlations with a factor of 3.8, which improves the results.

Another approach is related with the Colburn factor, which is usually used to calculate the Nusselt number for compact heat exchangers,

$$j = \frac{Nu}{RePr^{\frac{1}{3}}}, \tag{3-14}$$

Hesselgraves [52] gives an expression that correlates the Colburn factor with the Reynolds number in the channels,

$$j = 0.125Re^{-0.36}. \tag{3-15}$$

This correlation is valid for wavelength to width ratios close to 7. Kim et al. [39] test and confirm the validity of this expression for the mentioned wavelength to width ratio. Additionally, they develop correlations to predict the Nusselt number depending on the geometry of the channels. Although this study is performed using a Helium-Helium test loop, the results are used in this work since it is one of the few studies that develop correlations of the Nusselt number as a function of the geometry of the PCHE and the Reynolds number of the working fluid. The results of this analysis are expressed as a polynomial for the Nusselt number,

$$Nu = 4.089 + cRe^{d}, \tag{3-16}$$

where c and d are coefficients depending on the geometry of the PCHE. Notice how the lower the Reynolds number, the closer the Nusselt number to 4.089, which is the value recommended by Hesselgraves for laminar flow.

A recent study is carried out by Ngo et al. [42] with a modified Dittus Boelter correlation,

$$Nu = 0.1696Re^{0.629}Pr^{0.317}. \tag{3-17}$$

This expression is valid for Reynolds number between 3500 and 22000. A transition region is defined for lower Reynolds numbers and the calculation of the Nusselt number in this case is performed using an interpolation similar to the one of equation (3-13).

3-1-4 Pressure drop

The analysis of the pressure drop is done independently for straight and wavy channels, as shown in the next sections.

Straight channels

There are four types of losses contributing to the overall pressure drop in the regenerators, friction losses, acceleration losses, local losses and gravitational losses [40]. It is considered that the heat exchanger is horizontal, therefore the gravitational losses can be neglected. Local losses are produced by the contraction and expansion of the working fluid when it enters and leaves the channels. Dostal [16] calculates these losses with local loss coefficients,

$$\Delta P_{\mathrm{LC}} = C_{\mathrm{LC}} \rho \frac{v^2}{2}, \tag{3-18}$$

where v is the velocity of the fluid at the extremes of the channels, and C_{LC} stands for the loss coefficient, which has a value of 0.5 and 1.0 for the channels entrance and exit respectively. Acceleration losses are produced by the change of density in the heat exchanger,

$$\Delta P_{\mathrm{AC}} = G^2 \left(\frac{1}{\rho_{\mathrm{L}}} - \frac{1}{\rho_{\mathrm{E}}} \right), \tag{3-19}$$

where G is the fluid mass flux, and ρ_{E} and ρ_{L} are the densities of the fluid entering and leaving the channel respectively. Acceleration losses are negligible compared with the other losses and they are not considered in this work. This assumption is checked in Section 3-1-6. The friction losses are calculated with the Darcy-Weisbach equation,

$$\Delta P_{\mathrm{FR}} = F_{\mathrm{DR}} \frac{L}{D_{\mathrm{HD}}} \frac{\rho v^2}{2}, \tag{3-20}$$

where L is the length of the section. The Darcy friction factor F_{DR} is dependent on the Reynolds number and therefore it is different for each flow regime. For laminar flows with $Re < 2000$ the friction factor is calculated with the Hagen-Poiseuille law,

$$F_{\mathrm{DR}} = \frac{64}{Re}. \tag{3-21}$$

The departure Reynolds number is the limit for the laminar flow ($Re_0 = 2000$). It is independent from the pipe relative roughness with values smaller than 0.007. Otherwise, the departure Reynolds number has to be calculated [62],

$$Re_0 = 754 e^{\frac{0.0065}{\varphi}}, \tag{3-22}$$

where φ is the relative roughness. The transition region is limited between Re_0 and $Re = 4000$. The friction factor in this region is calculated by means of a linear interpolation between these boundaries. The Blasius law is considered for smooth tubes ($\varphi \leq 5 \cdot 10^{-6}$) and turbulent regimes ($Re \geq 4000$),

$$F_{\mathrm{DR}} = 0.3164 Re^{-0.25}. \tag{3-23}$$

The Colebrook-White equation is used for rough pipes ($\varphi > 5 \cdot 10^{-6}$),

$$F_{\mathrm{DR}} = \left[2\log\left(\frac{2.51}{Re\sqrt{F_{\mathrm{DR}}}} + \frac{\varphi}{3.7}\right)\right]^{-2}. \tag{3-24}$$

The last expression must be solved iteratively. In order to save computational time, the Serghides's approximate solution is used,

$$A = -2\log_{10}\left(\frac{\varphi}{3.7} + \frac{12}{Re}\right), \tag{3-25}$$

$$B = -2\log_{10}\left(\frac{\varphi}{3.7} + \frac{2.51A}{Re}\right), \tag{3-26}$$

$$C = -2\log_{10}\left(\frac{\varphi}{3.7} + \frac{2.51B}{Re}\right), \tag{3-27}$$

$$F_{\mathrm{DR}} = \left[A - \frac{(B-A)^2}{C - 2B + A}\right]^{-2}. \tag{3-28}$$

$$\tag{3-29}$$

This procedure gives a maximum of 0.4% error with Reynolds numbers between 10^4 and 10^8 and relative roughness between 10^{-6} and 10^{-1} [63].

Pettersen [60] shows that the Colebrook-White correlation is successful under cooling mode of s-CO_2 in circular microchannels. Kruizenga et al. [40] show that this correlation slightly over predicts the values measured in their experiments for straight channels in PCHE.

Wavy channels

Several authors obtain the friction pressure drop in wavy channels as a function of the Fanning friction factor [39,42,52], which is one fourth the Darcy friction factor used in equation (3-20) to calculate the friction pressure losses. Hesselgraves [52] obtains the Fanning factor for wavy channels as a function of the Reynolds number,

$$F_{\mathrm{FA}} = 11.0Re^{-0.53}. \tag{3-30}$$

Kim et al. [39] develop geometry-dependent correlations for a PCHE with a Helium-Helium test loop,

$$F_{\mathrm{FA}}Re = 15.78 + aRe^{b}, \tag{3-31}$$

where a and b depend on the geometry of the channels. Finally, Ngo et al. [42] define a different expression,

$$F_{\mathrm{FA}} = 0.1924Re^{-0.091}. \tag{3-32}$$

3-1-5 Calculation procedure

The calculation of the dimensions of the regenerator is performed by means of the discretization of the channels travel length in the heat exchanger. A schematic diagram of this procedure is shown in Figure 3-5. The chart presents a couple of channels correspondent to the hot and

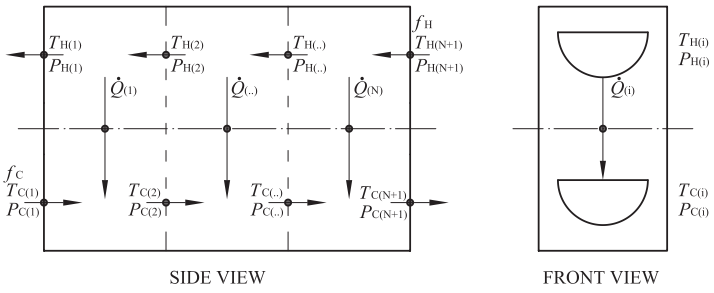

Figure 3-5: Side and front views of the discretization of the channels travel length used for the dimensioning of the regenerators.

cold sides of the heat exchanger. The side view indicates a counter current configuration. The nodes between each element have their own mass flow f pressure P and temperature T, with the subscripts H and C for the hot and cold sides respectively. It is assumed that the thermal energy $\dot{Q}_{(i)}$ is transferred only between each couple of channels. Additional assumptions are listed below,

- the CO_2 mass flow is equally distributed in all the channels,
- the properties at the beginning of the element are representative for the entire section,
- there are no thermal energy losses to the environment,
- heat transfer in the direction of the flow is neglected,
- the thermal power is equally distributed between channels.

The inlet temperature and pressure of both hot and cold extremes of the regenerator are known from the thermodynamic analysis. Thus, the properties of the fluids at node 1 in Figure 3-5 can be obtained. It is possible to calculate the heat transfer coefficient and the pressure drop for this element with the correlations described in the previous sections. Then, the area of the section can be obtained from the general heat transfer equation,

$$A_{(i)} = \frac{\dot{Q}_{(i)}}{U_{(i)} \left| T_{(i+1)} - T_{(i)} \right|}. \tag{3-33}$$

The local heat transfer $\dot{Q}_i$ is a function of the regeneration load, the number of channels and the number of discretization elements,

$$\dot{Q}_{(i)} = \frac{\dot{Q}_{RG}}{N_{CH} N_{CV}}, \tag{3-34}$$

where $\dot{Q}_{RG}$ is the regeneration power, and N_{CH} is the number of channels of the hot or cold sides. The number of elements, N_{CV}, is set to 200 for the calculations performed in the next sections. The validity of this consideration is confirmed at the end of the validation procedure in Section 3-1-6.

The length of the section is calculated with the perimeter of the channel,

$$L_{(\mathrm{i})} = \frac{A_{(\mathrm{i})}}{p_{\mathrm{CH}}}, \tag{3-35}$$

where p_{CH} is the channel diameter. Once the length is known, it is possible to calculate the friction pressure drop of the element by means of equation (3-20). The fluid pressure in the next node is a function of the fluid pressure and the pressure loss in the current control volume,

$$P_{(\mathrm{i+1})} = P_{(\mathrm{i})} + \Delta P_{(\mathrm{i})}. \tag{3-36}$$

The mathematical sign of the pressure drop, $\Delta P_{(\mathrm{i})}$, is positive for the hot side and negative for the cold side. The total pressure drop in the regenerators is therefore

$$\Delta P_{\mathrm{RG}} = \Delta P_{\mathrm{LC,IN}} + \Delta P_{\mathrm{LC,OUT}} + \sum_{\mathrm{i}}^{N_{\mathrm{CV}}} \Delta P_{\mathrm{FR(i)}}. \tag{3-37}$$

The local losses $\Delta P_{\mathrm{LC,IN}}$ and $\Delta P_{\mathrm{LC,OUT}}$ are calculated with equation (3-18). The last member in expression (3-37) corresponds to the summation of the friction losses in each element.

The specific enthalpy change in the control volume can be calculated with the properties at the inlet of the node,

$$\Delta h_{(\mathrm{i})} = \frac{\dot{Q}_{(\mathrm{i})}}{f}. \tag{3-38}$$

The enthalpy in the next node is calculated with the enthalpy change and the enthalpy at the current node,

$$h_{(\mathrm{i+1})} = h_{(\mathrm{i})} + \Delta h_{(\mathrm{i})}. \tag{3-39}$$

The procedure indicated above is valid for both hot and cold sides of the control volume. Once the pressure and temperature of the next node are obtained, the calculation procedure is repeated for the next element until the energy balance is performed in all the control volumes.

Regenerators total pressure drop

The travel length of the regenerator and consequently the total pressure drop depend on the number of channels in equation (3-34). Thus, it is possible to vary this value until a specific pressure drop is matched. This is useful since the total pressure drop of the regenerators is calculated with information from the previous chapter, as shown in the following.

The thermodynamic analysis of Chapter 2 places the pressure losses in the turbine and the compressor. In order to obtain the losses per component it is assumed that the pressure drop of a specific component is proportional to its load,

$$\Delta P_{(\mathrm{i})} = \Delta P_{\mathrm{TOT}} \frac{\dot{Q}_{(\mathrm{i})}}{\dot{Q}_{\mathrm{TOT}}}. \tag{3-40}$$

The total pressure drop in the cold or hot side of the cycle is ΔP_{TOT}, $\dot{Q}_{\mathrm{i}}$ is the power of each component (heater, regenerator, cooler, etc.) and $\dot{Q}_{\mathrm{TOT}}$ is the total load on the cold or hot

side. As an example, the total power in the hot side of the vapor recompression system is the summation of the power of its components,

$$\dot{Q}_{\mathrm{TOT}} = \dot{Q}_{\mathrm{RG,HIGH}} + \dot{Q}_{\mathrm{RG,LOW}} + \dot{Q}_{\mathrm{CO}}, \tag{3-41}$$

where $\dot{Q}_{\mathrm{RG,HIGH}}$ is the high temperature regenerator load, $\dot{Q}_{\mathrm{RG,LOW}}$ is the low temperature regenerator load, and $\dot{Q}_{\mathrm{CO}}$ is the cooler load.

Equation (3-40) can be used for both cold and hot sides and consequently the regenerators will have a different pressure drop for each side. One of these results should be chosen as the target to be matched by equation (3-37). Further results in the components design show that the pressure drop in the hot side of the regenerator is larger and this is the value taken as an input for this calculation procedure. The dimensioning of the regenerator consists therefore in varying the number of channels (by varying the dimensions of the PCHE core) until the pressure drop in equation (3-37) matches the pressure drop calculated in equation (3-40).

3-1-6 Correlations validation

This section presents the validation of the correlations for the heat transfer coefficient and pressure drop. The calculation procedure explained earlier is applied in the real PCHE studied by Song [4]. The geometrical characteristics of the channels are reported in Tables 3-1 and 3-2. The performance rating of this heat exchanger is shown in Table 3-3.

Table 3-3: Performance rating of the PCHE studied by Song (given by Heatric) [4]

		Cold Side		**Hot Side**	
		In	**Out**	**In**	**Out**
Flow rate (gas)	kg/h	353.0	353.0	543.0	543.0
Flow rate (liquid)	kg/h	0.0	0.0	0.0	0.0
Temperature	°C	84.0	178.0	181.0	85.0
Pressure inlet/design	barg	201.0/216.2		74.0/82.5	
Pressure drop calc./allowed	bar	0.07/0.25		0.24/0.25	
Design heat load	kW	17.5			
Overall HTC, clean	W/m^{2}K	754.0			
LMTD (ΔT_{LMTD})	°C	1.8			
Corrected TD (ΔT_{TD})	°C	4.2			

The results of the calculation procedure are presented in Figure 3-6. The overall heat transfer coefficient is shown in Figure 3-6a. All the correlations predict values lower than the one of the manufacturer rating (754 W/m^{2}K). The correlation of Gnielinski is the one that predicts the lowest overall heat transfer coefficient because it is meant for straight channels. The other correlations consider the effect of the wavy geometry and predict closer values to the reference one, with the correlations of Hesselgraves presenting the best results.

The Hesselgraves heat transfer coefficient decreases when the streams approach the hot side of the heat exchanger. This is due to the trend of the Nusselt number, presented in Figure 3-6b. The hot stream has a larger Nusselt number and a negative slope leading to the same trend for U. The Nusselt number is proportional to the Reynolds number, shown in Figure 3-6c. The latter decreases in the hot stream and increases in the cold stream when

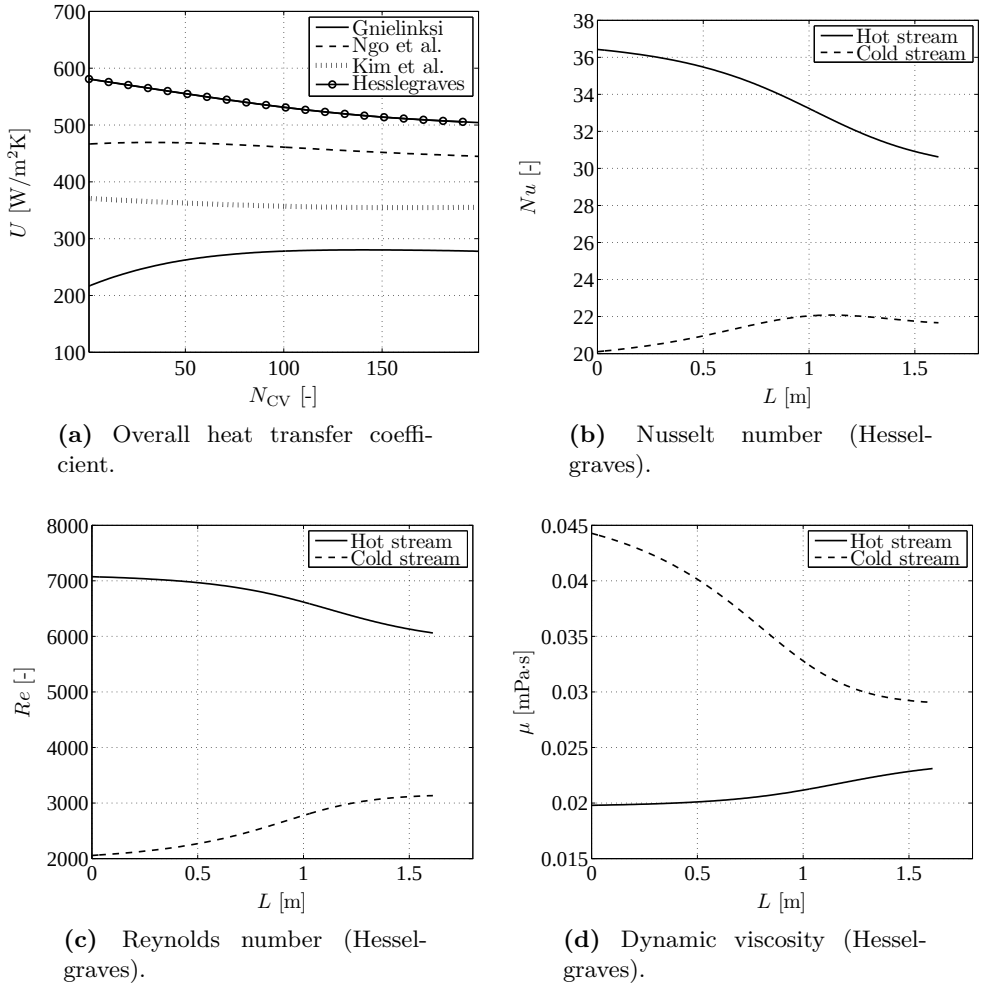

(a) Overall heat transfer coefficient.

(b) Nusselt number (Hesselgraves).

(c) Reynolds number (Hesselgraves).

(d) Dynamic viscosity (Hesselgraves).

Figure 3-6: Calculation of the overall heat transfer coefficient, Nusselt number, Reynolds number and dynamic viscosity for the PCHE in the work of Song [4] as a function of the number of control volumes (N_{CV}) and travel length (L).

they approach the hot extreme of the heat exchanger. The viscosity, shown in Figure 3-6d, is inversely proportional to Re and therefore presents the opposite trend.

The differences between the results provided by the correlations and the rating of the PHCE are presented in Table 3-4. The best prediction of the heat transfer coefficient is given by the correlations of Hesselgraves [52]. While the temperature errors are small for all the

Table 3-4: Differences of the temperature, pressure and length calculations between the design correlations and the PCHE rating given by Song

	Hot side			**Cold Side**		
	ΔT [%]	ΔP [bar]	L [%]	ΔT [%]	ΔP [bar]	L [%]
Gnielinski	0.21	0.11	-186.56	1.17	0.07	-156.78
Ngo et al.	0.00	-0.45	-54.66	1.20	0.15	-38.05
Kim et al.	0.18	0.03	-102.03	1.19	0.17	-80.33
Hesselgraves	0.00	-0.47	-31.02	1.21	0.10	-16.94

equations, the pressure drop calculation present large deviations in all the cases. Nevertheless, the correlations of Hesselgraves are chosen since they predict the best heat transfer coefficient and travel length. Further analysis should consider the improvement of the pressure drop prediction. The temperature profile of the PCHE according to the chosen correlations is presented in Figure 3-7.

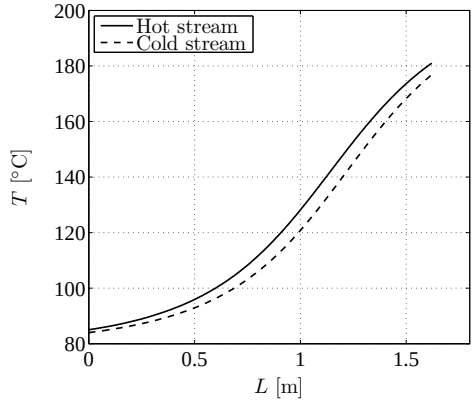

		Hot side		**Cold Side**	
		In	Out	In	Out
Temperature	°C	181.00 (181.00)	85.00 (85.00)	84.00 (84.00)	176.86 (176.90)
Pressure	bar	75.47 (75.00)	74.76 (74.76)	202.00 (202.00)	201.86 (201.30)
Travel length	m	1.61 (1.230)		1.61 (1.378)	
Heat transfer area	m^2	6.94 (5.60)		6.94 (5.60)	

Figure 3-7: PCHE temperature profile (according to the Hesselgraves correlations) as a function of the travel length. Values in parenthesis are those given by Heatric and reported by Song [4].

As already mentioned in Section 3-1-4, it is assumed that the acceleration losses are negligible. It is necessary to check the validity of this assumption and, in order to do so, the percentage values of the these losses compared with the friction losses are calculated and presented in Figure 3-8. The difference in magnitude indicates that the effect of the acceleration losses can be neglected and therefore the assumption is valid.

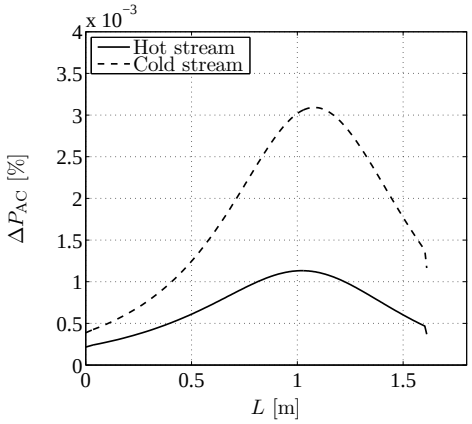

Figure 3-8: Percentage acceleration losses with with respect to friction losses as a function of the travel length.

Effect of the number of elements in the solution

In Section 3-1-5 it is mentioned that the number of discretization elements used in equation (3-34) is 200. However, it is convenient to study the convergence of the solution as a function of the number of discretization elements. To do so, the travel length calculated in this validation is plotted as a function of the number of control volumes, as shown in Figure 3-9. The length remains almost constant for a number of elements larger than 200 and consequently it is not necessary to consider larger values that would lead to larger computational cost.

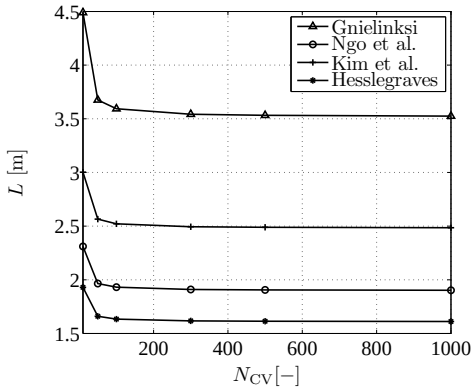

Figure 3-9: Converge of regenerators length for the PCHE of Song as a function of the number of sections.

3-1-7 Regenerators dimensioning

The regenerator core is considered to have a square section. Therefore, as described in Section 3-1-5, the side of the core is varied until the required pressure drop is matched. The actual volume of the material of the PCHE is calculated and multiplied times the density of the titanium alloy. Two parameters are used in the thermodynamic analysis to obtain the operating conditions, which are used in the dimensioning calculations. These parameters are the system pressure drop and the compressor discharge pressure. Figure 3-10 presents the weight of the regenerators as a function of these inputs.

The difference between the weights of the regenerators used in the Brayton configurations is large. This is due to the difference between the mass flow rates in both cases. As shown in Figure 2-30, the CO_2 mass flow in the recompression system is approximately 1.5 times larger than the one in the regenerative system and consequently the recompression configuration requires bigger equipment. Although the weight of the regenerators could be seen as an advantage for the regenerative cycle, recall that this system requires higher TITs, which brings additional challenges for the design of the heater and the materials of the rest of the components.

The weight of the rengenerators follows the same trend in both configurations shown in Figure 3-10. It decreases with larger pressure losses and larger compressor discharge pressures. Larger pressure losses require higher CO_2 mass flow rates, which increase the heat transfer coefficient, increase the pressure drop and consequently decrease the size of the heat exchanger.

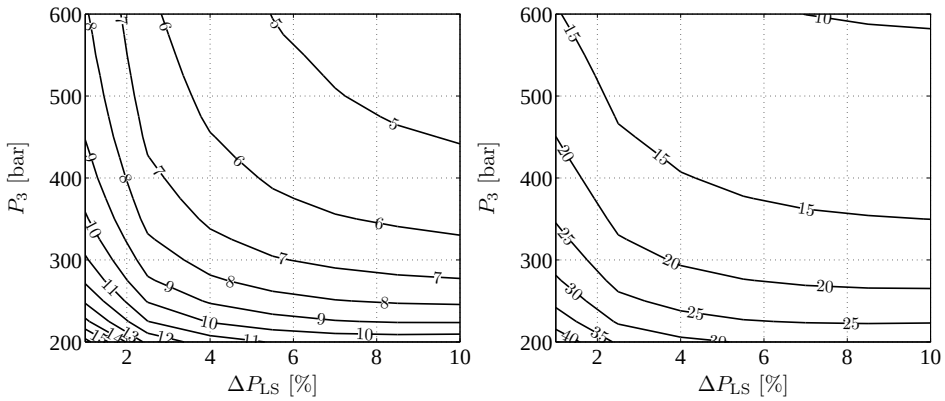

(a) Simple regenerative. **(b)** Vapor recompression.

Figure 3-10: Contour lines of the regenerators weight (tonne) as a function of the pressure drop and the discharge pressure for the regenerative and vapor recompression Brayton systems ($\eta_{TH} = 50\%$, $T_2 = 31.25°C$, $P_2 = 74$ bar, $\eta_{TR} = 93.4\%$, $\eta_{CM} = 85\%$, $\eta_{HR} = 90\%$, $\Delta T_{PN} = 10°C$).

Larger discharge pressures decrease the regeneration power and consequently decrease the heat exchanger size as well.

Finally, in order to have a grasp of how these components look in a real application a photograph and a schematic diagram are shown in Figure 3-11.

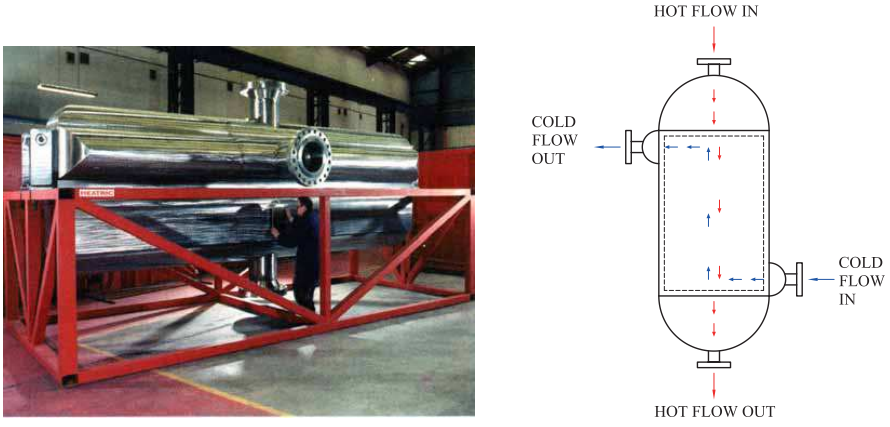

(a) PCHE final product [3] **(b)** PCHE schematic diagram

Figure 3-11: Printed Circuit Heat Exchanger photograph and diagram.

3-2 Dry cooler

This section presents the development of the steady state model of the cooler and its correspondent dimensioning procedure. Several studies promote the use of water-CO_2 PCHE for this component [16, 23, 27]. However, the s-CO_2 regenerative and recompression Brayton

systems in this study have a compressor suction temperature of 31.25°C, which allows the use of dry coolers with air as the heat sink. This is important since s-CO_2 power plants can be placed in locations without water resources and besides dry coolers avoid water pollution, which makes this type of heat exchangers an attractive option for the cooler.

The geometry of the dry cooler selected for the present study corresponds to plain flat fins on a tube array. Such configuration is used mainly in refrigeration and whenever an air low pressure drop is required [54]. While staggered tube arrays are common, inline tube arrangements are barely used and required only where the air pressure drop is constrained to be extremely low. It is beneficial to reduce this pressure drop since it will decrease the fan power consumption. Thus, an inline tube arrangement could seem a good choice. However, the heat transfer coefficient of the inline arrangements may be as small as 60% of the staggered array value [64]. This would increase considerably the size of the condenser, which is preferable to avoid. A staggered tube arrangement with plain flat fins combines the benefits of a low air side pressure drop with a reasonable heat transfer coefficient. A schematic graph of such configuration is shown in Figure 3-12.

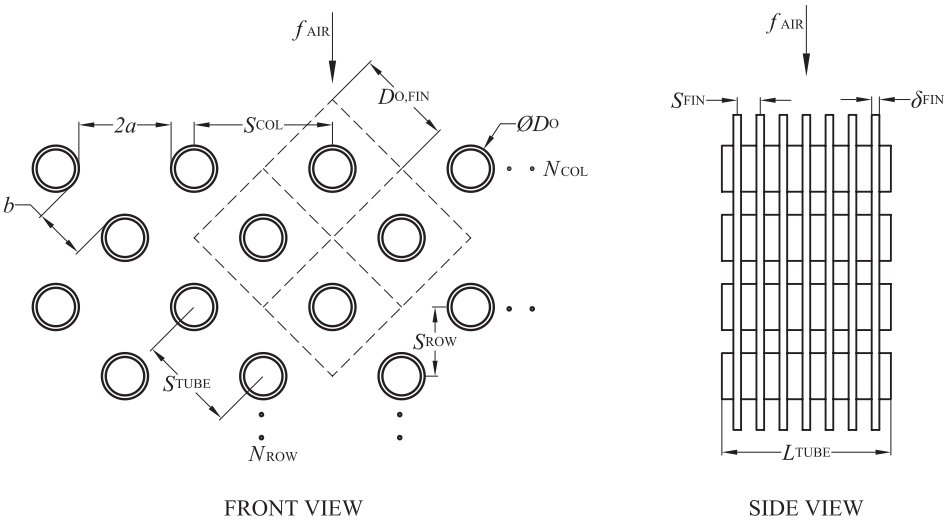

Figure 3-12: Cooler schematic diagram. Tube bundle front and side views.

3-2-1 Overall heat transfer coefficient

The overall heat transfer coefficient is a function of the resistances given by the tube side fluid, the tube wall, the fins and the air side,

$$U = \left(\frac{1}{\alpha_H} + \frac{D_I}{2\lambda_{TUBE}} \ln\left(\frac{D_O}{D_I}\right) + \frac{D_O}{2\lambda_{FIN}} \ln\left(\frac{D_{O,FIN}}{D_O}\right) + \frac{1}{\alpha_C \left(\frac{A_{FIN}}{A_I}\eta_{FIN} + \frac{A_{TUBE}}{A_I}\right)} \right)^{-1}, \tag{3-42}$$

where α_C and α_H correspond to the air and tube side heat transfer coefficients, λ_{FIN} and λ_{TUBE} stand for the thermal conductivities of the fins and tubes, and D_O and D_I are the external and internal tube diameters respectively. The external fin diameter, $D_{O,FIN}$, is a

function of the separation between tubes,

$$D_{\mathrm{O,FIN}} = \sqrt{(0.5 S_{\mathrm{COL}})^2 + S_{\mathrm{ROW}}^2}, \tag{3-43}$$

where S_{COL} and S_{ROW} are the transversal and longitudinal pitches respectively. The present study considers a rotated square staggered arrangement, which implies that the longitudinal pitch is half the transversal one. The area A_{FIN} corresponds to the fins, A_{I} to the internal surface of the tubes and A_{TUBE} to the external surface of the tubes without fins,

$$A_{\mathrm{FIN}} = N_{\mathrm{ROW}} N_{\mathrm{COL}} \frac{L_{\mathrm{TUBE}}}{S_{\mathrm{FIN}}} 2 \left(S_{\mathrm{ROW}} S_{\mathrm{COL}} - \frac{\pi D_{\mathrm{O}}}{4} \right), \tag{3-44}$$

$$A_{\mathrm{I}} = \pi D_{\mathrm{I}} L_{\mathrm{TUBE}} N_{\mathrm{ROW}} N_{\mathrm{COL}}, \tag{3-45}$$

$$A_{\mathrm{TUBE}} = \pi D_{\mathrm{O}} \left(L_{\mathrm{TUBE}} - \frac{L_{\mathrm{TUBE}}}{S_{\mathrm{FIN}} \delta_{\mathrm{FIN}}} \right) N_{\mathrm{ROW}} N_{\mathrm{COL}}. \tag{3-46}$$

The fin efficiency, η_{FIN}, for a straight fin with constant conduction cross section is

$$\eta_{\mathrm{FIN}} = \frac{\tanh(m L_{\mathrm{FIN}})}{m L_{\mathrm{FIN}}}, \tag{3-47}$$

where m is defined as

$$m = \left(\frac{2\alpha_{\mathrm{C}}}{\lambda_{\mathrm{FIN}} \delta_{\mathrm{FIN}}} \right). \tag{3-48}$$

The equivalent fin height, L_{FIN}, is

$$L_{\mathrm{FIN}} = 0.5 \sqrt{2 \frac{S_{\mathrm{COL}} S_{\mathrm{ROW}}}{\pi} S - D_{\mathrm{O}}} \left[1 + 0.35 \ln \left(\frac{2\sqrt{\frac{S_{\mathrm{COL}} S_{\mathrm{ROW}}}{\pi}}}{D_{\mathrm{O}}} \right) \right]. \tag{3-49}$$

The air side heat transfer coefficient is calculated as

$$\alpha_{\mathrm{C}} = \frac{Nu \lambda_{\mathrm{C}}}{D_{\mathrm{HD}}}, \tag{3-50}$$

where λ_{C} stands for the air thermal conductivity. The hydraulic diameter, D_{HD}, is function of the geometry of the heat exchanger,

$$D_{\mathrm{HD}} = \frac{4(S_{\mathrm{COL}} - D_{\mathrm{O}})(S_{\mathrm{FIN}} - \delta_{\mathrm{FIN}})}{2(S_{\mathrm{COL}} - D_{\mathrm{O}}) + 2(S_{\mathrm{FIN}} - \delta_{\mathrm{FIN}})}. \tag{3-51}$$

The calculation of the Nusselt number for the air side is done with the procedures of two different authors, as explained in the next section.

Air side heat transfer coefficient

Two expressions are used to calculate the air side heat transfer coefficient. The first one, given by Ferreira [7], calculates the Nusselt number as a function of the Reynolds and Prandtl numbers,

$$Nu = 0.167 Re^{0.63} Pr^{0.33}. \tag{3-52}$$

By definition the Reynolds number reads

$$Re = \frac{GD_{\text{HD}}}{\mu}. \tag{3-53}$$

The mass flux for the air side is function of the geometry and the air mass flow,

$$G = \frac{f}{(S_{\text{COL}} - D_{\text{O}})(S_{\text{FIN}} - \delta_{\text{FIN}})N_{\text{COL}}\frac{L_{\text{FIN}}}{S_{\text{FIN}}}}. \tag{3-54}$$

The second procedure to calculate the Nu is given by Wang and Chi [8] and recommended by Sha [54]. It deals with the calculation of the Colburn factor j,

$$j = \begin{cases} 0.108Re_{\text{CL}}^{-0.29}\left(\frac{S_{\text{COL}}}{S_{\text{ROW}}}\right)^{C_1}\left(\frac{S_{\text{FIN}}}{D_{\text{CL}}}\right)^{-1.084}\left(\frac{S_{\text{FIN}}}{D'_{\text{HD}}}\right)^{-0.786}\left(\frac{S_{\text{FIN}}}{S_{\text{COL}}}\right)^{C_2} & \text{for } N_{\text{ROW}} = 1, \\ 0.086Re_{\text{CL}}^{C_3}N_{\text{ROW}}\left(\frac{S_{\text{FIN}}}{D_{\text{CL}}}\right)^{C_5}\left(\frac{S_{\text{FIN}}}{D'_{\text{HD}}}\right)^{C_6}\left(\frac{S_{\text{FIN}}}{S_{\text{COL}}}\right)^{-0.93} & \text{for } N_{\text{ROW}} \geq 2, \end{cases} \tag{3-55}$$

where

$$C_1 = 1.9 - 0.23\ln\left(Re_{\text{CL}}\right), \tag{3-56}$$

$$C_2 = -0.236 + 0.126\ln\left(Re_{\text{CL}}\right), \tag{3-57}$$

$$C_3 = -0.361 - \frac{0.042N_{\text{ROW}}}{\ln\left(Re_{\text{CL}}\right)} + 0.158\ln\left[N_{\text{ROW}}\left(\frac{S_{\text{FIN}}}{D_{\text{CL}}}\right)^{0.41}\right], \tag{3-58}$$

$$C_4 = -1.224 - \frac{0.076\left(\frac{S_{\text{ROW}}}{D'_{\text{HD}}}\right)^{1.42}}{\ln\left(Re_{\text{CL}}\right)}, \tag{3-59}$$

$$C_5 = -0.083 + \frac{0.058N_{\text{ROW}}}{\ln\left(Re_{\text{CL}}\right)}, \tag{3-60}$$

$$C_6 = -5.735 + 1.21\ln\left(\frac{Re_{\text{CL}}}{N_{\text{ROW}}}\right). \tag{3-61}$$

$$\tag{3-62}$$

The Reynolds number Re_{CL} is based on the collar diameter $D_{\text{CL}} = D_{\text{O}} + 2\delta_{\text{FIN}}$,

$$Re_{\text{CL}} = \frac{\rho v_{\text{MIN}} D_{\text{CL}}}{\mu}, \tag{3-63}$$

where ρ corresponds to the density of the air and the velocity v_{MIN} is that correspondent to the minimum free flow area, A_{MIN}. In staggered arrays, the minimum free flow area can be located either at the plane perpendicular to the air mass flow (with dimension $2a$ in Figure 3-12), or at the plane aligned with the tube pitch (with dimension b in Figure 3-12). In order to calculate this area, Sha [54] calculates the variables a and b for each case,

$$2a = (S_{\text{COL}} - D_{\text{O}}) - (S_{\text{COL}} - D_{\text{O}})\frac{\delta_{\text{FIN}}}{S_{\text{FIN}}}, \tag{3-64}$$

$$b = (S_{\text{TUBE}} - D_{\text{O}}) - (S_{\text{COL}} - D_{\text{O}})\frac{\delta_{\text{FIN}}}{S_{\text{FIN}}}, \tag{3-65}$$

where S_{TUBE} is the tube pitch, as shown in Figure 3-12. The chosen variable will be the smallest one, which will produce the minimum flow area,

$$c = \begin{cases} 2a & \text{if } 2a < ab. \\ \\ 2b & \text{if } 2b < 2a. \end{cases} \tag{3-66}$$

Finally, the minimum free flow area can be calculated,

$$A_{\text{MIN}} = \left[\left(\frac{N_{\text{COL}}}{2} - 1\right) c + (S_{\text{COL}} - D_{\text{O}}) - (S_{\text{COL}} - D_{\text{O}})\frac{\delta_{\text{FIN}}}{S_{\text{FIN}}}\right] L_{\text{TUBE}}. \tag{3-67}$$

The hydraulic diameter in the expression of Wang, D'_{HD}, has a different formulation,

$$D'_{\text{HD}} = \frac{4 A_{\text{MIN}} S_{\text{ROW}} N_{\text{ROW}}}{A_{\text{FIN}} + A_{\text{TUBE}}}. \tag{3-68}$$

Tube side heat transfer coefficient

The hot (tube) side Nusselt number is calculated by means of the Gnielinski correlation, which is analyzed in Section 3-1-3.

3-2-2 Pressure drop

Two expressions are used to calculate the air side friction factor and pressure drop. The first is given by Ferreira [7] for the Darcy friction factor,

$$\Delta P_{\text{LS}} = \frac{F_{\text{DR}}}{2} \rho \left(\frac{G}{\rho}\right)^2, \tag{3-69}$$

$$F_{\text{DR}} = \begin{cases} 100 Re^{-0.82} \left(\frac{L}{D_{\text{HD}}}\right)^{0.7} & \text{for } Re < 1500 \\ \\ 0.7 Re^{-0.14} \left(\frac{L}{D_{\text{HD}}}\right)^{0.7} & \text{for } Re \geq 1500 \end{cases} \tag{3-70}$$

The second expression given by Wang [8] is used to calculate the Fanning friction factor,

$$F_{\text{FA}} = 0.0267 Re_{\text{L}}^{C_7} \left(\frac{S_{\text{COL}}}{S_{\text{ROW}}}\right)^{C_8} \left(\frac{S_{\text{FIN}}}{D_{\text{CL}}}\right)^{C_9}, \tag{3-71}$$

where

$$C_7 = -0.764 + 0.739 \left(\frac{S_{\text{COL}}}{S_{\text{ROW}}}\right) + 0.177 \left(\frac{S_{\text{FIN}}}{D_{\text{CL}}}\right) - \frac{0.00758}{N_{\text{ROW}}}, \tag{3-72}$$

$$C_8 = -15.689 + \frac{64.021}{\ln(Re_{\text{CL}})}, \tag{3-73}$$

$$C_9 = 1.696 - \frac{15.695}{\ln(Re_{\text{L}})}. \tag{3-74}$$

The Fanning friction factor in equation (3-71) is used in a special correlation that relates the friction factor and pressure drop for external finned geometries [64],

$$F_{\mathrm{FA}} = \frac{\Delta P_{\mathrm{LS}} D'_{\mathrm{HD}}}{2 N_{\mathrm{ROW}} G'^2}, \tag{3-75}$$

where G' is the mass flux based on the minimum free flow area.

The procedures given by Ferreira and Wang to calculate the heat transfer coefficient and pressure drop are tested on several several geometries, whose overall parameters are presented in Table 3-5.

Table 3-5: Geometries tested for air side correlations from Ferreira [7] and Wang [8].

		Equations (3-52),(3-70) [7]	Equations (3-55), (3-71) [8]
Ext. diameter	mm	$13.15 < D_{\mathrm{O}} < 22.10$	$6.35 < D_{\mathrm{O}} < 12.7$
Fin thickness	mm	$0.20 < \delta_{\mathrm{FIN}} < 0.35$	—
Fin pitch	mm	$2.20 < S_{\mathrm{FIN}} < 12.50$	$1.19 < S_{\mathrm{FIN}} < 8.7$
Longitudinal tube pitch	mm	$30.00 < S_{\mathrm{COL}} < 71.00$	$12.4 < S_{\mathrm{COL}} < 27.5$
Transversal tube pitch	mm	$30.00 < S_{\mathrm{ROW}} < 71.00$	$17.7 < S_{\mathrm{COL}} < 31.75$
N. of rows		$2 < N_{\mathrm{ROW}} < 6$	$1 < N_{\mathrm{ROW}} < 6$
N. of columns		$10 < N_{\mathrm{COL}} < 14$	—

Fan power consumption

The fan power consumption is an important factor since it affects the overall efficiency of the system. It is a function of the air mass flow rate, the pressure raise needed to overcome the losses in the cooler, the type of fan and the type of driving system [65],

$$\dot{W}_{\mathrm{FN}} = \frac{\dot{V} \Delta P}{\eta_{\mathrm{FA}} \eta_{\mathrm{DV}} \eta_{\mathrm{MT}}}, \tag{3-76}$$

where $\dot{V}$ is the fan volume flow rate, ΔP the pressure raise and η_{FN}, η_{DR}, η_{MT} the efficiencies of the fan, the driving system and the motor respectively.

The overall efficiency of axial fans have values between 45% and 85% [66] depending on the type of equipment. The largest value in this range is used in this study.

3-2-3 Material and geometrical characteristics

The pipe wall thickness is calculated according to the procedure provided by the ASME Process Piping Specification, ASME 31.3 [67]. Firstly, it is needed to obtain the "pressure design wall thickness",

$$t = \frac{P_{\mathrm{I}} D_{\mathrm{O}}}{2 \sigma_{\mathrm{AW}} K}, \tag{3-77}$$

where P_{I} is the internal design pressure, σ_{AW} is the allowable stress in tension, and K is the quality factor. All these characteristics depend on the pipe material and the manufacturing process. The minimum required thickness reads

$$t_{\mathrm{MIN}} = t + C, \tag{3-78}$$

where C stands for the mechanical, corrosion and erosions allowances. This value is set to 0 in this study.

The corrosion rates of carbon steel with s-CO_2 are up to 10 times higher than the rates for austenitic stainless steel [68] and therefore the latter is chosen as the tubing material. The allowable stress for stainless steel is 1379 bar at 100°C. The quality factor K is taken as 0.85, which is correspondent to an electric fusion welded pipe. It is possible to calculate the wall thickness as a function of the internal pressure and the tube outside diameter, as shown in Figure 3-13.

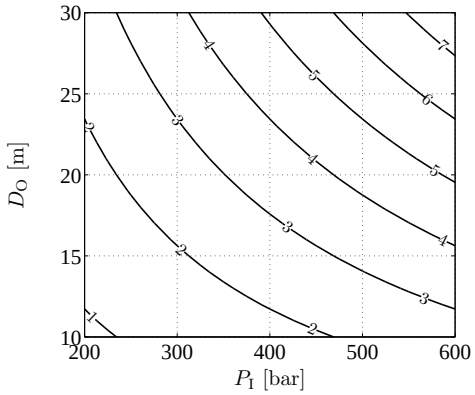

Figure 3-13: Cooler pipe minimum thickness as a function of the internal pressure and the pipe outside diameter [mm].

It is necessary to fix the geometry of the cooler to perform the dimensioning calculations. This geometry is chosen with the intention of fulfilling the recommendations indicated in Table 3-5, which regard the usage of the correlations for the pressure drop and the heat transfer coefficient. The dimensions are chosen as small as possible since this is beneficial for the overall heat transfer coefficient [8]. The result of these considerations is presented in Table 3-6.

Table 3-6: Cooler geometrical parameters and materials selected for the design procedure of the dry cooler

Geometrical parameters			
Tube external diameter	D_O	m	0.012
Pipe wall thickness	δ_{TUBE}	m	0.001
Tube horizontal pitch	S_{COL}	m	0.030
Tube vertical pitch	S_{ROW}	m	0.015
Fin pitch	S_{FIN}	m	0.002
Fin thickness	δ_{FIN}	m	0.0002
Materials			
Tube material	Stainless steel SS316		
Fin material	Aluminium 1060		

There are gaps between the ranges recommended by Ferreira and Wang presented in Table 3-5. For example, the minimum pipe outer diameter used by Ferreira is 13.5 mm, while the maximum diameter used by Wang is 12.7. Consequently, there are geometrical dimensions in Table 3-6 that do not comply with one of the mentioned ranges. This should be considered

when applying this procedure in future works. The properties of the materials used in this study are presented in Table 3-7.

Table 3-7: Cooler material properties

Material		SS 316 (tubes)	Al 1060 (fins)
Density	kg/m^3	7990.00 [55]	2698.79 [69]
Thermal conductivity	W/m^{2}K	16.20 [55]	234.37 [69]
Roughness	mm	0.045 [70]	—

3-2-4 Calculation procedure

The calculation of the dimensions of the cooler is performed by means of the discretization of the pipes in the bundle. A schematic diagram of this procedure is shown in Figure 3-14. While this particular case has 8 rows with 4 passes, further analysis consider additional

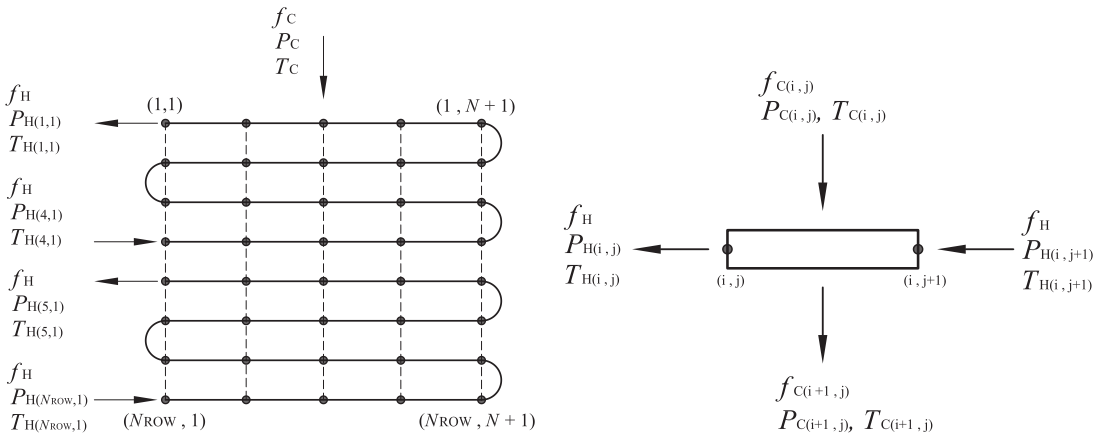

(a) Cooler discretization. **(b)** Single control volume.

Figure 3-14: Discretization of the pipes and single control volume in the dry cooler.

layout configurations. The thermodynamic states of both cold (air) and hot (CO_2) sides can be gathered as a matrix, as shown in Figure 3-14a. The free body diagram of a single element with two nodes is shown in Figure 3-14b. The information regarding the leaving CO_2 properties in the cooler are known from the thermodynamic analysis. The inlet air properties correspond to environmental conditions, which are taken as 15°C and 1 bar in this study. It is possible therefore to obtain the overall heat transfer coefficient with the correlations described previously and additionally it is possible to establish the energy balance for the first element, which has the index (1,1) in Figure 3-14. There are several assumptions considered in this analysis,

- the CO_2 mass flow rate is distributed equally in all the tubes,
- the properties at the beginning of the element are representative for the entire section,
- heat transfer in the direction of the flow is neglected,
- the air properties are considered constant and equal to those under environmental conditions.

The energy transferred between hot and cold sides is calculated with the overall heat transfer coefficient,

$$\dot{Q}_{(\mathrm{i,\,j})} = U_{(\mathrm{i,\,j})} A_{(\mathrm{i,\,j})} (T_{\mathrm{H(i,\,j)}} - T_{\mathrm{C(i,\,j)}}), \tag{3-79}$$

where $A_{(\mathrm{i,\,j})}$ stands for the heat transfer area,

$$A_{(\mathrm{i,\,j})} = \frac{L_{\mathrm{TUBE}}}{N_{\mathrm{CV}}}, \tag{3-80}$$

where N_{CV} stands for the number of elements or control volumes per tube. The specific thermal energy for the hot side is calculated with the CO_2 mass flow in each tube,

$$q_{\mathrm{H(i,\,j)}} = \frac{\dot{Q}_{(\mathrm{i,\,j})}}{f_{\mathrm{H}}}, \tag{3-81}$$

where f_{H} is the tube mass flow. The enthalpy leaving the current control volume for the CO_2 is calculated with the enthalpy at the first node and the specific thermal energy,

$$h_{\mathrm{H(i,\,j+1)}} = h_{\mathrm{H(i,\,j)}} + q_{\mathrm{H(i,\,j)}}. \tag{3-82}$$

The CO_2 pressure drop is calculated with the procedure used in the straight channels of the regenerators in Section 3-1-4. Once the pressure loss is obtained, the pressure of the CO_2 leaving the current control volume is obtained,

$$P_{\mathrm{H(i,\,j+1)}} = P_{\mathrm{H(i,\,j)}} + \Delta P_{\mathrm{H(i,\,j)}}. \tag{3-83}$$

Finally, the hot side temperature in the subsequent element can be obtained as a function of the pressure and the enthalpy,

$$T_{\mathrm{H(i,\,j+1)}} = T(P_{\mathrm{H(i,\,j+1)}}, h_{\mathrm{H(i,\,j+1)}}), \tag{3-84}$$

The air temperature in the next air node can be calculated from the energy balance in the element,

$$T_{\mathrm{C(i+1,\,j)}} = T_{\mathrm{C(i,\,j)}} + \frac{\dot{Q}_{\mathrm{C(i,\,j)}}}{f_{\mathrm{C(i,\,j)}} C_{\mathrm{P,C}}}. \tag{3-85}$$

The heat capacity is considered constant and its value is calculated as a function of the properties at the inlet of the first element,

$$C_{\mathrm{P,C}} = C_{\mathrm{P}} \left(P_{\mathrm{C(1,1)}}, T_{\mathrm{C(1,1)}} \right). \tag{3-86}$$

The air side pressure drop is not considered in the discretization procedure. It is calculated for the entire air mass flow by means of the friction factors given by equations (3-70) and (3-71).

Number of tubes

As shown later, the number of passes, rows and the tube length are inputs used in the optimization procedure. The calculation of the number of tubes is based on the average

properties of the fluid and the mentioned inputs. The friction pressure loss associated with the Darcy-Weisbach friction factor, equation (3-20), reads,

$$\Delta P_{\mathrm{FR}} = F_{\mathrm{DR}} \frac{L_{\mathrm{GR}}}{D} \frac{\rho v^2}{2},$$

where L_{GR} is the length correspondent to one group of tubes joined by the passes,

$$L_{\mathrm{GR}} = L_{\mathrm{TUBE}} N_{\mathrm{PASS}}. \tag{3-87}$$

The velocity of the fluid in the pipe, v, is a function of the mass flow in one pipe, the internal section area and the density,

$$v = \frac{f_{\mathrm{H}}}{A\rho}. \tag{3-88}$$

The tube mass flow f_{H} is a function of the total mass flow, the number tubes and the number of passes,

$$f_{\mathrm{H}} = \frac{f_{\mathrm{TOT}} N_{\mathrm{PASS}}}{N_{\mathrm{TUBE}}}. \tag{3-89}$$

Combining the last three expressions it is possible to obtain the number of tubes as a function of the number of passes and tube length,

$$N_{\mathrm{TUBE}} = \frac{f_{\mathrm{TOT}} N_{\mathrm{PASS}}}{A} \sqrt{\frac{L_{\mathrm{TUBE}} N_{\mathrm{PASS}} \bar{F}_{\mathrm{DR}}}{2 \Delta P_{\mathrm{LS}} \bar{\rho}}}. \tag{3-90}$$

Recall that the pressure loss ΔP_{FR} is caused by friction effects. It is calculated with the total pressure loss and the local losses at the inlet and outlet of the tubes,

$$\Delta P_{\mathrm{FR}} = \Delta P_{\mathrm{CO}} - \Delta P_{\mathrm{LC}}, \tag{3-91}$$

where ΔP_{LC} corresponds to the contraction and expansion losses calculated with expression (3-18). The total pressure drop in the cooler, ΔP_{CO}, is obtained from the thermodynamic analysis and the procedure explained in Section 3-1-5.

The bar over the density in equation (3-90) indicates that it is an average property, obtained with the inlet and outlet pressures and temperatures given by the thermodynamic analysis. The friction factor, $\bar{F}_{\mathrm{DR}}$, is calculated with a different expression,

$$\bar{F}_{\mathrm{DR}} = 1.25(F_{\mathrm{HE}} + F_{\mathrm{HL}}), \tag{3-92}$$

where F_{HE} and F_{HL} are the Darcy friction coefficients at the inlet and outlet of the pipes, which can be calculated with the procedure for the straight channels in the regenerators model of Section (3-1-4). Notice that equation (3-90) is an implicit expression and it requires an iterative procedure to be solved since the number of tubes is necessary to calculate the friction factors in equation (3-92), and the friction factors are needed to obtain N_{TUBE}.

Iterative procedure

Two additional iteration procedures are required to dimension the cooler according to the operating conditions given by the thermodynamic analysis. The first regards the hot side

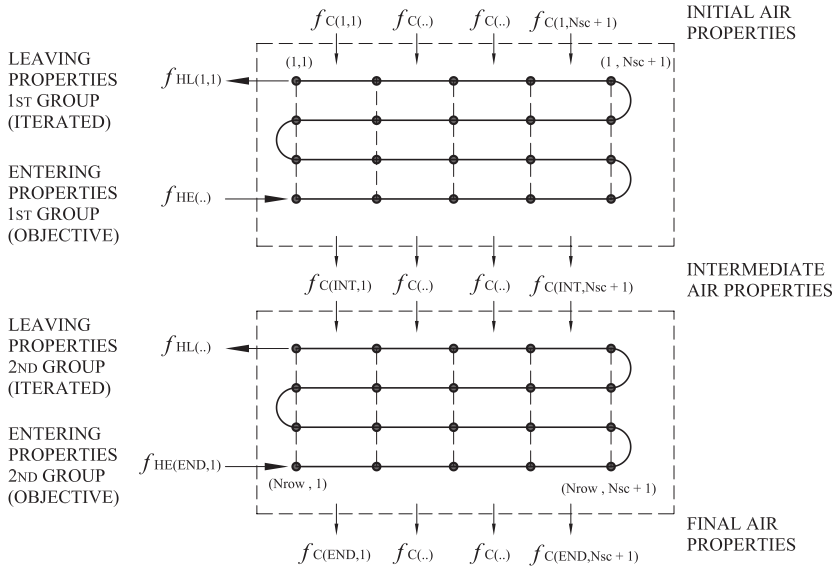

Figure 3-15: Cooler division in groups used for the iterative procedure.

properties. Notice that if the leaving properties of the CO_2 are considered inputs to the system, the inlet properties are a consequence of the calculation procedure explained earlier. The outlet properties will be the same in each tube, while the inlet properties will be different since each pass experiences different effects with the air at different temperatures. This approach is not correct since in real heat exchangers the inlet properties are the same in each tube, while the outlet states are different. In order to solve this problem, an iterative procedure is adopted. To perform this calculation the pipes are divided in groups according to the number of passes, as shown in Figure 3-15. With separate groups, it is possible to iterate the exit properties of each group, until the desired inlet state is reached. Once this is done, the properties of the air after the group (intermediate air properties in Figure 3-15) are sent to the next group, and the procedure is repeated for the next case until all the groups are covered.

The leaving properties of the CO_2 in the tubes are now different depending on each group. Further calculations require a unique outlet temperature and pressure in order match them with the required operating conditions. The outlet pressure is calculated as the arithmetic average of the pressures leaving each group,

$$\bar{P}_{\mathrm{HL}} = \frac{P_{\mathrm{HL(i)}} + ... + P_{\mathrm{HL}(N)}}{N}, \tag{3-93}$$

where $P_{\mathrm{HL(i)}}$ is the exit pressure of a single group and N is the number of groups. In order to calculate the leaving temperature it is necessary to obtain the average enthalpy,

$$\bar{h}_{\mathrm{HL}} = \frac{h_{\mathrm{HL(i)}} + ... + h_{\mathrm{HL}(N)}}{N}. \tag{3-94}$$

Finally, the leaving average temperature is a function of the average pressure and enthalpy,

$$\bar{T}_{\mathrm{HL}} = T(\bar{P}_{\mathrm{HL}}, \bar{h}_{\mathrm{HL}}). \tag{3-95}$$

For a given air mass flow, the iteration explained in the previous paragraphs gives a leaving CO_2 temperature calculated with equation (3-95). This temperature should match compressor suction temperature of the thermodynamic analysis shown in Table 2-2. The second iteration procedure consists on varying the air mass flow until this requirement is fulfilled. A schematic diagram of the two iterations is shown in Figure 3-16.

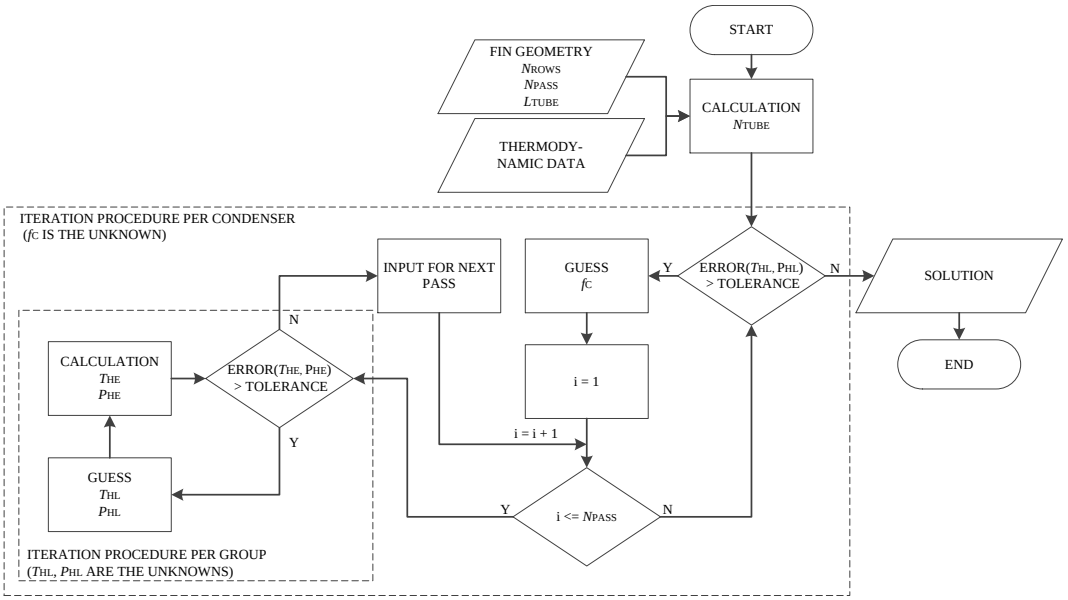

Figure 3-16: Flow diagram of the iterative procedure for dimensioning of the cooler.

3-2-5 Correlations validation

The validation of the correlations for the heat transfer coefficient and the pressure drop described in Sections 3-2-1 and 3-2-2 is done comparing the design of a heat exchanger based on these correlations and the design done with the commercial code ASPEN Exchanger Design & Rating [5]. The characteristics of this heat exchanger are presented in Table 3-8.

Table 3-8: Operating conditions for the validation of the steady state cooler model

CO_2 mass flow	f_{H}	kg/s	119.89
CO_2 inlet temperature	T_{HE}	°C	95.67
CO_2 outlet temperature	T_{HL}	°C	31.25
CO_2 max. pressure drop	ΔP_{H}	bar	0.5
CO_2 operating pressure	ΔP_{HE}	bar	50
Air mass flow	f_{C}	kg/s	calculated
Air inlet temperature	T_{CE}	°C	15
Air outlet temperature	T_{CL}	°C	50
Air pressure drop	Δ_{PH}	bar	calculated

The material and geometrical characteristics of the cooler have been already introduced in Table 3-6. The operating conditions of the cycle are those of the vapor recompression

system presented in Figure 2-23, corresponding to the minimum TIT for a pressure loss of 2%. However, the inlet pressure of CO_2 is set to 50 bar and not to the value close to the critical pressure since the calculation procedure of ASPEN produces high deviations in the energy balance when working in this region. Both ASPEN and the present study consider similar calculation procedures since they divide the pipes in a specific number of sections and evalueate each section as an independent control volume. The number of elements for every single pipe has been set as 12. The results of the design are shown in Table 3-9.

Table 3-9: Results of dimensioning calculations performed with ASPEN and the correlations for the dry cooler

		ASPEN	**Ferreira**	**Wang et.al.**
Tube side				
Inlet temperature	°C	113.08	113.08	113.08
Outlet temperature	°C	31.57	31.24	31.24
Inlet pressure	bar	50.00	50.00	50.00
Outlet pressure	bar	49.84	49.90	49.93
Pressure drop	bar	0.16	0.10	0.07
Tube length	m	9.85	7.78	5.01
Air side				
Mass flow	kg/s	346.51	346.51	346.51
Inlet temperature	°C	15.00	15.00	15.00
Outlet temperature	°C	49.99	50.17	50.20
Pressure drop	Pa	47.00	66.62	171.29
Heat transfer coefficient	W/m^2K	—	77.19	326.70
Fan power consumption	kW	21.56	22.17	56.99
Tubes and passes				
Number of tubes	—	4992	4992	4992
Number of rows	—	8	8	8
Number of passes	—	1	1	1
Other				
Bundle mass	tonne	19.89	15.26	9.82

Both the correlations of Ferreira and Wang predict a lower tube length when compared with the one of ASPEN. However, Ferreira's procedure gives a better result since the length of the tubes is closer to the one in the design done by ASPEN. The reason is the larger air side heat transfer coefficient given by the Wang correlations, leading to a lower tube length. As mentioned by these authors [8], their correlations are developed for smaller geometries, i.e., smaller tube diameter and pitch. This effect increases the air side heat transfer coefficient improving the performance of the heat exchanger and reducing its size. A schematic diagram of the cooler taken from ASPEN is presented in Figure 3-17. The only difference with the design developed in this work is the length of the tubes.

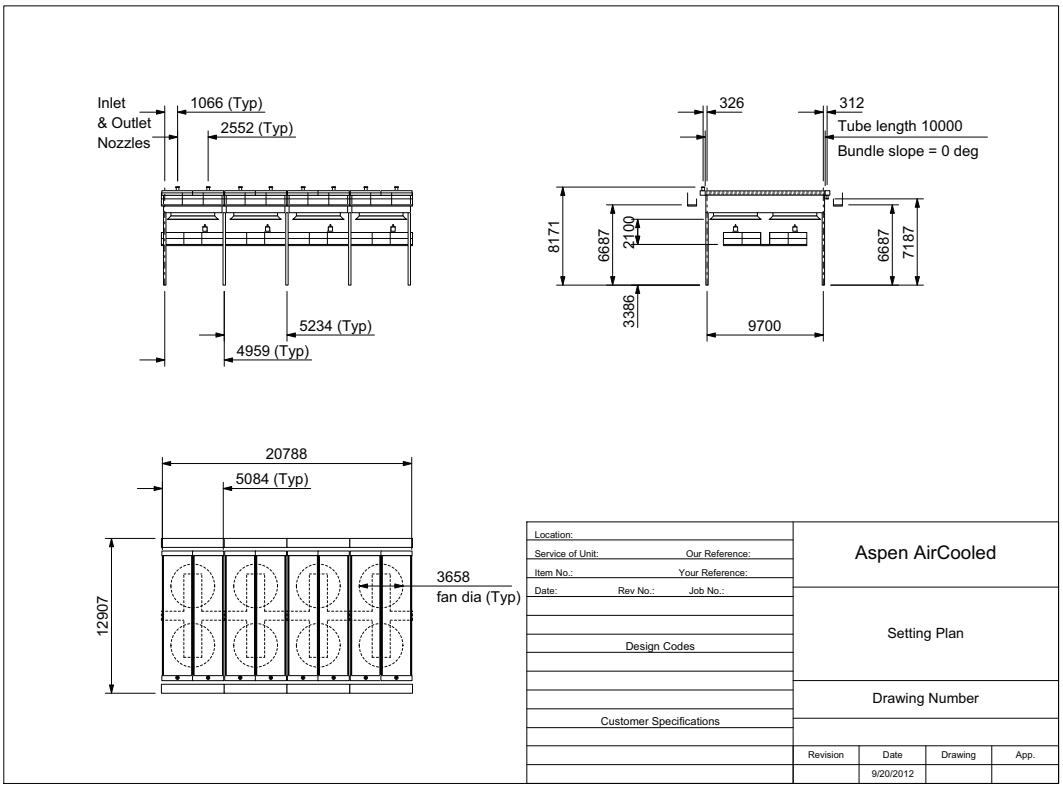

Figure 3-17: Cooler diagram correspondent to the validation procedure (taken from ASPEN [5]). All the dimensions in mm.

3-2-6 Optimization procedure

Once the finned geometry is fixed, it is possible to analyze different combinations of rows, passes and tube lengths to obtain the most beneficial configuration in terms of energy and material consumption. The constraints of the geometry are shown in Table 3-10. Using the calculation procedure explained earlier, it is possible to obtain several solutions that meet the required operating conditions and it is possible then to select the best configuration. An example is developed with the operating conditions of the recompression Brayton system described in Figure 2-21. The results are presented in Figure 3-18.

Table 3-10: Cooler optimization constraints

Number of rows	—	4,6,8
Number of passes	—	1,2,4,6,8
Tube length	m	2 - 10
Fan power	MW	< 20
Pinch	°C	> 5

The fan power consumption is shown in Figure 3-18a. Notice how for the same number of rows and passes, larger tube lengths present lower fan power. This trend is present since larger dimensions increase the flow area of the air side and reduce the Reynolds number and the pressure loss. This effect has a cost, the weight of the cooler increases considerably with lower fan power, as shown in Figure 3-18b. Not all the geometries present solutions due to

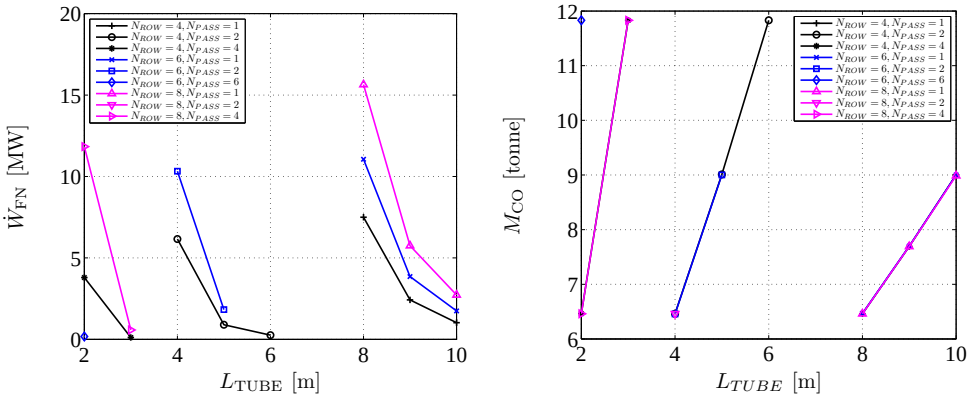

(a) Fan power. **(b)** Weight.

Figure 3-18: Fan power and bundle weight of the solutions for the cooler geometry as a function of the tube length, number of passes and rows. The design optimization is performed for the recompression Brayton system described in Figure 2-21.

the constraints in Table 3-10 which exclude the solutions with pinch temperatures lower than 5°C, for example. The analysis in this work takes the cooler configuration with the lowest power consumption as the optimal. The information about this heat exchanger chosen from the solutions in Figure 2-21 is presented in Figure 3-19.

Characteristic		Value
Number or tubes	—	10040
Number or columns	—	2510
Number or rows	—	4
Number of passes	—	4
Tube length	m	3
Pinch	°C	8.42
Fan power	kW	114.23
Weight	tonne	11.83
Pressure drop	bar	0.30

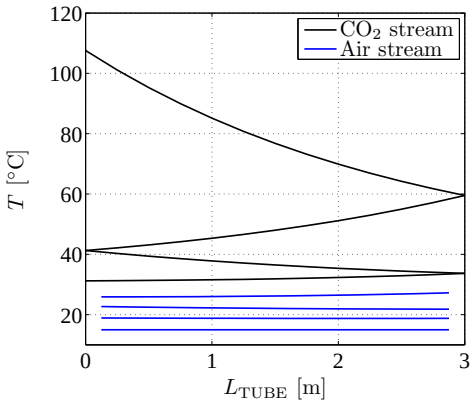

Figure 3-19: Characteristics of the cooler optimal geometry and its correspondent temperature profile for the recompression Brayton system described in Figure 2-21.

Notice how the slope of the CO_2 temperature is larger when the stream is far from the critical point. Once the CO_2 approaches the critical temperature, the slope decreases until the last pipe, in which the temperature of the CO_2 remains almost constant due to the increment in the specific heat capacity. The pinch temperature is 8.42°C, which is slightly higher than the imposed limit of 5°C. Therefore, the geometry of the cooler can be further modified in next projects until the minimum temperature approach is reached. The pressure drop from the thermodynamic analysis is 0.26 bar, and the design presents a value of 0.30 bar, which is reasonably close and proves the validity of the procedure to calculate the number of tubes related with equation (3-92).

3-2-7 Cooler dimensioning

Following a similar procedure to that developed for the regenerator, two parameters are used in the thermodynamic analysis to obtain the operating conditions of the cooler, which are used in the dimensioning calculations. The parameters are the system pressure drop and the compressor discharge pressure. Each set of operating conditions gives several solutions according to the optimization procedure explained in the last section. The configurations with the lowest fan power consumption are finally chosen. The results are presented in Table 3-11 and Table 3-12 for the regenerative and the recompression Brayton systems respectively.

Table 3-11: Cooler optimum solutions for the regenerative Brayton system as a function of the system pressure loss and compressor discharge pressure ($\eta_{TH} = 50\%$, $T_2 = 31.25°C$, $P_2 = 74$ bar, $\eta_{TR} = 93.4\%$, $\eta_{CM} = 85\%$, $\eta_{HR} = 90\%$, $\Delta T_{PN} = 10°C$)

P_3 (bar)	$\Delta P_{\mathbf{LS}}$ (%)	$N_{\mathbf{TUBE}}$	$N_{\mathbf{ROW}}$	N_{PASS}	L_{TUBE} (m)	$\dot{W}_{FN}$ (kW)	Weight (tonne)
200	2.0	4132	4	2	5	284.20	8.11
	6.0	12520	8	8	2	103.52	9.84
	10.0	2548	4	2	8	176.15	8.00
400	2.0	2772	4	2	7	135.14	7.62
	6.0	5526	6	6	3	111.80	6.51
	10.0	1532	4	2	10	201.69	6.02
600	2.0	2164	4	2	7	244.35	5.95
	6.0	4284	6	6	3	181.15	5.05
	10.0	2360	4	4	5	156.23	4.63

Table 3-12: Cooler optimum solutions for the recompression Brayton system as a function of the system pressure loss and compressor discharge pressure ($\eta_{TH} = 50\%$, $T_2 = 31.25°C$, $P_2 = 74$ bar, $\eta_{TR} = 93.4\%$, $\eta_{CM} = 85\%$, $\eta_{HR} = 90\%$, $\Delta T_{PN} = 10°C$)

P_3 (bar)	$\Delta P_{\mathbf{LS}}$ (%)	$N_{\mathbf{TUBE}}$	$N_{\mathbf{ROW}}$	N_{PASS}	L_{TUBE} (m)	$\dot{W}_{FN}$ (kW)	Weight (tonne)
200	2.0	21204	6	6	2	105.07	16.66
	6.0	5044	4	2	8	121.78	15.85
	10.0	4476	4	2	9	110.40	15.82
400	2.0	3832	4	2	7	166.13	10.54
	6.0	7830	6	6	3	129.42	9.23
	10.0	6342	6	6	3	275.70	7.47
600	2.0	2844	4	2	7	278.93	7.82
	6.0	6112	4	4	5	649.94	6.77
	10.0	3632	4	4	4	327.11	5.71

Computational cost

The calculation procedure described in this optimization procedure deals with the dimensioning of the dry cooler based on a discretization performed in the tubes of this component. The iterative procedure shown in Figure 3-16 requires long computational time mainly due to the calculation of the leaving close-to-critical properties of CO_2. Due to this fact the computational fluid library [45] performs large quantities of iterations to solve the equations of state delaying the search for optimum solutions in the cooler. For example, in order to obtain the cooler geometries presented in Tables 3-11 and 3-11, the computational code requires approx-

imately 9 hours, which means that each optimal solution requires 30 minutes. Future works should consider the optimization of the code improving the initial conditions of the solver, or replacing the equations of state by polynomials or look up tables.

Chapter 4

Integrated system design

This chapter is devoted to the application of the simultaneous thermodynamic analysis and components design to three specific applications. The first study case analyzes the possibility of using the s-CO_2 Brayton system for aerospace propulsion. The second deals with the application to solar power generation and the third consists in the statement of an optimization procedure.

4-1 Aircraft propulsion systems

Since the first aerospace applications of gas turbines and propellers at the beginning of the last century, the aircraft propulsion technology for commercial purposes has evolved until the turbofan engine, which is nowadays widely used in most of the modern airliners. Large improvements have been obtained through the years by means of efficient engine designs and materials, advanced fuel injection and combustion systems, etc. However, the worldwide energy usage and emissions trends make necessary to take a step further and think of new, innovative propulsion systems.

The current aircrafts generate the needed thrust by means of air breathing engines (gas turbines with open cycles) and open propellers, with overall maximum efficiencies of about 45% [9]. The s-CO_2 closed Brayton system can be a good alternative since it presents not only potential larger efficiencies, but also the advantage of smaller turbomachinery. In order to set an appropiate frame to analyze the potentialities of the s-CO_2 system, it is necessary to choose a reference aircraft engine. The characteristics of such device will be used for the design of the supercritical system.

4-1-1 Reference Engine: Rolls - Royce Trent 1000

The state-of-the-art turbofan Rolls-Royce Trent 1000-A1, used on the Boeing 787-8 aircraft, is the chosen as the reference engine since it is one of the best available technologies. The specifications of this propulsion system are shown in Table 4-1.

Table 4-1: Specifications of the Rolls-Royce Trent 1000 engine and airliner Boeing 787

Rolls-Royce Trent 1000 [51]		
Dry weight	kg	5409.0
Fan air mass flow	kg/s	1089.0 - 1211.0
Rotational speed	RPM	13500.0 (high pressure turbine)
Thrust* (ISA)	kN	283.6 (take off, S/L), 65.4
Specific fuel consumption (ISA)	mg/Ns	13.787 (take off), 14.325 (cruise)
By pass ratio	—	10.4 - 11.0 (take off), 10.7 (cruise)
Overall pressure ratio	—	47.7 (take off), 50.0 (climb)
Boeing 787 [71]		
Cruise speed	m/s	$0.85M$
Take off speed [72]	m/s	84.89
Maximum certified altitude	m	13135.0
Number of engines	—	2
Other information		
Fuel lower heating value [9]	kJ/kg	42800.0

* Cruise conditions, 10670 m, Trent 900, at $0.85M$

In order to establish a common frame for the comparison between the s-CO_2 Brayton system and the Trent engine, it is necessary to study the thermodynamic behavior of the latter. It is possible then to set specific targets for the s-CO_2 system based on the results of this analysis, which is the objective of the next sections.

Turbofan overall performance

The turbofan overall efficiency is the product of the thermal and propulsive efficiencies,

$$\eta_{\mathrm{OV}} = \eta_{\mathrm{TH}}\eta_{\mathrm{PR}}, \tag{4-1}$$

where η_{TH} stands for the thermal efficiency and η_{PR} for the propulsive efficiency. The thermal efficiency is the standard efficiency of a gas power cycle, which indicates the quantity of energy that is transformed into useful power in the engine,

$$\eta_{\mathrm{TH}} = \frac{\dot{W}_{\mathrm{PR}}}{f_{\mathrm{FL}} LHV_{\mathrm{FL}}}, \tag{4-2}$$

where f_{FL} is the fuel mass flow and LHV_{FL} the correspondent lower heating value. $\dot{W}_{\mathrm{PR}}$ stands for the propulsion power generated by the engine, which is not completely transformed into thrust. Consequently, a second indicator, the propulsive efficiency, is necessary to quantify the quality of the transformation of the engine power into the actual thrust,

$$\eta_{\mathrm{PR}} = \frac{\dot{W}_{\mathrm{TT}}}{\dot{W}_{\mathrm{PR}}}. \tag{4-3}$$

Where $\dot{W}_{\mathrm{TT}}$ is the thrust power, that is the power that actually moves the aircraft,

$$\dot{W}_{\mathrm{TT}} = F_{\mathrm{TT}} v_0, \tag{4-4}$$

where v_0 and F_{TT} correspond to the aircraft velocity and the engine thrust respectively. The turbofan engine generates the propulsive power by means of the core and the fan,

$$\dot{W}_{\mathrm{PR}} = \dot{W}_{\mathrm{PR,CR}} + \dot{W}_{\mathrm{PR,FN}}, \tag{4-5}$$

where $\dot{W}_{\mathrm{PR,CR}}$ and $\dot{W}_{\mathrm{PR,FN}}$ correspond to the contributions of the core and the fan respectively. In order to estimate the propulsive and thermal efficiency, it is necessary to obtain these contributions. Consider Figure 4-1, which shows a scheme of a turbofan engine with the correspondent station numbering. The uninstalled thrust of the core side can be calculated

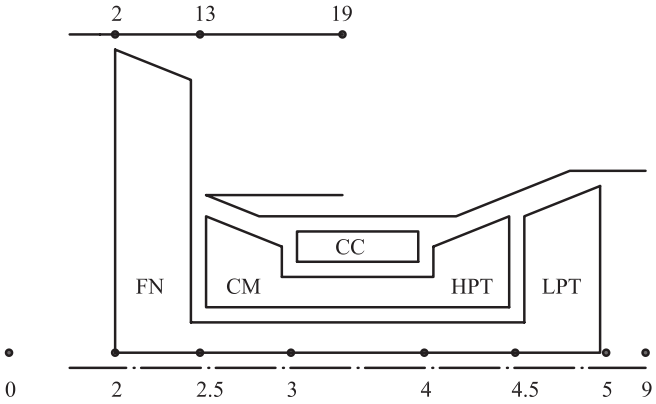

Figure 4-1: Turbofan schematic diagram.

as the momentum balance in this component without the drag effects due to the inlet and nozzle surfaces,

$$F_{\mathrm{CR}} = f_9 v_9 - f_{\mathrm{CR}} v_0 + (P_9 - P_0) A_9. \tag{4-6}$$

The air mass flow entering the core is f_{CR}, while f_9 corresponds to the mass flow leaving the core with a velocity v_9 and pressure P_9. It is desirable to expand the exhaust gas to the ambient pressure [9]. In this case, $P_9 = P_0$ and expression (4-6) reduces to

$$F_{\mathrm{CR}} = f_9 v_9 - f_{\mathrm{CR}} v_0. \tag{4-7}$$

The propulsion power generated by the engine is a function of the mass flow rates and their correspondent velocities,

$$\dot{W}_{\mathrm{PR,CR}} = \frac{1}{2}\left(f_9 v_9^2 - f_{\mathrm{CR}} v_0^2\right). \tag{4-8}$$

Equations (4-7) and (4-8) can be used for the fan analysis as well. The air mass flow through the core side is calculated with the bypass ratio and the fan mass flow,

$$f_{\mathrm{CR}} = \frac{f_{\mathrm{FN}}}{B+1}, \tag{4-9}$$

which gives a core mass flow of 93.08 kg/s. The fuel mass flow is calculated using the thrust specific fuel consumption and the thrust from Table 4-1, which gives a value of $f_{\mathrm{FL}} = 0.94$ kg/s. The cruise velocity is calculated with the correspondent speed of sound at cruise altitude (10670 m),

$$v_0 = M_0 a_0. \tag{4-10}$$

Considering that core produces about 20% of the total thrust in this engines [73], the core nozzle velocity can be calculated with expression (4-7). Finally, the core propulsive power in equation (4-8) can be calculated replacing the core exhaust mass flow (f_9) with the sum of the air mass flow (f_{CR}) and the fuel mass flow (f_{FL}). A similar procedure is followed for the fan analysis. The results of both procedures and the engine efficiencies are presented in Table 4-2.

Table 4-2: Calculated Rolls-Royce Trent 1000 performance parameters

Parameter		Core side	Fan side
Thrust	N	13080	52320
Nozzle velocity	kg/s	388.69	304.61
Propulsion power	kW	4144.70	14562.79
Air mass flow	kg/s	93.08	995.92
Thrust power	kW	16485.38	
Propulsive power	kW	18707.49	
Fuel mass flow	kg/s	0.94	
Fuel energy input	kW	40097.39	
Thermal efficiency	%	46.66	
Propulsive efficiency	%	88.12	
Overall efficiency	%	41.11	

The high thermal efficiency is achieved by the large difference between the maximum and minimum temperatures of the cycle. The environmental temperatures at cruise conditions can be as low as -50°C, while the TIT in the Trent 1000 engine can reach 1500 °C [74]. This difference leads to higher Carnot and thermal efficiencies. The large propulsive efficiency is produced by the high bypass ratio of this engine. To understand this, consider the combination of expressions (4-4), (4-7) and (4-8),

$$\eta_{\mathrm{PR}} = \frac{\left(f_9 v_9 - f_{\mathrm{CR}} v_0\right) v_0}{\frac{1}{2}\left(f_9 v_9^2 - f_{\mathrm{CR}} v_0^2\right)}. \tag{4-11}$$

This is valid for a jet engine with a single inlet and outlet. If the fuel mass flow is small compared to the air mass flow, the last expression can be reformulated,

$$\eta_{\mathrm{PR}} = \frac{2}{\frac{v_9}{v_0} + 1}. \tag{4-12}$$

Figure 4-2 shows the relation between the propulsive efficiency and the velocity ratio according to this expression. It can be seen that the lower the velocity of the jet, the higher the efficiency.

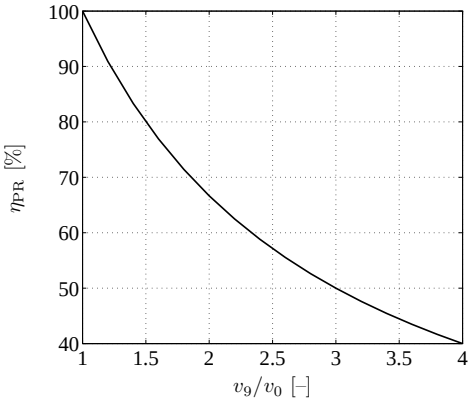

Figure 4-2: Ideal propulsive efficiency as a function of the velocity ratio.

Turbojet engines large velocity ratios, with low propulsive efficiency. On the other hand, the turbofan engines have a lower velocity ratio in their fan side (with large fan mass flow rates), with higher propulsive efficiencies. This is why the turbofans with high bypass ratio are able to improve their overall efficiency.

Parameters for the thermodynamic analysis

The turbofan has an internal Brayton cycle system responsible to generate the propulsive power in both the core and fan sides. It is convenient to analyze this system and obtain the thermodynamic states in each stage of the engine. There are several adopted assumptions,

- no transmission losses,
- ideal diffuser and nozzles,
- no pressure losses in combustion chamber,
- fuel mass flow neglected,
- the properties of air are considered valid for the working fluid during the entire cycle.

The figures of merit of the turbine and compressor (or fan) are the polytropic efficiencies, defined as

$$e_{\mathrm{TR}} = \frac{\text{Actual turbine work for a differential pressure change}}{\text{Ideal turbine work for a differential change}}, \tag{4-13}$$

$$e_{\mathrm{CM}} = \frac{\text{Ideal compressor work for a differential pressure change}}{\text{Actual compressor work for a differential pressure change}}, \tag{4-14}$$

$$\tag{4-15}$$

for the turbine and the compressor respectively. It can be demonstrated that the isentropic efficiency of both components is function of the polytropic efficiency for an ideal gas,

$$\eta_{\mathrm{TR}} = \frac{1 - \Pi_{\mathrm{TR}}^{\frac{\gamma-1}{\gamma} e_{\mathrm{TR}}}}{1 - \Pi_{\mathrm{TR}}^{\frac{\gamma-1}{\gamma}}}, \tag{4-16}$$

$$\eta_{\mathrm{CM}} = \frac{\Pi_{\mathrm{CM}}^{\frac{\gamma-1}{\gamma}} - 1}{\Pi_{\mathrm{CM}}^{\frac{\gamma-1}{\gamma} e_{\mathrm{CM}}} - 1}, \tag{4-17}$$

for the turbine and the compressor respectively. The total pressure ratio Π corresponds to the ratio of the total or stagnation pressures in both components,

$$\Pi = \frac{\text{Total pressure leaving the component}}{\text{Total pressure entering the component}}. \tag{4-18}$$

Expressions (4-16) and (4-17) are used to obtain the isentropic efficiencies of the turbine and compressor respectively. Similarly, the combustion efficiency is defined as

$$\eta_{\mathrm{CC}} = \frac{\text{Energy transfered to the cycle}}{\text{Energy from the fuel}}. \tag{4-19}$$

The values of the figures of merit for the compressor, turbine and combustion chamber are presented in Table 4-3 and correspond, according to Mattingly [9], to a level of technology 4, i.e., engines produced since the year 2005.

As mentioned in Table 4-1, the cruise thrust rating is done at 10670 m and the air properties have to be corrected for these conditions. The air properties are calculated according to the International Standard Atmosphere (ISA) models. The temperature decreases with a constant gradient,

$$\kappa = -6.5 \cdot 10^{-3}\,\mathrm{K/m}. \tag{4-20}$$

Table 4-3: Components figures of merit for aircraft turbine engines with level of technology 4 (produced since the year 2005) [9]

Component	Figure of merit	Value
Compressor	e_{CM}	0.90
Fan	e_{FN}	0.89
Turbine (cooled)	e_{TR}	0.90
Combustion chamber	η_{CC}	0.999

This relation valid until 11000 m. The temperature of the air at an altitude H is

$$T_H = T_{\mathrm{REF}} + \kappa H, \tag{4-21}$$

where T_{REF} is the reference value of 288 K at 0 m. The pressure is calculated as

$$P_H = P_0 \left(\frac{T_0 + \kappa H}{T_0} \right)^{-\frac{g}{R\kappa}}, \tag{4-22}$$

where P_0 stands for the reference pressure, with a value of 101325 Pa, R is the air gas constant, 287 $\mathrm{m}^2/(\mathrm{s}^2\mathrm{K})$, and g is the gravity constant, 9.8 m^2/s. Once the pressure and temperature are calculated, the rest of the properties are obtained by means of the computational fluid library used so far.

Fan side analysis

The thermodynamic analysis of the turbofan is done in two steps (fan side and core side). This section deals with the fan side, whose T-s diagram is shown in Figure 4-3. Recall that

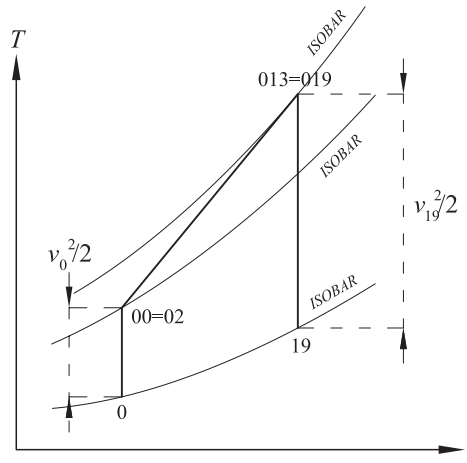

Figure 4-3: Schematic T-s diagram of the fan side of a turbofan engine.

the numbering corresponds to the stations indicated in Figure 4-1. Since the diffuser is taken as ideal, the total enthalpy and pressure at the inlet of the engine (00) are the same at the inlet of the compressor (02). Likewise, the nozzle is also considered to be ideal and the total enthalpy and pressure at the outlet of the fan (013) are the same at the outlet of the nozzle (019). It is assumed that the nozzle expands the air to the environmental pressure, i.e., $P_{19} = P_0$. Although the pressure ratio of the fan is an unknown, both the velocities at the

inlet and outlet of the fan are known from the calculations in Section 4-1-1. This information is enough to reveal the thermodynamics of the fan. The first equation used to do so is related to the fan pressure ratio,

$$\Pi_{\mathrm{FN}} = \frac{P_{019}}{P_{02}}. \tag{4-23}$$

The isentropic efficiency of the fan is a function of the polytropic efficiency and the pressure ratio,

$$\eta_{\mathrm{FN}} = \frac{\Pi_{\mathrm{FN}}^{\frac{\gamma-1}{\gamma}} - 1}{\Pi_{\mathrm{FN}}^{\frac{\gamma-1}{\gamma} e_{\mathrm{FN}}} - 1}. \tag{4-24}$$

The total enthalpy leaving the fan is a function of the pressure ratio, the entering enthalpy and the isentropic efficiency,

$$h_{019} = h\left(\Pi_{\mathrm{FN}}, h_{02}, \eta_{\mathrm{FN}}\right). \tag{4-25}$$

The entropy leaving the fan, s_{019}, is obtained with its correspondent total pressure and enthalpy and it is used to obtain the enthalpy at point (19),

$$h_{19} = h\left(P_{19}, s_{019}\right), \tag{4-26}$$

where P_{19} equals the environmental pressure. The velocity of the air leaving the fan is a function of the stagnation enthalpy at (019) and the enthalpy at (19),

$$v_{19} = \sqrt{2(h_{019} - h_{19})}. \tag{4-27}$$

The cruise velocity v_{19} is known from previous calculations. Thus, it is necessary to iterate on the value of the total pressure P_{019} until the required cruise velocity is matched. The fan propulsive power is the difference between the kinetic energy entering and leaving this system,

$$\dot{W}_{\mathrm{PR,FN}} = f_{\mathrm{FN}}\left(\frac{v_{19}^2}{2} - \frac{v_0^2}{2}\right) = f_{\mathrm{FN}}\left[(h_{013} - h_{19}) - (h_{02} - h_0)\right]. \tag{4-28}$$

The shaft power used to drive the fan is function of the leaving and entering total enthalpies,

$$\dot{W}_{2-13} = f_{\mathrm{FN}}\left(h_{013} - h_{02}\right). \tag{4-29}$$

The T-s diagram for the fan and the related information is presented in Figure 4-3.

Core side analysis

A general T-s diagram of the process in the core is shown in Figure 4-5. The assumptions considered for the fan are valid for the core side as well. The total enthalpy at the inlet of the engine (00) equals the one entering the compressor (02), and the total enthalpy leaving the turbine (05) equals the one leaving the nozzle (09). The pressure at the outlet of the core side (9) equals the environmental pressure (0) since it is assumed that the expansion is done until environmental conditions. The thermodynamic states can be found with the available information from the cycle and using a similar procedure to the one used for the fan. The enthalpy leaving the high pressure compressor is a function of the entering enthalpy and the pressure ratio,

$$h_{03} = h\left(\eta_{\mathrm{CM}}, h_{02}\right). \tag{4-30}$$

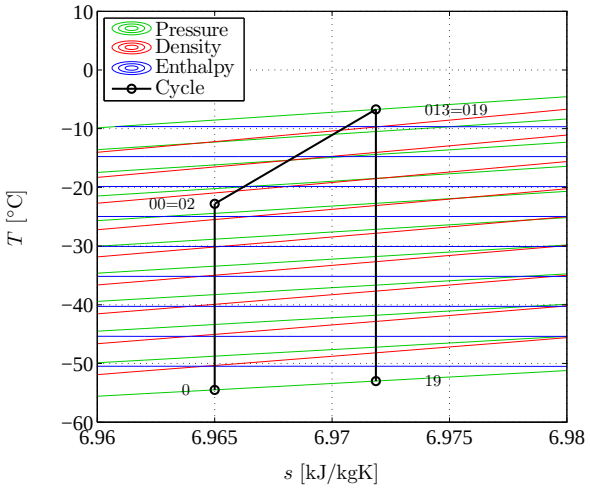

Cycle points	P [bar]	T [°C]	h [kJ/kg]
Environm. cond. (0)	0.24	-54.50	218.79
Fan inlet (02)	0.38	-22.80	250.56
Fan outlet (013)	0.46	-6.72	266.69
Nozzle outlet (19)	0.24	-53.00	220.29
Shaft power [kW]	16063.54		
Isent. efficiency	0.89		
Pressure ratio	1.21		

Figure 4-4: Fan T-s diagram of the Turbofan Trent 1000 engine.

The energy entering the cycle is taken from the fuel energy input reported in Table 4-2. Consequently, the enthalpy at the inlet of the turbine, h_{04}, can be obtained from the energy balance on the combustion chamber,

$$h_{04} = h_{03} + \frac{f_{\text{FL}} LHV_{\text{FL}} \eta_{\text{CC}}}{f_{\text{CR}}}. \tag{4-31}$$

The enthalpy of the air leaving the turbine can be calculated from the internal energy balance in the system. Both the fan and the compressor are driven by the high and low pressure turbines,

$$\dot{W}_{2-13} + \dot{W}_{2-3} = \dot{W}_{4-5}, \tag{4-32}$$

where $\dot{W}_{2-13}$ corresponds to the shaft power of the fan, calculated in the fan analysis and shown in Figure 4-4. Likewise, $\dot{W}_{2-3}$ stands for the power of the compression process from the inlet of the fan to the outlet of the compressor, while $\dot{W}_{4-5}$ is the power of the high pressure

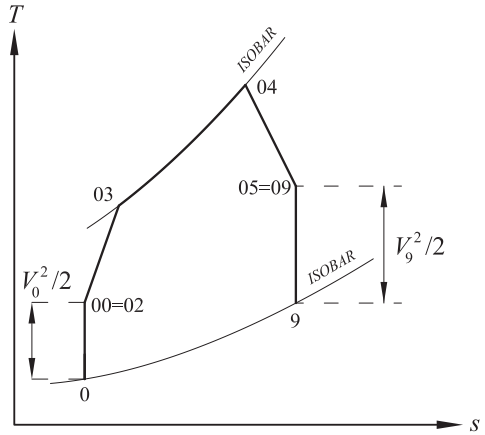

Figure 4-5: Schematic T-s diagram of the core side of a turbofan engine.

and low pressure turbines. The leaving total enthalpy is obtained working equation (4-32),

$$h_{09} = h_{04} - \frac{\dot{W}_{2-13}}{f_{\text{CR}}} - \frac{\dot{W}_{2-3}}{f_{\text{CR}}}. \tag{4-33}$$

The entropy leaving the core, s_{09}, is obtained with its correspondent total pressure and enthalpy and it is used to obtain the enthalpy at point (9),

$$h_9 = h\left(P_9, s_{09}\right), \tag{4-34}$$

where P_9 equals the environmental pressure. The velocity of the air leaving the core is again a function of the stagnation enthalpy at (09) and the enthalpy at (9),

$$v_9 = \sqrt{2(h_{09} - h_9)}. \tag{4-35}$$

The core velocity is shown in Table 4-2 and it is necessary to iterate the value of the total pressure P_{09} until the core velocity matches this value. The information of the core side analysis is shown in Figure 4-6. The propulsive power of the engine core is the difference of

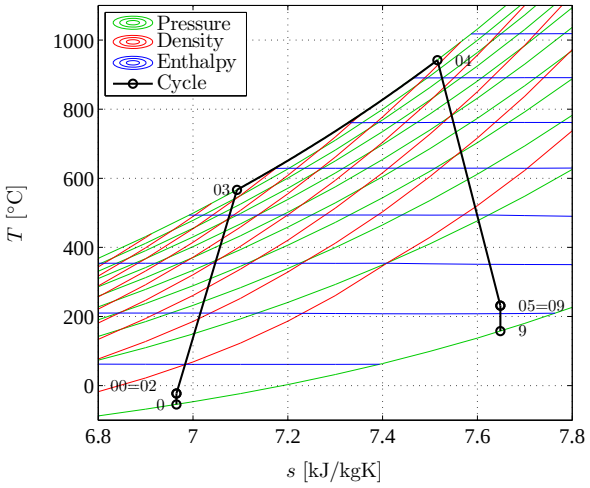

Cycle points	P [bar]	T [°C]	h [kJ/kg]
Environm. cond. (0)	0.24	-54.50	218.79
Fan inlet (02)	0.38	-22.80	250.56
Cm. outlet (03)	19.12	566.60	867.15
Tr. inlet (04)	19.12	941.90	1297.51
Tr. outlet (09)	0.42	231.56	508.34
Nozzle outlet (9)	0.24	157.79	432.80
Trb. power (gross) [kW]	73453.51		
Comp. power [kW]	57389.97		
Turb. Is. efficiency	0.94		
Comp. Is. efficiency	0.84		
Turb. pressure ratio	0.022		

Figure 4-6: Core T-s diagram of the Turbofan Trent 1000 engine.

the kinetic energy of the air mass flow through the core and it can be calculated as a function of the total enthalpies in the system,

$$\dot{W}_{\text{PR,CR}} = f_{\text{CR}}\left(\frac{v_9^2}{2} - \frac{v_0^2}{2}\right) = f_{\text{FN}}[(h_{05} - h_9) - (h_{02} - h_0)]. \tag{4-36}$$

The turbine shaft power driving the compressor and the fan reads

$$\dot{W}_{4\text{-}5} = f_{\text{CR}}\left(h_{04} - h_{05}\right). \tag{4-37}$$

Finally, the power of the compressor is

$$\dot{W}_{2\text{-}3} = f_{\text{CR}}\left(h_{03} - h_{02}\right). \tag{4-38}$$

In order to verify the validity of the calculations, the overall energy balance is stated and calculated. The control volume is shown in Figure 4-7.

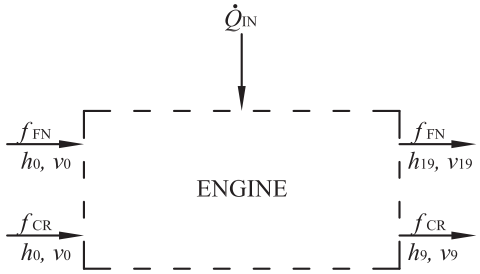

Figure 4-7: Turbofan overall control volume.

The shaft work generated in the cycle is used internally to drive the fan and the compressors. Consequently, the power generated in the engine is associated with changes in the kinetic energy and the enthalpy in the mass flow rates. The energy balance reads,

$$(f_{FN} + f_{CR}) \left(h_0 + \frac{v_0^2}{2} \right) + f_{FL} LHV_{FL} \eta_{CC} = f_{FN} h_{019} + f_{CR} h_{09}. \tag{4-39}$$

The right side of expression (4-39) is expressed as a function of the total enthalpies in order to use the values shown in Figures 4-4 and 4-6. The result of both sides of this equation is 312 MW, which shows that the energy balance is correct.

Thermal efficiency and power of the supercritical cycle

The power that is finally moving the aircraft is the thrust power. It was shown in Section 4-1-1 that, for the Boeing 787, it has a value of

$$\dot{W}_{TT} = 16.5 \text{ MW}.$$

Once the thrust power is fixed, it is the propulsive efficiency the one that determines the power that must be generated by the cycle,

$$\dot{W}_{PR} = \frac{\dot{W}_{TT}}{\eta_{PR}}.$$

The turbofan, an open cycle, generates the propulsive power, $\dot{W}_{PR}$, accelerating the air in both the core and the fan side. A closed cycle like that of the s-CO_2 systems, generates shaft power which can be converted to produce thrust by means of another component like an open propeller.

As calculated before, the overall efficiency of the Trent 1000 engine is about 41%. It is necessary to achieve an overall efficiency larger than the mentioned value in order to prove that the s-CO_2 system can overcome the performance rates of this engine. Once the propulsive efficiency is known, the thermal efficiency and the shaft power of the cycle can be calculated with expressions (4-1) and (4-3). This thermal efficiency is the minimum value that should be

obtained from the s-CO_2 cycle in order to decrease the energy consumption compared to the Trent 1000 engine. The propulsive efficiency is considered equal to that of the Trent engine, 88.12%, which gives the needed shaft work and thermal efficiency.

$$\dot{W}_{\mathrm{SH}} = 18.7\,\mathrm{MW},$$
$$\eta_{\mathrm{TH}} = 46.66\,\%.$$

The thermodynamic analysis of the s-CO_2 cycle aims to obtain the same power with a higher thermal efficiency, which is chosen as 50%.

4-1-2 Regenerator dimensioning

Chapter 3 deals with the dimensioning of the regenerators. Recall that the Trent 1000 engine was used as a reference for both the thermodynamic analysis and the components dimensioning. Consequently, the results obtained in section 3-1-7 can be used here. The weight of the regenerators is shown in Figure 4-8.

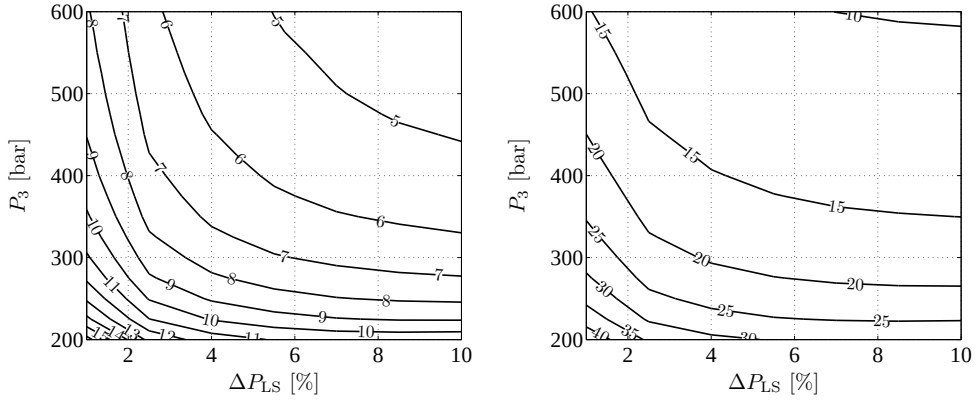

(a) Simple regenerative. **(b)** Vapor recompression.

Figure 4-8: Contour lines of the regenerators weight (tonne) as a function of the pressure drop and discharge pressure for the regenerative and vapor recompression Brayton systems ($\eta_{\mathrm{TH}} = 50\%$, $T_2 = 31.25°\mathrm{C}$, $P_2 = 74$ bar, $\eta_{\mathrm{TR}} = 93.4\%$, $\eta_{\mathrm{CM}} = 85\%$, $\eta_{\mathrm{HR}} = 90\%$, $\Delta T_{\mathrm{PN}} = 10°\mathrm{C}$).

The simple regenerative system presents the best characteristics, with weights that vary between 5 and 15 tonne. However, considering that the reference engine dry weight is 5.4 tons [51], it is clear that the s-CO_2 regenerative and recompression Brayton systems are not feasible for aerospace propulsion with the design procedures adopted until this point. The turbomachinery, the heater and the cooler will add more weight which will make the total system even heavier.

Anyway, because of the very high potential related to the use of s-CO_2 power systems in terms of efficiency and compactness, new design strategies for compact and light heat exchangers are worth being investigated to decrease more the weight of these components by means of different channel geometries or lighter heat exchanger materials. Additionally, future investigations should consider the design of the external heater, which has not been considered in this project and will bring additional complexity to the propulsion system.

4-2 Solar tower power plant

Nowadays, converting the solar energy into heat is the most common and well-developed solar conversion technology [75]. It is done by means of Concentrated Solar Power technologies (CSP). These systems transfer the thermal energy to a thermal power cycle for the generation of electricity. Two different configurations of CSP systems have been developed up to commercial scales, the parabolic through and the solar tower systems. While the first one has a working temperature between 150 and 350°C, the solar power works typically between 500 and 1000°C, depending on the primary heat transfer fluid and the type of power cycle [75]. The high pressure associated with s-CO_2 power cycles makes the application to parabolic through systems difficult. Previous studies lead to the conclusion that solar powers tower may be more suitable for this working fluid [31]. Although the high pressures are a challenge for the solar tower as well, there are modular options which are currently being studied in order to decrease the load and complexity per tower.

Solar tower systems consists in a complex of sun tracking mirrors (heliostats) which reflect the solar irradiation and concentrate it into a receiver. This last device is the one that converts irradiation into thermal energy. A schematic diagram of the whole system is presented in Figure 4-9.

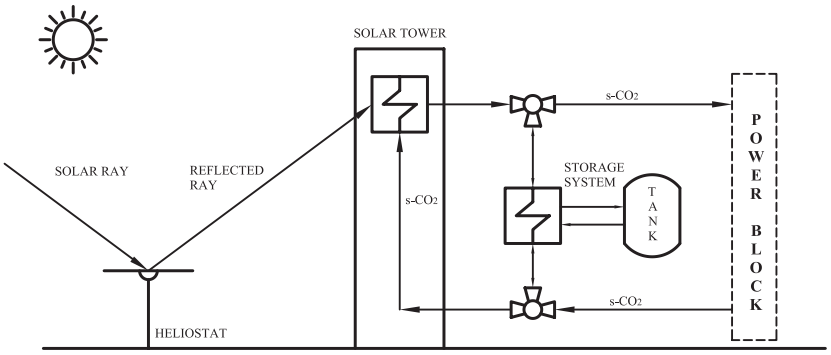

Figure 4-9: Solar tower power complex. The power block is composed by the turbomachinery and the heat exchangers.

The proposed design is based on the works of Turchi et al. [31]. The figure presents the connection between the solar tower and the power block, the last one constituted by the turbomachinery, the regenerators and the cooler. The s-CO_2 is used as both heat transfer and gas power fluid. The advantages of such design are simpler and compact machinery needed for s-CO_2 applications, with smaller weight and volume, that may lead to lower installation and maintenance costs.

Additional advantages are related to the properties of the s-CO_2 itself. Current CSP plants use oil, steam, or molten salts to transfer the energy to the power block. These fluids present several difficulties that could be overcome with s-CO_2. While the synthetic oil has an upper temperature limit of 400°C, the steam generation requires complex control and its storage capacity is limited. The molten salts can work until temperatures of 600°C and they have practically no vapor pressure. However, they freeze at 100°C, requiring complex freeze control systems [32]. The s-CO_2 Brayton cycle offers the advantages of single phase

operation. However, the main challenge is the high pressure of the fluid (higher than that used for superheated steam). As mentioned earlier, a possible solution is to design modular fields, each one with its own power block. This approach could reduce the size of the system with shorter piping, smaller machinery, lower losses and faster dynamics [31].

The receiver is the heat exchanger in which the concentrated solar irradiation is transformed into thermal energy. It can be classified into external and cavity designs. The most common external receivers (tubular receivers) consist of several panels with connected vertical tubes that form a cylinder. The tubes are made of special materials covered with coatings in order to have a close to black body behavior. In the cavity receivers the solar irradiation passes through an aperture before hitting the heat transfer surface. This type of receivers have acceptance angles between 60 and 120° [75]. The tubular receivers with conventional panels have been used with steam, sodium and molten salts for temperatures up to 500-600°C. The experience on this type of receivers with gas is scarce. However, temperatures up to 800-900°C are achievable [76]. Cylindrical external receivers are the most common choice for surrounding fields, which is the configuration taken in this study.

The main costs of a solar power system are distributed among the heliostat field, the power block and the tower (receiver), with a total share of 74% [77]. The largest contribution of 43% of the total cost is produced by the heliostat field, which is why the present study focuses on the dimensioning of this component.

4-2-1 Local field efficiency

The power transmitted to the receiver comprehends the contributions of each heliostat in the field. Thus, it is necessary to analyze the performance of these devices in order to establish a procedure to size the system according to the required power. The local heliostat field efficiency is the concept that helps measuring the performance of a single heliostat [10],

$$\eta_{\mathrm{HT}} = \cos(\omega) F_{\mathrm{SB}} F_{\mathrm{SP}} F_{\mathrm{AT}}, \tag{4-40}$$

where ω is the incidence angle, F_{SB} is the blocking factor, F_{SP} is the spillage factor, and F_{AT} is the attenuation factor.

Cosine efficiency

The cosine efficiency, $\cos(\omega)$, is related with the position of the sun, the heliostat and the receiver (see Figure 4-10). The heliostats have a sun tracking system with a normal vector

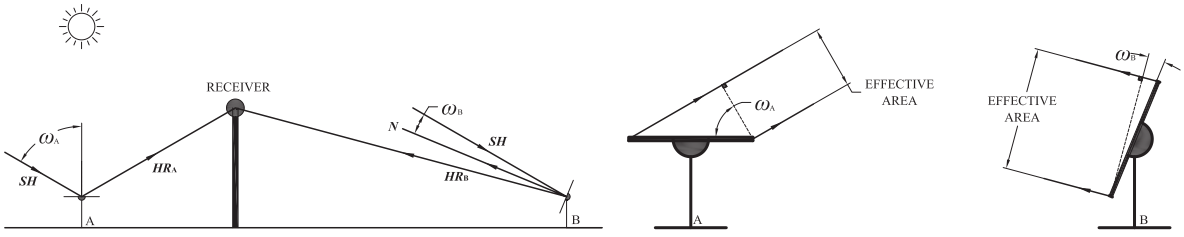

Figure 4-10: Tower, heliostat and sun ray relative positions.

($\boldsymbol{N}$) that bisects the angle between the vector formed by the sun and the heliostat center ($\boldsymbol{SH}$) and the vector formed by the heliostat center and the receiver ($\boldsymbol{HR}$). The incidence angle ω is the one between the normal of the surface and the other two vectors. Notice that the effective mirror area depends on this angle and corresponds to the area of the heliostat times the cosine of ω. The heliostat B has a surface located in the opposite side of the sun, which gives a lower incidence angle. On the other hand, the location of the heliostat A produces a higher incidence angle, reducing the effective area. This is why, for the solar power plants with a positive latitude (north hemisphere), the heliostats located at the north of the tower have a higher cosine efficiency and an better overall performance. The incidence angle can be obtained with the scalar product of the unit vectors of $\boldsymbol{SH}$ and $\boldsymbol{HR}$,

$$\omega = 0.5\cos^{-1}(-\boldsymbol{SH}_{\mathrm{U}} \cdot \boldsymbol{HR}_{\mathrm{U}}). \tag{4-41}$$

In order to obtain the solar ray unit vector it is necessary to set a reference system. Consider Figure 4-11, the unitary vector of the sun ray $\boldsymbol{SH}$ is a function of the position of

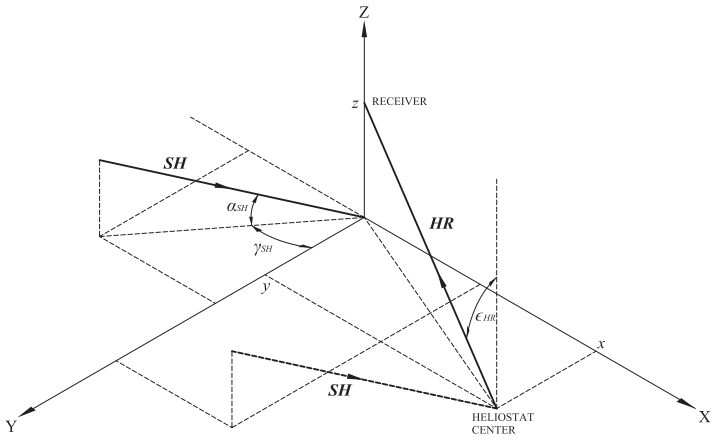

Figure 4-11: Heliostat field, coordinate system.

the sun, described by three angles, the solar hour angle ψ, the site latitude φ and the solar declination ϑ [78]. The solar hour angle is the angular displacement of the sun from a specific meridian due to the earth rotation. It is considered positive in the morning and negative in the afternoon, with each hour correspondent to 15°of displacement (all the angles in radians in the following equations),

$$\psi = (HOUR - 12)\frac{15\pi}{180}. \tag{4-42}$$

The solar declination corresponds to the angle between the equatorial line and a line joining the center of the earth and the center of the sun. It depends on the day of the year,

$$\vartheta = \frac{23.45\pi}{180}\sin\left(2\pi\frac{284 + DAY}{365}\right). \tag{4-43}$$

The variable DAY starts with 1 in January the 1$^{\mathrm{st}}$. The elevation of the solar ray is function of the mentioned angles,

$$\alpha_{SH} = \sin(\varphi)\sin(\vartheta) + \cos(\varphi)\cos(\vartheta)\cos(\psi). \tag{4-44}$$

It is possible now to calculate the solar ray azimuth angle,

$$\gamma_{SH} = \frac{\sin(\alpha_{SH})\sin(\varphi) - \sin(\vartheta)}{\cos(\alpha_{SH})\cos(\varphi)}. \tag{4-45}$$

The unit vector of the sun ray can be expressed with the elevation and azimuth angles,

$$\boldsymbol{SH}_{\mathrm{U}} = \left(\cos(\alpha_{SH})\sin(\gamma_{SH}), -\cos(\alpha_{SH})\cos(\gamma_{SH}), -\sin(\alpha_{SH})\right). \tag{4-46}$$

Considering the reference system in Figure 4-11, the unit vector joining the heliostat and the receiver is

$$\boldsymbol{HR}_{\mathrm{U}} = \left(\frac{-x}{\sqrt{x^2+y^2+z^2}}, \frac{-y}{\sqrt{x^2+y^2+z^2}}, \frac{z}{\sqrt{x^2+y^2+z^2}}\right). \tag{4-47}$$

Spillage factor

The spillage factor is the fraction of the energy sent from a heliostat that actually hits the receiver surface. It is calculated with the following expression for a reasonably well focused heliostat [6],

$$F_{\mathrm{SP}} = \frac{\mathrm{pH}\left(\frac{H_{\mathrm{RC}}}{2\sqrt{2}}\sigma_{\mathrm{RC}}, -a_{\mathrm{RC}}, a_{\mathrm{RC}}\right)\mathrm{pH}\left(\frac{L_{\mathrm{RC}}}{2\sqrt{2}}\sigma_{\mathrm{RC}}, -a_{\mathrm{RC}}, a_{\mathrm{RC}}\right)}{a_{\mathrm{RC}}^2}, \tag{4-48}$$

where L_{RC} corresponds to the height of the receiver and W_{RC} to the width (diameter) of the receiver. a_{HT} is a parameter function of the overall area of the heliostat,

$$a_{\mathrm{HT}} = \frac{\sqrt{A_{\mathrm{HT}}}}{2\sqrt{2}\sigma_{\mathrm{RC}}}, \tag{4-49}$$

where A_{HT} is the area of the heliostat and σ_{RC} is the dispersion of the effective sunshape on the receiver plane. For convenience expression (4-48) contains a function called pH,

$$\mathrm{pH}(\xi, -a, a) = \frac{1}{2}\left[(\xi+a)\mathrm{erf}(\xi+a) + \frac{1}{\sqrt{\pi}}e^{-(\xi+a)^2} - (\xi-a)\mathrm{erf}(\xi-a) - \frac{1}{\sqrt{\pi}}e^{-(\xi-a)^2}\right] + \mathrm{const}, \tag{4-50}$$

where erf(x) is the error function.

Attenuation factor

The attenuation factor is related to the losses produced by atmospheric factors and the distance between the heliostats and the receiver. For a clear day, considered in this study, the attenuation factor is [79]

$$F_{\mathrm{AT}} = 0.99326 - 0.1046|\boldsymbol{HR}| + 0.017|\boldsymbol{HR}|^2 - 0.002845|\boldsymbol{HR}|^3, \tag{4-51}$$

where $|\boldsymbol{HR}|$ corresponds to the scalar distance between the heliostat center and the receiver.

The staggered array

The blocking factor is associated with the area of the heliostat free of shadows and blockings. The shadowing is produced by neighbor heliostats interrupting the sun rays, while the blocking corresponds to the non shaded area of a heliostat that can not be seen from the receiver because of the presence of other heliostats. It is time dependent since it is related with the sun position. In order to minimize the blocking factor a staggered array is typically chosen for heliostat fields [6, 75, 79]. Such configuration is shown in Figure 4-12.

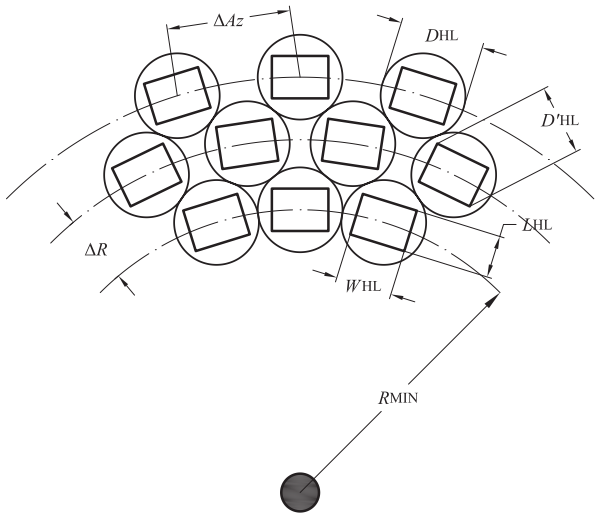

Figure 4-12: Heliostat staggered array (based on the works of Collado et. al. [6]).

The diagonal of the heliostats corresponds to D'_{HT}, while L_{HT} and W_{HT} are the height and the width of the heliostats respectively. The distance that separates each row is ΔR and the azimuthal separation between heliostats is ΔAz. The first row of the heliostats is located at a minimum radius R_{MIN}. Notice that the effective diameter of the heliostats is represented by D_{HT}, which is larger than the diagonal of these components, D'_{HT}. This is done in order to add a safety distance between the heliostats in the same row [6]. It can be shown that

$$D_{\mathrm{HT}} = \left(\sqrt{1 + wr^2} + r_{\mathrm{SD}}\right) L_{\mathrm{HT}}, \tag{4-52}$$

where wr corresponds to the height to width ratio of the heliostats and r_{SD} is the adimensional safety distance between heliostats in the same row,

$$r_{\mathrm{SD}} L_{\mathrm{HT}} = D_{\mathrm{HT}} - D'_{\mathrm{HT}}. \tag{4-53}$$

Blocking factor

Collado et al. [6] developed an analytical expression for the blocking factor based on geometrical relations between the heliostats. Consider Figure 4-13, which presents the relations between the heliostats A and B. The vectors $\boldsymbol{SH}$, $\boldsymbol{N}$ and $\boldsymbol{HR}$ correspond to the solar ray, the heliostat surface normal and the vector joining the heliostat and the receiver respectively (these vectors were already presented in Figure 4-11).

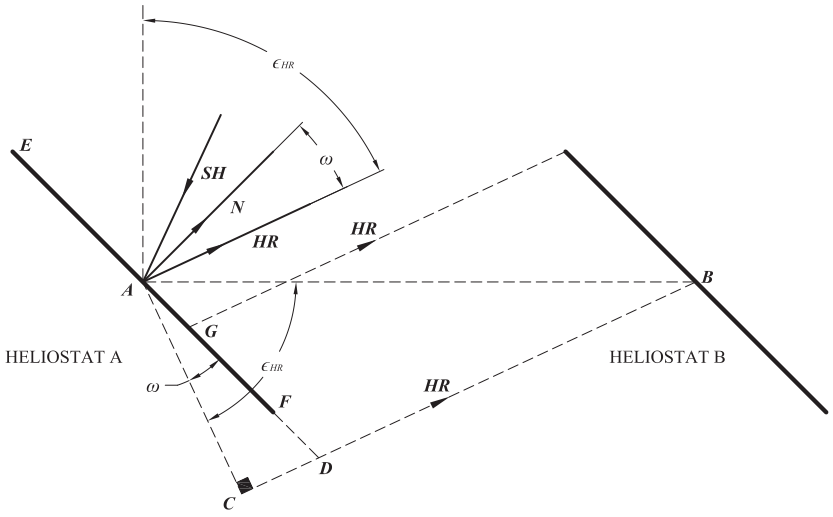

Figure 4-13: Simplified blocked projection of heliostat B on heliostat A (based on the works of Collado et al. [6]).

Several assumptions are taken. The vector $\boldsymbol{HR}$ remains constant through all the points in the heliostat surface and it is considered that the azimuthal angle between heliostats in consecutive rows is negligible. Another assumption is that there is no inclination of the ground surface. Additionally, the blocking of the heliostat is produced only by the heliostats in front of it in the previous row (closer to the tower). Finally shading was neglected since it is small compared to the blocking effect.

These assumptions allow to build the geometrical relations based on Figure 4-13. The blocked section in the main heliostat corresponds to $|\boldsymbol{GF}|$. The figure shows that

$$|\boldsymbol{GF}| = |\boldsymbol{AF}| - |\boldsymbol{AG}|. \tag{4-54}$$

It can be proven that

$$|\boldsymbol{AG}| = |\boldsymbol{AD}| - |\boldsymbol{AF}|. \tag{4-55}$$

Combining these two expressions it is possible to obtain $|\boldsymbol{GF}|$,

$$|\boldsymbol{GF}| = 2|\boldsymbol{AF}| - |\boldsymbol{AD}|. \tag{4-56}$$

$|\boldsymbol{AD}|$ can be obtained by means of a simple trigonometrical analysis,

$$|\boldsymbol{AD}| = |\boldsymbol{AB}|\frac{\cos(\epsilon_{HR})}{\cos(\omega)}. \tag{4-57}$$

Finally, combining the last two expressions the height of the blocked section, called B_{L} from now on, can be found,

$$B_{\mathrm{L}} = L_{\mathrm{HT}} - \Delta R\frac{\cos(\epsilon_{HR})}{\cos(\omega)}. \tag{4-58}$$

In this equation $2|\boldsymbol{AF}|$ has been replaced by L_{HT}, the height of the heliostat. Likewise, $|\boldsymbol{AB}|$ has been replaced by ΔR, the radius between consecutive heliostats.

The blocked surface in the heliostat problem has a rectangular shape with height B_{L}. It is necessary to obtain the width of this polygon. To do so, the blocking heliostats are projected

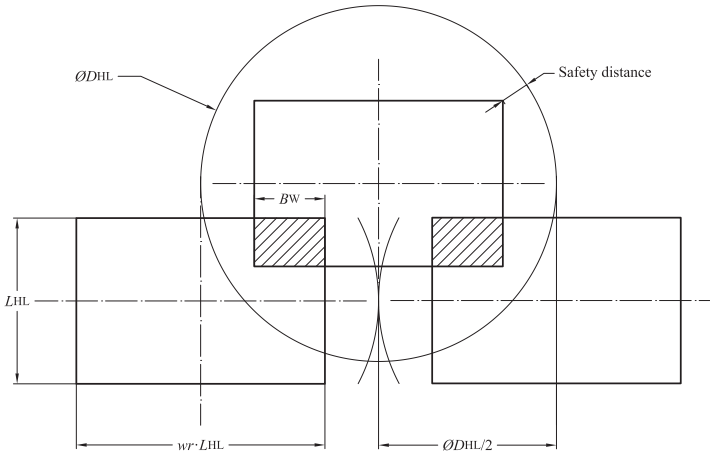

Figure 4-14: Contours of the neighboring heliostats projected onto the problem heliostat plane (based on the works of Collado et al. [6]).

on the surface of the main heliostat, as shown in Figure 4-14. This procedure is approximated and assumes that the rotation of the heliostats due to the azimuth displacement is negligible. The section of interest is B_{W}, i.e., the width of the blocked area (shadowed in the figure). This length can be found equating several sections in Figure 4-14,

$$\frac{wrL_{\mathrm{HT}}}{2} + \frac{D_{\mathrm{HT}}}{2} = \frac{wrL_{\mathrm{HT}}}{2} - B_{\mathrm{W}} + wrL_{\mathrm{HT}}. \tag{4-59}$$

Combining the last expression with equation (4-52) it is possible to obtain B_{W},

$$B_{\mathrm{W}} = wrL_{\mathrm{HT}} - \frac{\left(\sqrt{1+wr^2} + r_{\mathrm{SD}}\right) L_{\mathrm{HT}}}{2}. \tag{4-60}$$

The blocking factor is the fraction of the free area of the heliostat,

$$F_{\mathrm{SB}} = 1 - \frac{2B_{\mathrm{W}}B_{\mathrm{L}}}{wrL_{\mathrm{HT}}^2}. \tag{4-61}$$

Combining the equations (4-58), (4-60) and (4-61) the final expression for the blocking factor is obtained,

$$F_{\mathrm{SB}} = 1 - \left[1 - \frac{\Delta R}{L_{\mathrm{HT}}}\left(\frac{\cos(\epsilon_{HR})}{\cos(\omega)}\right)\right]\left[\frac{2wr - \left(\sqrt{1+wr^2} + r_{\mathrm{SD}}\right)}{wr}\right]. \tag{4-62}$$

4-2-2 Heliostat field distribution

The heliostat distribution is obtained dividing the field in concentric zones with a staggered array within each zone. This is done to avoid excessively large azimuthal distance between the heliostats. Thus, after several rows the zone distribution is restarted with a new row of consecutive heliostats. Within a zone the azimuthal spacing of the heliostats increases with increasing distance from the receiver in order to maintain the staggered array. The radial

distance is a choice dependent on the desired blocking factor (see equation (4-62)). If the aim is to have a constant blocking factor, this expression can be reordered,

$$\Delta R = \left[\frac{\cos(\omega)}{\cos(\epsilon_{HR})} \left(1 - \frac{(1 - f_{SB}) wr}{2wr - \left(\sqrt{1 + wr^2} + r_{\mathrm{SD}} \right)} \right) \right] L_{\mathrm{HT}}. \tag{4-63}$$

If ΔR is lower than the minimum value for the safety diameter, $D_{\mathrm{HT}}/2$, the radius is adjusted to match this requirement.

This procedure, proposed by Collado [11], has the advantage of a quick and simple preliminary layout of the heliostat field. However, as mentioned by this author, for deeper analysis it is necessary to obtain more accurate values for the blocking and the shading factors, the latter neglected in this work.

4-2-3 Correlations validation

In order to test the validity of the procedure, the results implemented in the engineering software [44] are compared with those of the original work. The parameters used by Collado [10] are presented in Table 4-4. He takes several information from the power plant PSA located in Almeria, Spain.

Table 4-4: Assumed values used in the validation of the heliostat field [10]

Parameter			Value
Minimum radius first zone	R_{MIN}	m	65.00
Tower optical height	THT	m	130.00
Receiver size	L_{RC}	m	9.44
Heliostat height	L_{HT}	m	10.95
Width to height ratio	wr	—	1.00
Location	—	—	PSA, Almeria
Latitude	φ	°	37.00
Standard deviation of sunshape	σ_{RC}	rad	$2.51 \cdot 10^{-3}$
Security distance ratio	r_{SD}	—	0.30
Spring equinox day	DAY	—	81.00
Solar noon hour	$HOUR$	—	12.00

The expression used to obtain ΔR, equation (4-63), is time dependent through $\cos(\omega)$. As mentioned by Collado [11], the instantaneous power collected at the solar noon in the spring equinox has difference of 1.0% to 1.5 % with the annual average. Consequently, this instant can be used as the design point for the field distribution. Recall that this case is valid for the conditions of Almeria. For different locations it is recommendable to use an annual averaged method. The results of the calculations in the present study and those of the orgininal work are shown in Figure 4-15.

Although there are slight differences between both charts, the results are virtually the same. As expected, the heliostats with the largest efficiency are located in the northern section of the field. Notice that the heliostats placed at the south of the tower are closer than those in the north, producing an asymmetric distribution. This is due to the calculation of the constant blocking factor, which affects more the northern heliostats because of their inclination that

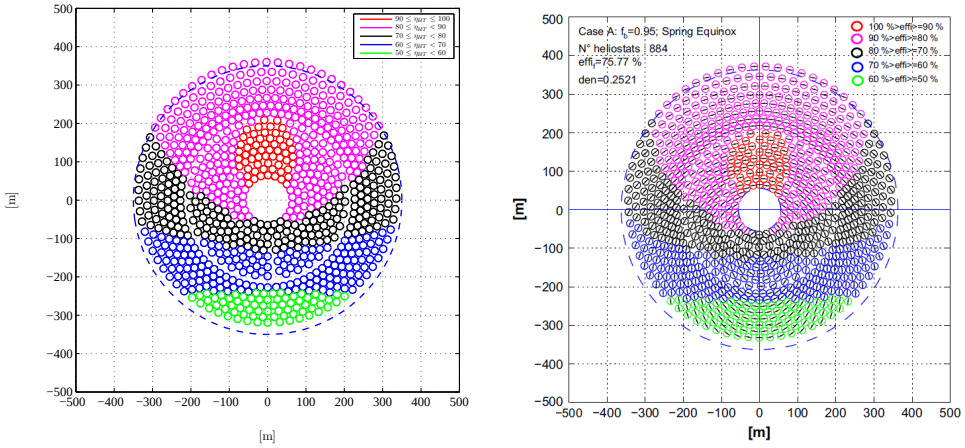

(a) Field distribution, present work.

(b) Field distribution, Collado [11].

Figure 4-15: Calculation of the heliostat distribution and field efficiency expressed in the different colors of the heliostats.

leads to a larger radial distance between them. The individual field efficiency of the heliostats can be used for further optimization options regarding the repositioning or elimination of heliostats with an efficiency lower than a threshold value.

4-2-4 Heliostat field dimensioning

In order to dimension the heliostat field, it is necessary to obtain the instant power collected by the solar tower system, which depends on the performance parameters of the heliostats and the components associated with the receiver and storage systems,

$$\dot{W}_{\mathrm{HR}} = Z A_{\mathrm{HT}} \zeta I \eta_{\mathrm{AVA}} \eta_{\mathrm{RC}} \eta_{\mathrm{STO}} \sum_{i}^{N} \eta_{\mathrm{HT(i)}}, \tag{4-64}$$

where Z is the product of the mirror reflectiveness and the cleanliness, A_{HT} is the area of the heliostat, ζ is the fraction of mirror area in the heliostat, I is the solar irradiation, η_{AVA} is the field availability, η_{RC} is the receiver efficiency, and η_{STO} is the efficiency of the storage system. The index i corresponds to a single heliostat, N to the number of heliostats in the field. The values assumed in this work are taken from the work of Collado [11] and they are listed in Table 4-5.

Table 4-5: Assumed values used in the dimensioning of the heliostat field [11]

Parameter			Value
Solar irradiation	I	$\mathrm{W/m^2}$	918.00
Mirror reflectiveness x cleanliness	Z	—	0.8883
Fraction of mirror area	ζ	—	0.9583
Field availability	η_{AVA}	—	0.99
Receiver efficiency	η_{RC}	—	0.88
Storage efficiency	η_{STO}	—	0.99

Once the required power is known from the thermodynamic analysis, the heliostat rows are successively added until this power is reached. This dimensioning procedure should be used as a starting point. In order to establish the real share of the cost between the components of the system, it is necessary to develop a detailed design of the heliostats, the receiver, the piping system, and so on.

4-2-5 Design of the s-CO_2 solar power plant

This section exemplifies the application of the integrated design methodology to the dimensioning of a solar power tower combined with a s-CO_2 power block. The thermal efficiency and the output power remain with the values used in the thermodynamic analysis and the previous study case. The performance parameters of the thermodynamic cycle are listed in Table 2-2, except for the heater efficiency because it has to be changed. The heater efficiency for solar power towers is expressed in therms of the receiver efficiency (η_{RC}) in equation (4-64), and therefore its value in the thermodynamic analysis is set to 100% in this procedure.

The power block coupled with the solar tower corresponds to the vapor recompression system since this configuration gives the lowest TIT at the lowest system pressures. The compressor discharge pressure corresponds to the minimum TIT for a system pressure loss of 2%. The operating conditions of this system and the heliostat field ditribution calculated with the computational integrateddesign tool are shown in Figure 4-16.

Parameter		Value
Power output	MW	18.70
Thermal efficiency	%	50.00
Required CO_2 mass flow	kg/s	159.86
Mass fraction α	—	0.32
Regenerator 1 effectiveness	%	92.35
Regenerator 2 effectiveness	%	96.43
Regenerator 1 power	MW	24.88
Regenerator 2 power	MW	46.51
Heater power	MW	37.41
Cooler power	MW	18.71
Compressor 1 power	MW	4.30
Compressor 2 power	MW	4.96
Turbine gross power	MW	27.96
Fan power	MW	0.15
Turbine inlet temperature	°C	646.51
Compressor discharge pressure	bar	244.95
Regenerator 1 mass	tonne	2.76
Regenerator 2 mass	tonne	13.96
Cooler bundle mass	tonne	18.34
Heliostat field area	m^2	300.00
Number of heliostats	—	636

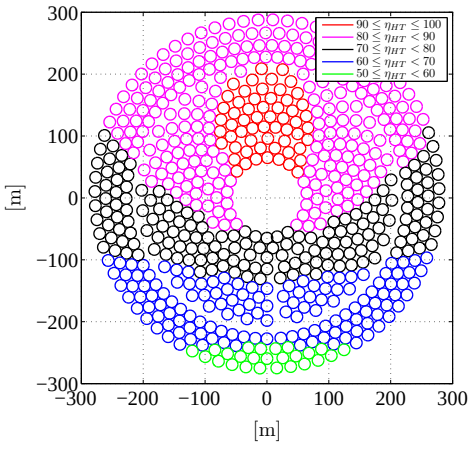

Figure 4-16: Heliostat field distribution, heliostat local efficiency, and operating conditions of the recompression Brayton power plant coupled with a solar power tower ($\eta_{TR} = 50\%$, $T_2 = 31.25°C$, $P_2 = 74$ bar, $P_3 = 244.95$ bar, $\eta_{TR} = 93.4\%$, $\eta_{CM1} = 85\%$, $\eta_{CM2} = 85\%$, $\Delta P_{LS} = 2\%$, $\Delta T_{PN} = 10°C$).

The results of the integrated design give a general impression of the dimensions of the largest components in the solar power plant for specific operating conditions. The parametrization

of the inputs in the calculation methodology can be used in economical/thermodynamical optimizations, as shown in the next section.

4-3 Optimization of the net present value of a solar tower power plant

This section deals with the formulation of an optimization problem which takes into account both the thermodynamic cycle parameters and dimensioning of the main components. The solution to this problem is left for future investigations due to its high computational costs. The optimization problem is oriented to the design of the solar tower power plant, and it is focused on the maximization of the thermal efficiency and simultaneously on the minimization of the investments associated with the system components.

The net present value is a parameter commonly used to analyze the profitability of an investment project. It is the difference between the present value of all future cash inflows produced by a property and the present value of the cash investment required to obtain the property. It can be calculated by means of the next equation

$$NPV = \sum_{\mathrm{i}=1}^{N} \frac{\Lambda_{\mathrm{i}}}{(1+k)^{\mathrm{i}}} - \Gamma_0, \tag{4-65}$$

where N is generally the number of years considered, Λ_i is the cash flows produced in a specific year i, k discount rate and Γ_0 is the initial investment. Higher net present values mean better projects and therefore its maximization is an important target in economical analysis. In this regard, equation (4-65) shows that decreasing the initial investment Γ_0 increases the NPV. Additionally, for a fixed power output, increasing the efficiency of the system decreases the collected power from the solar field, which will need a lower number of heliostats and consequently will have a lower cost. Thus, increasing the system thermal efficiency and decreasing the equipment investment can be considered the targets of these optimization problem.

Since two variables are of interest in the problem, a multi-objective optimization procedure is needed from a mathematical point of view. This problem can be stated as

$$\begin{aligned} &\text{maximize} \quad && \mathbf{F}(\mathbf{x}) = [\eta_{\mathrm{TH}}(\mathbf{x}), \varsigma(\mathbf{x})]\,, \\ &\text{subject to} \quad && j_k(\mathbf{x}) \leq 0, \quad k = 1, 2, ..., n, \end{aligned} \tag{4-66}$$

where η_{TH} is the thermal efficiency as a function of the design variables $\mathbf{x}$, and ς is a function related with the calculation of the components cost. The set of constrains is represented by j_k and n the number of functions in this set. The function ς calculates the inverse of the normalized cost of the components,

$$\varsigma(\mathbf{x}) = 1 - \frac{\varsigma'(\mathbf{x})}{|\varsigma'_{\mathrm{MAX}}|}, \tag{4-67}$$

where $\varsigma'(\mathbf{x})$ is the function that calculates the cost and $|\varsigma'_{\mathrm{MAX}}|$ is the maximum investment allowable. The cost of the components can be calculated as a function of their mass,

$$\varsigma'(\mathbf{x}) = \Psi[\Phi(\mathbf{x})], \tag{4-68}$$

where Φ is a function that calculates the mass of the regenerators and the cooler, while Ψ can be a constant or an additional function that converts this weight into the cost of the power block including the turbomachinery. A possible choice for some parameters and constraints is presented in Table 4-6. The regenerators pinch temperature is obtained from the typical

Table 4-6: Optimization parameters, inequality constraints and design variables for the optimization of the design of a s-CO_2 solar tower power plant

Parameters			
Compressor 1 efficiency	—	η_{CM1}	85.00
Compressor 2 efficiency	—	η_{CM2}	85.00
Turbine efficiency	—	η_{TR}	93.40
Compressor 1 suction T.	°C	T_2	31.25
System power	MW	$\dot{W}_{CY}$	—
Constrains set (j)			
Components cost	€	$\varsigma'(\mathbf{x})$	$\leq \lvert\varsigma'_{MAX}\rvert$
Regenerators effectiveness	%	$\varepsilon_{RG}(\mathbf{x})$	≤ 98.00
Design variables (x)			
Regenerators pinch temperature	°C	$\Delta T_{PN,RG}$	≥ 3.00
Cooler pinch temperature	°C	$\Delta T_{PN,CO}$	≥ 5.00
Pressure loss	%	ΔP_{LS}	≥ 0.00
Turbine inlet temperature	°C	T_4	≤ 600.00
Compressor discharge pressure	bar	P_3	≤ 260.00

values given by the PCHE manufacturer [3], while the one of the cooler is the standard value for air cooled heat exchangers [80]. The maximum temperature of the solar heater has been taken as 600°C, which is the typical value for towers with molten salts [31]. Finally, the maximum compressor discharge pressure is much larger than the maximum pressures in current towers (100-135 bar [76]). However, this is still a system to be further studied and additional works can prove the feasibility of such pressures for this proposal.

A multiple-objective problems generally does not have a single solution. It is rather possible to define the so called "Pareto front", which includes a set of optimal solutions that fit the definition of optimality. The Pareto optimal criteria states that a point $\mathbf{x}^*$ is Pareto optimal if and only if there does not exist another point such that $\mathrm{F}(\mathbf{x}) \geq \mathrm{F}(\mathbf{x}^*)$ and $F_i(\mathbf{x}) \geq F_i(\mathbf{x}^*)$ for at least one function [81]. In order to understand this concept consider Figure 4-17.

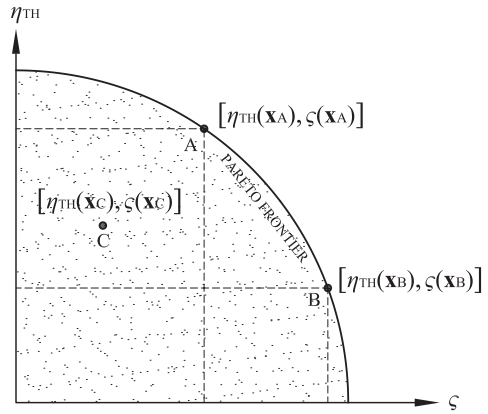

Figure 4-17: Pareto efficiency diagram.

The shadowed area represents all the possible solutions to function **F** in equation (4-66). The points that fulfill the requirement of Pareto efficiency are in the "Pareto frontier". Since this is a maximization problem, point C is not Pareto efficient since there are solutions that have both higher values in the functions η_{TH} (higher efficiency) and ς (lower cost). On the other hand, points A and B have at least one function value that is always a maximum, which makes them Pareto efficient and part of the Pareto frontier. Although the targets of this case are the efficiency and the cost of the system, it is possible to have different targets, with different constrains and parameters depending on the requirement of the optimization.

4-3-1 Solution method

Genetic algorithm techniques are attractive options to solve multi-objective optimizations since they have several advantages over other algorithms. They do not require gradient information, making them effective regardless of the shape of the objective functions and constrains. This characteristic can be useful since the optimization process of the cooler presents non linear and non continuous solutions due to the discrete geometries considered in it. Additionally, genetic algorithms are global optimization techniques, which means that they find a global set of solutions rather than a local one. This is the main reason to choose this method for multi-objective optimization since in these kind of problems there may be several solutions which comply with the Pareto optimality criteria [81].

Genetic algorithms belong to the evolutionary algorithms class since they are based on the Darwin's theory of natural selection. The reproduction cycle of this algorithm is presented in Figure 4-18.

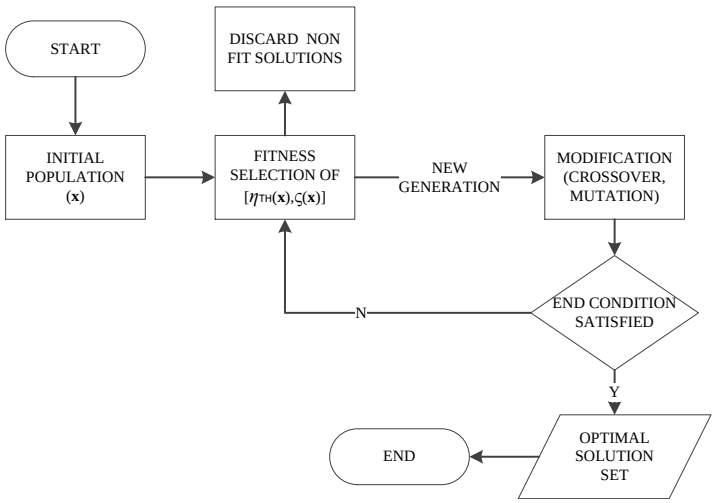

Figure 4-18: General genetic algorithm flow diagram.

The initial population represents a randomly generated set of design variables or chromosomes **x**. A design vector x_{i} could be represented by a binary code or a set of real values, which is applicable to this case. For a given population there are three operations applied: selection, crossover, and mutation. The selection is based on a criteria called fitness, which is applied on the functions η_{TH} and ς and it is proportional to the probability of surviving

into the next generation. The fitness function is defined according to the Pareto optimality criteria and returns the fitness value which is used to select the best solutions from a given population. The solutions with a low qualification are discarded and the new generation goes through the modification process, which includes the crossover and mutation. Crossover is the process of combining two different designs, generating new solutions between them. The next operation is the mutation, which is a random process that alters some parts of a genetic string.

Since there may not be a definitive answer to the issued problem it may not be obvious when to stop. Then it is recommendable to produce as many populations as possible according to the available computational resources and time. In this regard, a specific time limit or number of generations can be imposed as the criteria to continue or stop the loop. The Pareto optimality concept is not embedded into the fundamentals of the genetic algorithms, which is why an optimal solution can be generated and then die in the process. In order to avoid this the optimal solutions should be stored independently as they arise [81].

Chapter 5

Conclusions and recommendations

Conclusions

In this work, a design methodology for supercritical carbon dioxide power plants which integrates the thermodynamic analysis and the design of the individual components of the system has been developed. Supercritical CO_2 systems are a very attractive option because of their advantages like small equipment and high conversion efficiencies at moderate turbine inlet temperatures. The present study develops a innovative procedure that allows to couple and parametrize simultaneously the thermodynamic analysis and the components design.

A preliminary thermodynamic analysis is developed for three system configurations, a Brayton regenerative, a Brayton recompression and a Rankine system. The targets of the analysis are the thermal efficiency and the power output, which are set to 50% and 18.7 MW respectively. The effects of the performance and operating conditions in the components of the system are evaluated in terms of turbine inlet temperature and regeneration load. It is observed that for a constant pressure loss the turbine inlet temperature as function of the compressor discharge pressure presents a minimum. It is possible then to obtain the minimum TIT and its correspondent system pressure as a function of the pressure loss. It is shown then that the recompression system requires the lowest discharge pressures to achieve the minimum TIT.

Among the three, the Rankine configuration presents the best characteristics in terms of TIT, pressure system, regeneration load, and CO_2 mass flow. However, this system has been studied for the specific case of aerospace applications and takes advantage of a very low condensing temperature (-20°C), which makes it hardly feasible for stationary power generation, unless a mixture working fluid is adopted in order to obtained the desired critical point. The recompression system is therefore the best available option for power generation since it presents lower TITs and lower pressures than the regenerative system. However, the CO_2 mass flow and regeneration load present larger values than the regenerative system, leading to larger equipment.

The design of the components is focused on the regenerators and the cooler only. For the former, Printed Circuit Heat Exchangers are chosen as the best available options mainly due to their compactness and resistance to high pressures and temperatures. There is little information regarding the performance of this equipment given by its manufacturer. Thus, several expressions of the heat transfer coefficient and pressure drop are tested and validated against the rating values of a real PCHE. The best correlations are those given by Hesselgraves [52], and they are chosen to calculate the weight of the regenerators as function of the discharge pressure and pressure loss. The weight of the components decreases with larger discharge pressures since also the power decreases. Similarly, the larger the pressure loss, the lower the weight since larger losses lead to higher CO_2 mass flow rate, which increases the heat transfer coefficient and the pressure drop, decreasing the required travel length and the size of the PCHE.

The cooler is designed as an air cooled heat exchanger. The fan power is required to be minimal and the plain fins with staggered tube arrays match this feature. The model is based on the discretization of the tubes and the analysis of each element as a independent control volume. Two correlations are tested against a well known commercial software in order to validate them. The correlations of Ferreira [7] give the best results and they are taken for the design of this component. An optimization procedure which considers several geometries is developed and the solution characterized by the lowest fan power is chosen. The optimization shows that the lower the fan power consumption, the higher the weight. This is due to the larger number of tubes that increases the flow area reducing the air Reynolds number and pressure drop.

In the final part of the work, two study cases are analyzed with the developed tool. The first case regards the application of s-CO_2 turbines for aerospace propulsion systems. One of the best available turbofans is set as the reference engine and its thermodynamic analysis gives the performance characteristics that are to be overcome by the s-CO_2 system. Although both the recompression and the regenerative Brayton cycles meet these requirements, the weight of the regenerators is much larger than the weight of the reference engine. This leads to the conclusion that, with the design procedures for stationary power applications used in this work, the application s-CO_2 systems is not suitable for these objectives.

The second case deals with power generation by means of Solar Concentrating Power systems, since the operating temperatures needed by this technology match the requirements of the s-CO_2 with efficiencies larger than the current applications. Previous works show that the solar power tower is the technology that could be best coupled with s-CO_2. The heliostat field represents the largest cost in these systems and for this reason the model that obtains the number of heliostats and its distribution is developed. Additionally, the model gives the individual field efficiencies which allow to evaluate the related costs and implement further optimization options.

Finally, a general statement of an optimization problem applied to the second study case is presented. It takes into account both cycle performance and components dimensioning, and can be solved using the tools developed in the previous chapters. It consists in a multi-objective problem whose targets are to maximize the efficiency and minimize the cost of the system. Although the problem is not solved due to large computational time required, further improvements in the computer routines could allow to do so by means of genetic algorithms, which are suitable methods for multi-objective problems with not a single optimal solution but

rather a set of them (Pareto front). This application shows the potentiality of the developed methodology, and allows to analyze a large variety of additional optimization problems, which could have different targets and/or different constrains and parameters.

Recommendations

The present study is focused on the regenerators, the cooler and the heater design. Further developments should include the design of the turbomachinery in order to consider the effects of the components efficiency in the system. This is specially important for the compressor, which operates close to the critical point.

The design of the components is based on a steady state model. Future works should include their dynamic modeling since the heat exchangers are characterized a by large thermal inertia. This will play a fundamental role in the operation under transient conditions.

Future projects should study the modification of the critical point of CO_2 by means of gas mixtures that can adjust the critical temperature in order to bring it to levels that increase the possibility of using air as the heat sink in the condensation process of s-CO_2 Rankine power generation systems.

The design of both the cooler and the regenerator is based on a discretization procedure which evaluates each element as an individual control volume. Though it is effective, it implies long computational time and makes the parametrization slow. This is specially important for the cooler since it works close to the critical point, where the evaluation of the fluid properties is computationally more expensive. Future works should consider additional options to replace the fluid library with alternatives like look up tables or polynomial approximations directly programmed in the code.

Despite the conclusions drawn in Chapter 3, the study of the application of the s-CO_2 systems for aerospace propulsion seems promising. The main aim should be to decrease the weight of the regenerators as much as possible. This can be done varying the geometrical characteristics of the channels (channel diameter, wave length and angle, etc.) to improve the power density of the heat exchanger, using lighter materials for the manufacturing process, or analyzing additional options for compact heat exchangers. Future investigations should also consider the design of the external heater, which will bring additional complexity to the propulsion system and represents one of the largest challenges in this new propulsion concept.

Regarding the second study case, the design of the heater is constrained to the heliostat field, which has the largest cost in the power tower system. However, the cost of the overall system is not known, and deeper analysis should be performed in order to determine the actual required investments. The preliminary heliostat layout obtained should be used as a starting point, and alternative arrangements, more detailed analysis of the efficiency factors, and time averaged evaluations should be studied as well.

Appendix A

Integrated design program

The computational programs developed based on the design methodology documented in this report are found on the CD attached to this document.

Bibliography

[1] E. G. Feher, "The Supercritical Thermodynamic Power Cycle," *Energy Conversion*, vol. 8, pp. 85–90, 1968.

[2] T. Bowdery, "LNG Applications of Diffusion Bonded Heat Exchangers," in *AIChE Spring Meeting*, 2006.

[3] Heatric, a division of Meggitt Ltd., "Typical Diffusion-Bonded Heat Exchanger Characteristics," 2012.

[4] H. Song, *Investigations of a Printed Circuit Heat Exchanger for Supercritical CO_2 and Water*. PhD thesis, Inha University, 2004.

[5] Aspen Technology, Inc., "Aspen Exchanger Design & Rating V7.3.1," 2012.

[6] F. Collado and J. Turegano, "Calculation of the Annual Thermal Energy Supplied by a Defined Heliostat Field," *Solar Energy*, vol. 42, pp. 149 – 165, 1989.

[7] C. I. Ferreira, "Beproeving van Lamelconfiguraties," tech. rep., Nederlandse Maatschappij voor Energie en Milieu B.V. en Apparatenfabriek Helpman N.V., 1988.

[8] C. Wang, K. Chi, and C. Chang, "Heat Transfer and Friction Characteristics of Plain Fin-and-Tube Heat Exchangers, Part II: Correlations," *International Journal of Heat and Mass Transfer*, vol. 43, pp. 2693 – 2700, 2000.

[9] J. Mattingly, *Elements of Propulsion: Gas Turbines and Rockets*. AIAA Education Series, 2006.

[10] F. J. Collado, "Quick Evaluation of the Annual Heliostat Field Efficiency," *Solar Energy*, vol. 82, pp. 379 – 384, 2008.

[11] F. J. Collado, "Preliminary Design of Surrounding Heliostat Fields," *Renewable Energy*, vol. 34, pp. 1359 – 1363, 2009.

[12] J. Sherman, *Fossil Fuel Power*. Capstone Press, 2004.

[13] M. Tarbell and D. Schechter, *The History of the Standard Oil Company.* Cosimo, Inc., 2009.

[14] I. Dincer, "Renewable Energy and Sustainable Development: a Crucial Review," *Renewable and Sustainable Energy Reviews*, vol. 4, pp. 157 – 175, 2000.

[15] J. Harinck, *Super- and Transcritical Fluid Expansions for Next-Generation Energy Conversion Systems.* PhD thesis, Delft University of Technology, 2010.

[16] V. Dostal, M. Driscoll, and P. Hejzlar, *A Supercritical Carbon Dioxide Cycle for Next Generation Nuclear Reactors.* PhD thesis, Massachusetts Institute of Technology, 2004.

[17] G. Angelino, "Carbon Dioxide Condensation Cycles for Power Production," *Journal of Engineering for Power Transactions of the ASME*, pp. 287–295, 1968.

[18] V. Petr and M. Kolovratnik, "A Study on Application of a Closed Cycle CO_2 Gas Turbine in Power Engineering," tech. rep., Czech Technical University, 1997.

[19] V. Petr, M. Kolovratnik, and V. Hanzal, "On the Use Of CO_2 Gas Turbine in Power Engineering," tech. rep., Czech Technical University in Prague, 1999.

[20] V. Dostal, N. Todreas, P. Hejzlar, and M. Kazimi, "Power Conversion Cycle Selection for the LBE Cooled Reactor with Forced Circulation," tech. rep., Massachusetts Institute of Technology, 2001.

[21] V. Dostal, N. Todreas, P. Hejzlar, and N. Todreas, "CO_2 Brayton Cycle Design and Optimization," tech. rep., Massachusetts Institute of Technology, 2002.

[22] N. Carstens, P. Hejzlar, and M. Driscoll, "Control System Strategies and Dynamic Response for Supercritical CO_2 Power Conversion Cycles," tech. rep., Massachusetts Institute of Technology, 2006.

[23] A. Moisseytsev and S. Sienicki, "Performance Improvement Options for the Supercritical Carbon Dioxide Brayton Cycle," tech. rep., Argonne National Laboratory, 2007.

[24] S. Wright, R. Radel, M. Vernon, G. Rochau, and P. Pickard, "Operation and Analysis of a Supercritical CO_2 Brayton Cycle," tech. rep., Sandia National Laboratories, 2010.

[25] E. Parma, S. Wright, M. Vernon, D. Fleming, D. Rochau, A. Suo-Anttila, and A. R. P. Tsvetkov, "Supercritical CO_2 Direct Cycle Gas Fast Reactor (SC-GFR) Concept," tech. rep., Sandia National Laboratories, 2011.

[26] S. Wright, "Summary of the Sandia Supercritical CO_2 Development Program," tech. rep., Sandia National Laboratories, 2011.

[27] J. Cha, T. Lee, J. Eoh, S. Seong, S. Kim, D. Kim, M. Kim, T. Kim, and K. Suh, "Development of a Supercritical CO_2 Brayton Energy Conversion System Coupled with a Sodium Cooled Fast Reactor," *Nuclear Engineering and Technology*, vol. 41, pp. 1025–1044, 2009.

[28] C. Oh, T. Lillo, W. Windes, T. Totemeier, and R. Moore, "Development of a Supercritical Carbon Dioxide Brayton Cycle: Improving PBR Efficiency and Testing Material Compatibility," tech. rep., Idaho National Engineering and Environmental Laboratory, 2004.

[29] H. Yamaguchi, X. Zhang, K. Fujima, M. Enomoto, and N. Sawada, "Solar Energy Powered Rankine Cycle Using Supercritical CO_2," *Applied Thermal Engineering*, vol. 26, pp. 2345–2354, 2006.

[30] D. Chapman and D. Arias, "An Assessment of the Supercritical Carbon Dioxide Cycle for Use in a Solar Parabolic Trough Power Plant„" in *Supercritical CO_2 Power Cycle Symposium*, 2009.

[31] C. Turchi and Z. Ma, "Advanced Supercritical Carbon Dioxide Power Cycle Configurations for Use in Concentrating Solar Power System," in *Supercritical CO_2 Power Cycle Symposium*, 2011.

[32] C. Turchi, "Supercritical CO_2 for Application in Concentrating Solar Power Systems," in *Supercritical CO_2 Power Cycle Symposium*, 2009.

[33] S. Wright, T. Conboy, and G. Rochau, "Overview of Supercritical CO_2 Power Cycle Development at Sandia National Laboratories," in *2011 University Turbine Systems Research Workshop*, 2011.

[34] D. Howard, "The s-CO_2 Brayton Cycle Integrated System Test (IST)," in *Supercritical CO_2 Power Cycle Symposium*, 2009.

[35] K. Rahner and M. Hexemer, "Application of Supercritical CO_2 Brayton Cycle Integrated System Test (IST), TRACE Model to Initial Turbomachinery and Brayton Loop Testing," in *Supercritical CO_2 Power Cycle Symposium*, 2011.

[36] W. S. Jeong, J. I. Lee, and Y. H. Jeong, "Potential Improvements of Supercritical Recompression CO_2 Brayton Cycle by Mixing Other Gases for Power Conversion System of a SFR," *Nuclear Engineering and Design*, vol. 241, pp. 2128 – 2137, 2011.

[37] Y. Gong, N. Carstens, M. Driscoll, and I. Matthews, "Analysis of Radial Compressor Options for Supercritical CO_2 Power Conversion Cycles," tech. rep., MIT Department of Nuclear Science and Engineering, 2006.

[38] R. Pecknic and P. Colonna, "Accurate CFD Analysis of a Radial Compressor Operating with Supercritical CO_2," in *Supercritical CO_2 Power Cycle Symposium*, 2011.

[39] I. H. Kim and H. C. No, "Physical Model Development and Optimal Design of PCHE for Intermediate Heat Exchangers in HTGRs," *Nuclear Engineering and Design*, vol. 243, pp. 243 – 250, 2012.

[40] A. Kruizenga, M. Anderson, R. Fatima, M. Corradini, A. Towne, and D. Ranjan, "Heat Transfer of Supercritical Carbon Dioxide in Printed Circuit Heat Exchanger Geometries," *ASME Conference Proceedings*, vol. 2010, pp. 653–661, 2010.

[41] Q. Li, G. Flamant, X. Yuan, P. Neveu, and L. Luo, "Compact Heat Exchangers: A Review and Future Applications for a New Generation of High Temperature Solar Receivers," *Renewable and Sustainable Energy Reviews*, vol. 15, pp. 4855 – 4875, 2011.

[42] T. L. Ngo, Y. Kato, K. Nikitin, and T. Ishizuka, "Heat transfer and Pressure Drop Correlations of Microchannel Heat Exchangers with S-Shaped and Zigzag Fins for Carbon Dioxide Cycles," *Experimental Thermal and Fluid Science*, vol. 32, pp. 560 – 570, 2007.

[43] U.S. Department of Energy, "Concentrating Solar Power SunShot Research and Development Awards," 2012.

[44] MATLAB, *version 7.10.0 (R2010a)*. The MathWorks Inc., 2010.

[45] P. Colonna and T. van der Stelt, "FluidProp: A Program for the Estimation of Thermophysical Properties of Fluids," 2005.

[46] R. Span and W. Wagner, "A New Equation of State for Carbon Dioxide Covering the Fluid Region from the Triple-Point Temperature to 1100 K at Pressures up to 800 MPa," *Journal of Physical and Chemical Reference Data*, vol. 25, pp. 1509–1596, 1996.

[47] J. van Buijtenen and W. Visser, *Gas Turbines*. NLR, DeltaConsult, 2007.

[48] D. Seborg, T. Edgar, and D. Mellichamp, *Process Dynamics and Control*. John Wiley & Sons, Inc., 2004.

[49] R. Schleicher, A. Raffray, and C. Wong, "An Assesment of the Brayton Cycle for High Performance Power Plants," tech. rep., General Atomics, 2000.

[50] I. Dincer and M. Rosen, *Exergy: Energy, Environment and Sustainable Development*. Elsevier Science, 2007.

[51] Defense and Security Intelligence and Analysis: IHS Jane's, "Jane's Aero-Engines-Rolls-Royce Trent 1000," 2012.

[52] J. Hesselgraves, *Compact Heat Exchangers*. John Wiley & Sons, Inc., 2004.

[53] K. Nikitin, Y. Kato, and L. Ngo, "Printed Circuit Heat Exchanger Thermal and Hydraulic Performance in Supercritical CO_2 Experimental Loop," *International Jtitlournal of Refrigeration*, vol. 29, pp. 807 – 814, 2006.

[54] R. Sha and D. Sekulic, *Fundamentals of Heat Exchanger Design*. John Wiley & sons, 2003.

[55] AK Steel Corporation, "Stainless 316/316L Steel Product Data Sheet," 2007.

[56] J. van Meter, "Experimental Investigation of a PCHE Using Supercritical Carbon Dioxide and Water as Heat Transfer Media," Master's thesis, Kansas State University, 2008.

[57] Allegheny Technologies, Inc., "ATI Titanium Grade 5 Technical Data Sheet," 2012.

[58] ASM Aerospace Specification Metals, Inc., "ASM Titanium Grade 5 Technical Data Sheet," 2012.

[59] T. Ishizuka, Y. Kato, Y. Muto, K. Nikitin, N. Lam, and H. Hashimoto, "Thermal-Hydraulic Characteristics of a Printed Circuit Heat Exchanger in a Supercritical CO_2 loop," in *NURETH-11, 11th Intl. Topical Meeting on Nuclear Reactor Thermal-Hydraulics*, 2005.

[60] J. Pettersen, R. Rieberer, and S. Tollak, "Heat Transfer and Pressure Drop for Flow of Supercritical and Subcritical CO_2 in Microchannels," tech. rep., Norwegian University of Science and Technology, 2000.

[61] M. Carlson, A. Kruizenga, M. Anderson, and M. Corradini, "Measurements of Heat Transfer and Pressure Drop Characteristics of Supercritical Carbon Dioxide Flowing in

Zig-Zag Printed Circuit Heat Exchanger Channels," in *Supercritical CO_2 Power Cycle Symposium*, 2011.

[62] I. Idelchik, *Handbook of Hydraulic Resistance*. Jaico Publishing House, 2006.

[63] D. Brkic, "Review of Explicit Approximations to the Colebrook Relation for Flow Friction," *Journal of Petroleum Science and Engineering*, vol. 77, pp. 34 – 48, 2011.

[64] R. Webb and N. Kim, *Principles of Enhanced Heat Transfer*. Taylor & Francis, 2005.

[65] S. Doty and W. Turner, *Energy Management Handbook*. Fairmont Press, 2009.

[66] Bureau of Energy Efficiency, "Energy Efficient Guide Book," tech. rep., Government of India, 2004.

[67] Aalco Metals Ltd., "Stainless Steel Tubular Products," 2012.

[68] G. Cao, V. Firouzdor, K. Sridharan, M. Anderson, and T. Allen, "Corrosion of Austenitic Alloys in High Temperature Supercritical Carbon Dioxide," *Corrosion Science*, vol. 60, pp. 246 – 255, 2012.

[69] Sapa Extrusions Inc., "Extruded Aluminium Data Sheet," 2012.

[70] C. Westaway and A. Loomis, *Cameron Hydraulic Data*. Ingersoll Rand, 1984.

[71] Boeing, "Boeing 787-8 Dreamliner Fact Sheet," 2012.

[72] Lissys Ltd., "Piano: Aircraft Design and Competitor Analysis Software, Boeing 787 Sample Analysis," 2006.

[73] Rolls-Royce plc, "Gas Turbine Technology: Introduction to a jet engine," 2012.

[74] P. Spittle, "Gas turbine technology," tech. rep., Rolls-Royce plc, 2003.

[75] D. Goswami, F. Kreith, and J. Kreider, *Principles of Solar Engineering*. Taylor & Francis, 2000.

[76] M. Romero and E. Zarza, *Concentrating Solar Thermal Power*. CRC Press, 2007.

[77] Sargent & Lundy LLC Consulting Group, "Assessment of Parabolic Trough and Power Tower Solar Technology Cost and Performance Forecasts," tech. rep., National Renewable Energy Laboratory, 2003.

[78] H. Zhang, Z. Wang, M. Guo, and W. Liang, "Cosine Effciency Distribution of Heliostats Field of Solar Thermal Power Tower Plants„" tech. rep., Institute of Electrical Engineering, Chinese Academy of Sciences, 2009.

[79] B. Kistler, "A Users Manual for DELSOL3: A Computer Code for Calculating the Optical Performance and Optimal System Design for Solar Thermal Central Receiver Plants," tech. rep., Sandia National Laboratories, 1986.

[80] A. Ashwood and D. Bharathan, "Hybrid Cooling Systems for Low-Temperature Geothermal Power Production," tech. rep., National Renewable Energy Laboratory, 2011.

[81] R. Marler and J. Arora, "Survey of Multi-objective Optimization Methods for Engineering," *Struct Multidisc Optim*, vol. 26, pp. 369–395, 2004.

List of symbols

Symbols:

a	Speed of sound
A	Area
Az	Azimuthal distance
B	By pass ratio
B_W	Width of a heliostat blocked area
B_L	Length of a heliostat blocked area
C	Loss coefficient
C_{P}	Specific heat capacity at constant pressure
D	Diameter
e	Polytropic efficiency
E	Exergy
f	Mass flow
F	Thrust
F_{AT}	Attenuation factor
F_{SP}	Spillage factor
F_{SB}	Blocking factor
F_{DR}	Darcy friction factor
F_{FA}	Fanning friction factor
g	Gravitational constant
G	Mass flux
h	Specific enthalpy
k	Discount rate
K	Quality factor
L	Length
LHV	Lower value
NPV	Net present value
M	Mach number/Mass
N	Number
P	Pressure
ΔP	Pressure difference
$\dot{Q}$	Thermal load
r_{SD}	Security distance ratio
R	Radius
ΔR	Radius increment
s	Specific entropy
S	Pitch
t	Wall thickness
T	Temperature
THT	Tower optical height
ΔT_{PN}	Pinch temperature
ΔT_{C}	Cold extreme temperature difference
$\dot{V}$	Volume flow
v	Velocity
wr	Heliostat width to height ratio
U	Overall heat transfer coefficient
$\dot{W}$	Power
$\dot{W}_{\mathrm{RV}}$	Reversible power
Z	Mirror reflectiveness times cleanliness

Greek letters:

α	Mass flow fraction/heat transfer coefficient
α_{SH}	Solar ray elevation angle
χ	Heat transfer coefficient
δ	Thickness
η	Efficiency
ϵ_{HR}	Receiver-heliostat angle
γ_{SH}	Solar ray azimuth angle
Γ	Initial investment
κ	Temperature gradient
λ	Thermal conductivity
Λ	Cash flow
μ	Viscosity
ω	Incidence angle
Π	Total pressure ratio
ε	Effectiveness
φ	Latitude/relative roughness
ϑ	Solar declination
ψ	Hour angle
Ψ	Function to convert components mass into cost
Φ	Function to calculate components mass
ρ	Density
σ	Stress
σ_{RC}	Standard deviation of sunshape
ς	Function to calculate components cost
τ	Shear stress
ϑ	Solar declination
ζ	Sensitivity

Abbreviations

ISA	International standard atmosphere
RPM	Revolutions per minute
S/L	Sea level
TIT	Turbine inlet temperature
CSP	Concentrating solar power
PN	Pinch
PR	Propulsive
RC	Receiver
RG	Regenerator
TH	Thermal
TR	Turbine
TT	Thrust
TIT	Turbine inlet temperature
TOT	Total

Subscripts / superscripts:

0	Reference/environmental condition
2	Compressor/pump entering
3	Compressor/pump leaving
3.3	Low temperature regenerator leaving, cold side
3.5	High temperature regenerator leaving, cold side
4	Turbine entering
5	Turbine leaving
5.5	High temperature regenerator leaving, hot side
6	Low temperature regenerator leaving, hot side
AW	Allowed
C	Cold
CC	Combustion chamber
CE	Cold entering
CL	Cold leaving
CH	Channel
CL	Collar diameter
CM	Compressor
CO	Cooler
CR	Core
CV	Control volume
CY	Cycle
DV	Driving system
E	Entering
EX	Exergy
FA	Fan
FL	Fuel
FR	Friction
G	Generated
GR	Group of tubes
H	Hot
HD	Hydraulic
HE	Hot entering
HL	Hot leaving
HR	Heater
HT	Heliostat
I	Internal
L	Leaving
LC	Local
LS	Total loss
LM	Logarithmic mean
MIN	Minimum
MT	Motor
O	External
OBJ	Objective
OV	Overall